NASA TECHNICAL MEMORANDUM
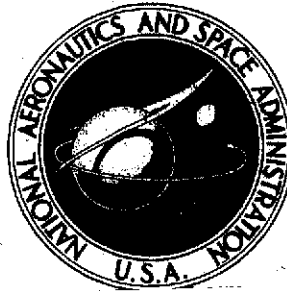
NASA TM X-3032

NASA TM X-3032

EFFECT OF GASEOUS AND SOLID SIMULATED JET PLUMES ON AN 040A SPACE SHUTTLE LAUNCH CONFIGURATION AT M = 1.6 TO 2.2

by Jules B. Dods, Jr., Jack J. Brownson,
Donald L. Kassner, Kenneth L. Blackwell,
John P. Decker, and Barney B. Roberts

Ames Research Center
Moffett Field, Calif. 94035

1. Report No. X-3032	2. Government Accession No.	3. Recipient's Catalog No.
4. Title and Subtitle EFFECT OF GASEOUS AND SOLID SIMULATED JET PLUMES ON AN 040A SPACE SHUTTLE LAUNCH CONFIGURATION AT M = 1.6 TO 2.2		5. Report Date APRIL 1974
		6. Performing Organization Code
7. Author(s) Jules B. Dods, Jr., Jack J. Brownson, Donald L. Kassner Kenneth L. Blackwell John P. Decker Barney B. Roberts		8. Performing Organization Report No. A-5212
		10. Work Unit No. 502–32–02
9. Performing Organization Name and Address NASA, Ames Research Center, Moffett Field, Calif. 94035 NASA, Marshall Space Flight Center, Huntsville, Ala. 53812 NASA, Langley Research Center, Hampton, Va. 23365 NASA, Johnson Space Center, Houston, Texas 77058		11. Contract or Grant No.
		13. Type of Report and Period Covered Technical Memorandum
12. Sponsoring Agency Name and Address National Aeronautics and Space Administration Washington, D. C., 20546		14. Sponsoring Agency Code

15. Supplementary Notes

16. Abstract

An experimental investigation was conducted to determine the effect of plume-induced flow separation and aspiration effects due to operation of both the orbiter and the solid rocket motors on a 0.019-scale model of the launch configuration of the Space Shuttle Vehicle. Longitudinal and lateral-directional stability data were obtained at Mach numbers of 1.6, 2.0, and 2.2 with and without the engines operating. The plumes exiting from the engines were simulated by a cold-gas jet supplied by an auxiliary 200-atm air supply system and by solid-body plume simulators. The aerodynamic effects produced by these two simulation procedures are compared. This report indicates that the parameters most significantly affected by the jet plumes are pitching moment, elevon control effectiveness, axial force, and orbiter wing loads. The solid rocket motor (SRM) plumes have the largest effect on the aerodynamic characteristics. The effect of the orbiter plumes in combination with the SRM plumes is, however, also significant. It is shown that variations in the nozzle design parameters and configuration changes can reduce the jet plume-induced aerodynamic effects.

17. Key Words (Suggested by Author(s)) Space Shuttle Jet plumes Plume-induced Se ·aration Stability and Control	18. Distribution Statement Unclassified — Unlimited CAT. 31	
19. Security Classif. (of this report) Unclassified	20. Security Classif. (of this page) Unclassified	21. No. of Pages · 149	22. Price* $4.75

TABLE OF CONTENTS

Page

PRECEDING PAGE BLANK NOT FILMED

NOMENCLATURE

The axis system and sign convection are shown in figure 1. Because of the limitations in the computer notation system for plotting data, conventional aerodynamic symbols are replaced by plot symbols in the data figures as follows.

Symbol	Plot symbol	
b		wing span, m
$\bar{c}$		mean aerodynamic chord, m
C_N	CN	normal-force coefficient; $\dfrac{\text{normal force}}{qS}$
C_A	CA	axial-force coefficient; $\dfrac{\text{axial force}}{qS}$
C_Y	CY	side-force coefficient; $\dfrac{\text{side force}}{qS}$
C_{A_b}	CAB	base-force coefficient; $\dfrac{\text{base force}}{qS} - \dfrac{A_b(P_b - P_\infty)}{qS}$
C_{A_f}	CAF	forebody axial-force coefficient, $C_A - C_{A_b}$
C_m	CLM	pitching-moment coefficient; $\dfrac{\text{pitching moment}}{qS\bar{c}}$
C_n	CYN	yawing-moment coefficient; $\dfrac{\text{yawing moment}}{qSb}$
C_ℓ	CBL	rolling-moment coefficient; $\dfrac{\text{rolling moment}}{qSb}$
	CWBM	wing root bending-moment coefficient; $\dfrac{\text{bending moment}}{qS\bar{c}}$
AR		aspect ratio
BL		butt line, orbiter wing reference plane, m
FS		fuselage station, m
WL		water line, m
L		length of hydrogen-oxygen tank, m
M	MACH	free-stream Mach number

q		free-stream dynamic pressure, N/m²
r		radius of nozzle, m (see footnote 1 below)
r_e		radius of nozzles at exit plane, m
r^*		radius of nozzles at throat, m
r_u		radius of upper gaseous plume boundary, m
r_ℓ		radius of lower gaseous plume boundary, m
$\bar{r}$		average gaseous plume boundary, $\dfrac{r_u + r_\ell}{2}$, m
S		wing area, m²
x		longitudinal distance from nozzle exit plane, positive downstream, m (see footnote 1 below)
	XCP/L	center of pressure
α	ALPHA	angle of attack, deg
β	BETA	angle of sideslip, deg
δ_a	AILRON	aileron deflection, deg
δ_e	ELEVON	elevon deflection, deg
δ_r	RUDDER	rudder deflection, deg
θ_N		conical nozzle angle of SRM, deg
$(\rho U)_j$		density velocity product of jet at exit plume boundary, N/m²-sec
$(\rho U)_\infty$		tunnel free-stream density velocity product, N/m²-sec
$\left(\dfrac{P_c}{P_{t_\infty}}\right)$	PC/PT	ratio of engine chamber pressure to tunnel total pressure
$\left(\dfrac{P_c}{P_t}\right)_{set}$	PC/PT	ratio as set
$\left(\dfrac{P_c}{P_e}\right)$		ratio of engine chamber pressure to nozzle exit static pressure

[1] See sketches in table 2 for additional r and x nozzle coordinate definitions.

$\left(\dfrac{P_c}{P_t}\right)_{cal}$		$\left(\dfrac{P_c}{P_t}\right)_{set}$ (calibration factor), where calibration factor $= \dfrac{(P_c/P_e)\text{theory}}{(P_c/P_e)\text{exp}}$
	NOM	nominal or design PC/PT
$\dfrac{A}{A^*}$	A/A	ratio of nozzle exit area to minimum throat area
	SRM	solid rocket motor
	ORB	orbiter
	TNK	hydrogen-oxygen tank
$\dfrac{\Delta C_\ell}{\Delta \delta_a}$	DCBL	rolling-moment coefficient increment due to control surface deflection
	DCBLP	rolling-moment coefficient increment due to control surface deflection in presence of plumes
$\dfrac{\Delta C_Y}{\Delta \delta_r}$	DCYN	yawing-moment coefficient increment due to control surface deflection
	DCYNP	yawing-moment coefficient increment due to control surface deflection in presence of plumes
$\dfrac{\Delta C_m}{\Delta \delta_e}$	DCLM	pitching-moment coefficient increment due to control surface deflection
	DCLMP	pitching-moment coefficient increment due to control surface deflection in presence of plumes
	DCBLA	ratio of rolling-moment increments due to aileron deflection, plume on divided by plume off
	DCBLR	ratio of rolling-moment increments due to rudder deflection, plume on divided by plume off
	DCYNR	ratio of yawing-moment increments due to rudder deflection, plume on divided by plume off
	DCLME	ratio of pitching-moment increments due to elevator deflection, plume on divided by plume off
C_{ℓ_β}	DCBLDB	slope of rolling-moment coefficient versus angle of sideslip
C_{n_β}	DCYNDB	slope of yawing-moment coefficient versus angle of sideslip

EFFECT OF GASEOUS AND SOLID SIMULATED JET PLUMES ON

AN 040A SPACE SHUTTLE LAUNCH CONFIGURATION AT $M = 1.6$ TO 2.2

Jules B. Dods, Jr., Jack J. Brownson, and Donald L. Kassner
Ames Research Center

Kenneth L. Blackwell
Marshall Space Flight Center

John P. Decker
Langley Research Center

and

Barney B. Roberts
Johnson Space Center

SUMMARY

An experimental investigation was conducted in the Ames 9- by 7-Foot Supersonic Wind Tunnel to determine the effect of plume-induced flow separation and aspiration effects due to operation of both the orbiter and the solid rocket motors on a 0.019-scale model of the launch configuration of the Space Shuttle Vehicle. Longitudinal and lateral-directional stability data were obtained at Mach numbers of 1.6, 2.0, and 2.2 with and without the engines operating. The plumes exiting from the engines were simulated by a cold-gas jet supplied by an auxiliary, 200-atm, air supply system and by solid-body plume simulators. The aerodynamic effects produced by these two simulation procedures are compared. The data indicate that the parameters most significantly affected by the jet plumes are pitching moment, elevon control effectiveness, axial force, and orbiter wing loads. The solid rocket motor (SRM) plumes have the largest effect on the aerodynamic characteristics. The effect of the orbiter plumes in combination with the SRM plumes is, however, also significant. Variations in the nozzle design parameters can reduce plume-induced aerodynamic effects. Configuration design changes, such as a more rearward location of the SRM nozzles, should produce smaller plume-induced effects.

The tests were conducted at angles of attack from −4° to 10° and at angles of sideslip from −4° to 6°. Flow visualization studies were made to determine the extent of flow separation on the wing and body caused by the jet plumes. The vapor-screen technique was used to show the cross-sectional shape of the operational plumes at various distances from the nozzle exit for a limited range of angles of attack.

INTRODUCTION

During the ascent, or launch, phase of the Space Shuttle Vehicle trajectory, both the orbiter main propulsion systems and the large SRM boosters are operating. The plumes formed by the

1

exhaust gases of these boosters induce flow separation over the aerodynamic control surfaces of the orbiter vehicle. This flow separation reduces the effectiveness of the vehicle aerodynamic control and increases the aerodynamic loads of the vehicle, both static and dynamic. To investigate the magnitude and significance of these plume-induced effects, tests were conducted in the Ames 9- by 7-Foot Supersonic Wind Tunnel (SWT) on a 0.019-scale model of the JSC 040A Space Shuttle Vehicle in the ascent configuration with provisions for both gaseous and solid simulation of the exhaust plumes. The tests were conducted at Mach numbers of 1.6, 2.0, and 2.2, at angles of attack from −4° to 10°, and at angles of sideslip from −4° to 6°.

Solid-plume simulation tests on the same scale model were conducted previously in the Ames 9- by 7-Foot SWT and the 11- by 11-Foot Transonic Wind Tunnel (TWT) (ref. 1). For this investigation, tests with solid plumes for $M_\infty = 1.4$ and 1.6 of the reference tests were repeated inasmuch as the pitching moments would not be comparable because, for the present tests, the pressure loads of the nozzle were not being measured by the force balance. The nozzles and their pressure chambers were an integral portion of the supporting sting. The solid plume shapes were predicted from reference 2.

Although the basic objective was to obtain the longitudinal and lateral aerodynamic stability characteristics and the vehicle control effectiveness with and without the exhaust plume simulation, wing root bending-moment increments were also obtained; off-design variations such as the number of engines operating, area ratio, and altitude were also studied.

TEST FACILITY

The Ames 9- by 7-Foot SWT is of the closed-return, variable-density type with a 9- by 7-foot rectangular test section. The nozzle is an asymmetric, sliding-block type in which the Mach number is varied by streamwise translation of the fixed contour block that forms the floor of the nozzle. The Mach number range of the SWT is continuously variable from 1.55 to 2.5. This facility can be operated at unit Reynolds numbers from 3.9370×10^6 to 21.325×10^6 per meter.

DESCRIPTION OF MODEL

The 0.019-scale model of the Space Shuttle Vehicle launch configuration consisted of a JSC 040A orbiter combined with an external hydrogen-oxygen tank (EHOT, 8.2885 m diam, full scale) and two externally mounted solid-rocket motors (SRM, 3.9624 m diam, full scale). The details of the model are shown in figures 2(a) through 2(g) and pertinent full-scale and model-scale dimensions are given in table 1. The model nozzle geometry is given in table 2. Figures 3(a) and 3(b) are front and rear views, respectively, of the model installed in the tunnel and figure 3(c) is a front view of the model with the $M = 1.4$ nozzle design solid plume simulators. Solid-plume simulators were used to compare the test results with gaseous plumes. The solid-plume simulators designed for $M = 1.4$ and 1.6 are shown in figure 2(g) and the coordinates are given in table 3. One wing of the orbiter was instrumented with strain gages to measure wing-bending moments.

PLUME SIMULATION

Both the orbiter and the SRM propulsion system exhaust plumes were simulated by air expanding from supersonic nozzles supplied by a high-pressure (200-atm) air system. The supersonic nozzles were designed on the basis of the following considerations: (1) calculated prototype plume shapes and flow characteristics, (2) application of plume simulation criteria, and (3) vehicle model limitations. The prototype plume shapes were calculated from Lockheed's Method-of-Characteristics Computer Program (VOFMOC) (ref. 3). The orbiter and SRM motor characteristics used as input to this program (summarized in table 4) represent the best data available for the engine-operating conditions and nozzle configurations.

Specific motor-nozzle specifications were not available for the SRM's. Therefore, calculation of the SRM plumes was based on the nozzle exit conditions determined only from nozzle area ratio and exit lip angle information. Equilibrium chemistry data for use with the VOFMOC program were calculated using the NASA-Lewis Chemical Equilibrium Chemistry (CEC) program (ref. 4). A propellant composition representative of prior SRM systems was used. The chamber pressure of the SRM motor decreases with time as shown in table 4. Therefore, a unique set of equilibrium chemistry data was used at each trajectory point. Newtonian pressure conditions were assumed to define the SRM plume boundaries. The free-stream flow was assumed to be uniform and parallel to the nozzle centerline. No attempt was made to consider two-phase flow effects in the flow-field calculations. SRM prototype plume boundary shapes were determined for the trajectory conditions listed in table 5.

The design of the model nozzles was an iterative process. Design criteria for the model nozzles were the plume shape similarity parameters found in reference 5. The objective of these similarity parameters is to match the overall prototype plume shape as closely as possible. However, because of a one-dimensional flow assumption used in the model nozzle design procedures, prototype values of the similarity parameters were not duplicated by the model nozzles. It was found, through parametric calculations, that the prototype plume shapes could be satisfactorily matched by the model nozzles even though the similarity parameters of reference 5 were not duplicated. In fact, this investigation revealed that all prototype plume shapes could be produced by each model nozzle whereas the criteria of reference 5 require a different nozzle for each plume shape. This allowed, at least theoretically, for the plume shapes to be held constant and for the effects of other plume parameters on base pressure and plume-induced separation to be investigated.

A consideration of the limitations dictated by the vehicle model design required that the simulation criteria be modified. For the SRM, the conical model nozzle area ratio was held constant and the angle of the conical nozzle section and the model chamber pressure were varied to satisfy plume boundary simulation. This procedure permitted the exit dimension of the nozzle to remain constant and the overall length of the nozzle to remain within acceptable limits.

The simulation of the orbiter plume shapes followed more closely the established criteria. Nozzle length limitations dictated by vehicle model considerations required the use of contoured nozzles. To satisfy this requirement, the prototype orbiter contour was scaled down. Model area ratio was changed by varying the model throat size and fairing the nozzle throat into the scaled contour. Model chamber pressure was then varied to match the prototype plume boundary shapes.

TESTING AND PROCEDURE

The model was sting mounted through the base of the external hydrogen-oxygen tank (EHOT), and force and moment data were obtained from an internally mounted, six-component, strain-gage balance. The moment center was 0.5005 m aft of the EHOT nose and 0.02316 m above the centerline (fig. 2(a)). The nozzles and the nozzle pressure chambers for both the orbiter and the SRM's were an integral portion of the sting; thus, the forces and pressures on the nozzles were not measured on the strain-gage balance. Base and cavity chord force corrections were, however, applied to the data. The jet plumes generated from the SRM's and the orbiter engines were simulated with cold air supplied by the auxiliary, 200-atm, air-supply system. The SRM's and the orbiter engines were independently supplied by a compartmented sting design. The total pressure conditions of the tunnel were dictated by the capacity of the auxiliary air-supply system to set nozzle design pressure ratios (P_c/P_{t_∞}), as well as for the under- and overexpanded pressure ratios tested to illustrate the effect of plume size. The high mass and pressure addition to the tunnel circuit caused the total pressure of the tunnel to rise considerably during a "blow" of the model engines. Special operational procedures were thus required. After sufficient experimentation with the air-pressurizing system of the tunnel, it was possible to maintain nearly constant total pressure in the tunnel during a sequence by continuous suction on the tunnel circuit.

Data were obtained at M = 1.6, 2.0, and 2.2 for angles of attack from $-4°$ to $10°$ and angles of sideslip from $-4°$ to $6°$, with and without the gaseous plume simulation. In addition, data were obtained for solid-plume simulation at a free-stream Mach number of 1.6 for M = 1.4 and 1.6 design solid-plume simulators. Fluorescent oil-flow studies of the upper and lower surfaces of the orbiter wing and body were made with and without the gaseous flow simulation.

Transition was artificially induced on the vehicle by applying spherical roughness elements to the wing, tail, and noses of the EHOT, the SRM's, and the orbiter. The roughness elements, about 2.6924×10^{-4} m in diameter, were located about 0.0254 m aft of the noses of the EHOT, the SRM's and the orbiter. The roughness strips on the wings and tail were also about 0.0254 m aft of the leading edges.

As previously mentioned, the model was tested with different design Mach number nozzles to simulate plume shapes larger and smaller than the prototype plume shape. Table 6 is a tabulation of experimentally measured plume shapes derived from schlieren photograph measurements. The nozzle test conditions are given in table 7.

RESULTS AND DISCUSSION

The objectives of the present test were to obtain longitudinal and lateral stability characteristics and rudder, aileron, and elevator control effectiveness, and wing root-bending-moment increments with and without jet exhaust plumes operating to evaluate the plume-induced separation effects on the current Space Shuttle Vehicle. Of secondary importance was the evaluation of solid versus gaseous plume simulations since the solid plumes are only a rough approximation because of the basic error in using a solid body to represent a gaseous boundary. Figures 4 and 5 present

experimentally determined, average plume shape variations with the viscous mixing parameter for various nozzle designs at free-stream Mach numbers of 1.6 and 2.0. Figure 6 shows the variation of the average gaseous plume shape with the viscous mixing parameter at a given distance from the nozzle exit, with different nozzle designs. The corresponding plume dimensions for the solid-plume simulators are also shown. The remainder of the discussion is divided into basic propulsion effects and simulation problems. The basic data are presented in figures 7 through 27 as described in detail in table 8.

Basic Propulsion Effects

Nominal power, $A/A^* = 8$ — For the space shuttle launch configuration of the present tests, the plumes generated by the propulsion system affect the aerodynamic characteristics of the vehicle significantly. The data show that pitching moment, elevon control effectiveness, axial force, and orbiter wing loads are most significantly affected. The changes in these characteristics from the power off case are, of course, caused by the plume-induced flow separation (evidenced from the force- and pitching-moment data and confirmed by fluorescent oil-flow observations, not shown). The flow separation on the wing varies significantly with angle of attack for the Mach numbers tested At near zero angle of attack, there is only a small area of separation on the wing trailing edge ahead of the plume, which extends no farther forward than the elevon hinge line. As angle of attack increases (either positively or negatively), the flow separation increases until, at $\alpha = 10°$, the outboard portion of the wing (as described by a line from 50 percent of the leading edge and 80 percent of the trailing edge) is completely separated by the jet plume. The oil flow did not cover the rear portion of the external tank and the SRM's, so the extent of flow separation there could not be visualized, but it was probably limited to a small aft region. As shown in figure 7, the plume-induced flow separation on the wing body causes a localized change in load distribution, resulting in a 10 to 20 percent decrease in normal force, creating a pitch-up moment that is maximum at $-2°< \alpha < 4°$. This pitch-up is accompanied by a large shift in C_{m_o}. Flow separation on the wing reduces the root bending-moment considerably, which follows the same trends as the total vehicle moments (fig. 7). Because the elevons are submerged in the separated-flow region, their effectiveness is drastically reduced and, for $M \geqslant 2.0$, control reversal occured (as shown in figs. 17 and 18).

Lateral-directional characteristics were not as severely affected by propulsion operation. Rudder control effectiveness was reduced by approximately 50 percent and aileron effectiveness was reduced to nearly zero, while lateral and directional stability was affected by 15 to 25 percent (fig. 8). Note that even though lateral-directional levels are reduced, the stability characteristics as a function of the angle of sideslip are more nearly linear than the longitudinal data. The longitudinal data have large shifts in the zero intercepts and the gradients change sign as a function of angle of attack.

Engine isolation— The change in the aerodynamic characteristics (as previously discussed) is caused by flow separation on the vehicle. From the data for which the orbiter and the SRM plumes are operated separately and together, the effects caused by each propulsion system can be isolated. The data indicate that the SRM plumes have the largest effect on the aerodynamic characteristics. The orbiter plumes alone have little effect on the data; however, their contribution is magnified when coupled with the SRM operation (figs. 10 and 11).

Nozzle design sensitivity— The data presented in figure 7 illustrate the rather large effects on the vehicle aerodynamic characteristics (in particular, pitching moments) for moderate changes in the prototype nozzle design. The nominal data for this test were obtained for a prototype nozzle area ratio of $A/A* = 8$, with variations on either side of this value, that is, as shown in figure 7, for $A/A* = 12$ and for an effectively lower value of $A/A*$ obtained by operating the model nozzle at about 30-percent higher than design chamber pressures. The data illustrate that larger expansion ratios (which yield smaller plumes) reduce the jet plume effect on the vehicle aerodynamics. In fact, the data are sensitive to small changes in the plume shape, in general, as illustrated by a comparison of the data in figures 4 and 5, which show the plume shape variation with various nozzle designs, with that in figures 7 and 9. Thus, variations in the nozzle design parameters can reduce plume-induced aerodynamic effects on the vehicle by increasing the nozzle area ratio, by reducing the nozzle lip angle, or by reducing the chamber pressure for the prototype propulsion system.

Simulation Effects

Validity of simulation— For these tests, the prototype was simulated by matching the plume shape using cold air as the simulant at $M = 1.6$ only. Plume sizes obtained during the present test did not necessarily simulate desired trajectory conditions. This occurred for two reasons. First, the plenum chamber pitot tubes gave erroneous readings. During a post-test check, it was discovered that two SRM pitot tubes had broken off. Also, the plenum designs could be deficient because of their small size and because sharp bends precede them. This possibility cannot be confirmed since the plenums were not calibrated thoroughly before the tests. The second error was due to oxygen liquefaction and possible water vapor condensation, as illustrated in pretest calibration data (ref. 6). The calibration data indicate that oxygen liquefied in the orbiter nozzle and outside the SRM nozzle in the plume. However, during the present test, the higher operating chamber pressure and approximately equal chamber temperatures caused the oxygen to liquefy in both the orbiter and the SRM nozzles. The oxygen liquefaction during the test indicated an oversight in the test design. However, without a heated air supply, nothing could be done to correct this design. The liquefaction tends to yield larger plumes for a given chamber pressure because heat is given off when oxygen liquefies, causing an increase in pressure. This oversized plume was confirmed when quiescent plumes from the present test were compared with analytical plumes, and has since been further confirmed in nozzle recalibrations conducted at the MSFC 14-Inch Trisonic Wind Tunnel (unpublished results). Water vapor condensation could not be confirmed by a water content measurement. Water vapor condensation was suspected because of the visibility of the plume and because, in the calibrations, plumes were not visible although oxygen liquefaction was present. However, since the present test was conducted at higher pressures, which resulted in greater oxygen liquefaction, the visibility was possibly due to a combination of liquefaction and oxygen crystals in the plume. Thus, the information presently available is insufficient to determine quantitatively the vapor state of the plume.

During this test, it was not realized that the pitot tubes were broken or that liquefaction had occurred. However, some anomaly was noted because P_c/P_e measured during the test did not match the analytical values. It was assumed that the chamber pressure measurements were erroneous and that the exit pressure measurements were accurate. On the basis of this assumption, the chamber pressures were adjusted to account for this deficiency by $(P_c/P_e)_{analytical}/(P_c/P_e)_{test}$. However, this procedure left a deficiency in plume shape when plumes were calculated on the basis of adjusted chamber pressure.

6

It appears that at least part of this discrepancy is due to the effects of liquefaction and condensation. Even though exact plume shapes could not be duplicated to match a given prototype plume shape, the major objectives of the tests were achieved by varying the plume sizes over a range large enough to provide an assessment of the effects of plume size on the aerodynamic characteristics of the vehicle (as discussed in "Nozzle design sensitivity"). For tests in which it is important to duplicate prototype plume shapes for various trajectory design altitudes and pressures, a heated air supply should be provided to eliminate oxygen liquefaction, or, if heated air is not available, the nozzles and their plenum chambers should be calibrated at the expected pressures and temperatures to compensate for pressures due to liquefaction effects.

Effect of viscous mixing parameter— Attempts to isolate the effects of the viscous mixing parameter, $(\rho U)_j/(\rho U)_\infty$ were unsuccessful because the plume size could not be held constant for varying values of $(\rho U)_j/(\rho U)_\infty$, and nozzle geometry became an unexpected variable. The reason for not being able to control the plume size (condensation effects) was previously discussed under Validity of Simulation. The data presented here show that plume-induced aerodynamic effects are, at least, a function of some parameter other than plume shape, but that the effect of $(\rho U)_j/(\rho U)_\infty$ cannot be isolated from the present results (see figs. 4, 5, and 6 and table 7). Thus, for the present investigation, plume effects were found to be a function of plume shape and nozzle geometry, neither of which was varied independently of the viscous mixing parameter. Although no conclusions can be drawn concerning the effect of $(\rho U)_j/(\rho U)_\infty$, it cannot be ruled out as a significant factor.

Comparison of solid body and gaseous plumes — The data presented in figures 6 and 12 show that, for the gaseous plumes tested, a smaller solid-body plume is required to produce similar results, particularly for longitudinal data. The $M = 1.6$ design solid-body plume (designed to simulate plumes at $M = 1.6$ and trajectory pressure altitude for an earlier test and trajectory (ref. 1)) is approximately the same size as the nominal gaseous plume at $M = 1.6$ (nominal conditions at $M = 1.6$ for the present test). Yet the pitching-moment curves show that much larger effects are caused by the solid body. This effect was not as apparent for the yaw data (figs. 8 and 12), including wing bending moments, although the effects were not too large for the gaseous plumes either. The fact that the wing bending moments were not affected differently indicates that, since the moment for the total vehicle was affected to a greater degree by the solid-body plumes, local plume interference distribution must be considerably different. Even though the wing bending-moment characteristics are nearly the same for both solid and gaseous plumes, it is suspected that the wing load distribution is altered. It would be unreasonable to expect that all interference is confined to the EHOT and SRM since the wing is so near these bodies. Note that the $M = 1.4$ solid-body simulators produced pitching-moment results very similar to those for the gaseous plumes at $M = 1.6$. However, it is believed that solid-body simulators cannot be used for more than qualitative results, and they will probably be limited to moderate angles of attack and to the higher Mach numbers where plume entrainment is small and does not affect the aft portion of the vehicle, that is, at supersonic Mach numbers and altitude where there is considerable nozzle underexpansion. If solid-body simulators are to be used even qualitatively, then a better understanding of the relationship between a solid plume and a gaseous plume is required. (A development program would be required to accomplish this.)

Effect of plumes on control effectiveness — The remainder of the data presented in figures 13 through 27 shows the effect of the plumes on elevon, aileron, and rudder power and effectiveness.

Figure 13 compares the control effectiveness for gaseous and solid SRM plumes. Plume effects with and without the orbital maneuvering system (OMS) pods are shown in figure 14, and the effect of angle of attack on the lateral characteristics with and without the OMS is shown in figures 15 and 16. Figures 17 through 20 show the effect of plumes on elevon, aileron, and rudder power. The effect of plume size on elevon and rudder power is shown in figures 21 and 22. The separate effects of orbiter and SRM plumes on elevon and rudder power is presented in figures 23 and 24. In figures 25 through 27, the effect of plumes on elevon, rudder, and aileron effectiveness is shown. The effects of the plume simulation on the control power and effectiveness presented here are given primarily to document the results obtained and are not discussed further.

CONCLUSIONS

1. For the space shuttle launch configuration of the present tests, the plumes generated by the propulsion system affect the aerodynamic characteristics of the vehicle significantly. The data show that the most significantly affected characteristics are pitching moment, elevon control effectiveness, axial force, and orbiter wing loads.

2. The SRM plumes have the largest effect on the aerodynamic characteristics. However, the orbiter plumes, when coupled with the SRM plumes, also have a significant effect.

3. For the present configuration, at the test Mach number and altitude conditions, the plume-induced separation effects are very sensitive to small changes in the SRM plume shape.

4. Variations in the nozzle design parameters can reduce plume-induced aerodynamic effects (separation, aspiration, etc.) on the vehicle. These parameters include nozzle area ratio, nozzle lip angle, and chamber pressures of the prototype propulsion system.

5. Configuration design changes, such as a more rearward location of the SRM nozzles, should also produce smaller plume-induced effects.

6. Attempts to isolate the effects of the viscous mixing parameter were unsuccessful because the plume size could not be held constant for varying values of the parameter. Plume sizes obtained during the test were not as predicted, but this result will not adversely affect the use of present results because a range of plume sizes was investigated.

7. A discussion of the factors of the present investigation that pertain to the validity of the proper simulation parameters indicates that further analysis is required.

8. A comparison of the aerodynamic results obtained from solid-body plume simulators compared to gaseous simulation indicates that solid-body simulators caused larger aerodynamic effects for the same plume size than did the gaseous plume simulation.

Ames Research Center
  National Aeronautics and Space Administration
    Moffett Field, Calif., 94035, October 11, 1973

REFERENCES

1. Brownson, Jack J.; Whitnah, A. Miles; Kassner, Donald L.; and Rampy, John: Aerodynamic Characteristics of an 040A Space Shuttle Launch Configuration with Simulated Rocket Plumes at Mach Numbers From 0.8 to 2.2. NASA TM X-62,126, 1972.

2. Penny, Morris M.; Baker, L. Ray, Jr.; and McCanna, Richard W.: Prediction of the Space Shuttle Launch Vehicle Exhaust Plumes Shapes for Several Trajectory Points. CR-115 728, 1972.

3. Smith, S. D.; and Ratliff, A. W.: Users Manual – Variable O/F Ratio Method of Characteristics Program for Nozzle and Plume Analysis. LMSC–HREC D162220 – IV, Lockheed Missiles and Space Co., Jan. 1972.

4. McBride, Bonnie; and Gordon, S.: Preliminary Description of CEC, Computer Program for Calculation of Chemical Equilibrium Compositions with Applications. Lewis Research Center, Cleveland, Ohio, May 1961.

5. Herron, R. D.: Investigation of Jet Boundary Simulation Parameters for Underexpanded Jets in a Quiescent Atmosphere. AEDC–TR–68–108, Arnold Engineering Development Center, Tullahoma, Tenn., Sept. 1968.

6. Baker, L. R.; Penny, M. M.; and McCanna, R. W.: Design and Calibration of Model Nozzles for Use in Gasdynamic Simulation of the Space Shuttle Propulsion System Exhaust Plumes. LMSC–HREC–TR D306555, Lockheed Missiles and Space Co., April 1, 1973.

TABLE 1.— MODEL GEOMETRY (JSC 040A)

Orbiter body (B1)		
	Full scale	Model scale
Length, m	33.401	0.6346
Maximum width, m	5.1816	.09845
Maximum depth, m	6.0452	.1149
Maximum cross-sectional area, m^2	28.4429	.01027
Projected base area, m^2	27.4863	.009923
Wing (W1)		
Total data		
Area		
Planform, m^2	293.1368	.1058
Span (equivalent), m	22.4028	.4257
Aspect ratio	1.71212	1.71212
Taper ratio	.14860	.14860
Dihedral angle, deg	7	7
Incidence angle, deg	1.5	1.5
Aerodynamic twist, deg	0	0
Sweep back angles		
Leading edge, deg	60	60
Trailing edge, deg	0	0
0.25 element line, deg	52.42	52.42
0.5 element line, deg	40.9	40.9
Chords		
Root (wing station 0.0), m	22.7838	.4329
Tip (equivalent), m	3.3858	.06433
MAC, m	15.4813	.2941
FS of 0.25 MAC, m	26.8714	.5106
BL of 0.25 MAC, m	4.2164	.0801
Airfoil section		
Root	NACA 0008-64	0008-64
Tip	NACA 0008-64	0008-64
Exposed data		
Area, m^2	186.7356	0.06741
Span (equivalent), m	17.2212	.3272
Aspect ratio	1.58818	1.58818
Taper ratio	.18501	.18501
Chords		
Root, m	18.3007	.3477
Tip, m	3.3858	.06435
MAC, m	12.5527	.2385
FS of 0.25 MAC, m	29.0661	.5523
BL of 0.25 MAC, m	5.9090	.1123

TABLE 1.– MODEL GEOMETRY (JSC 040A) – Continued

Elevon (W1) (each)		
	Full scale	Model scale
Area, m^2	21.1509	.007635
Span (equivalent), m	7.0612	.1342
Inboard equivalent chord, m	2.9972	.05695
Outboard equivalent chord, m	2.9972	.05695
Ratio movable surface		
Chord/total surface chord		
At inboard equivalent chord	.166	.166
At outboard equivalent chord	.516	.516
Sweep back angles		
Trailing edge, deg	0	0
Hingeline, deg	0	0

Vertical tail (V2)		
Leading-edge sweepback, deg	45	45
Airfoil section		
Root	NACA 0012-64	0012-64
Tip	NACA 0012-64	0012-64
Exposed data		
Area, m^2	45.0562	.01626
Span (equivalent), m	9.3769	.1782
Aspect ratio	1.95	1.95
Taper ratio	.3137	.3137
Chords		
Root, m	7.3152	.1390
Tip, m	2.2949	.04361
MAC, m	5.2421	.09959
FS of 0.25 MAC, m	37.3136	.7090
WP of 0.25 MAC, m	16.5720	.3149
BL of 0.25 MAC, m	0	0

Rudder (V2)		
Area, m^2	18.4585	.006663
Span (equivalent), m	8.7630	.1665
Inboard equivalent chord, m (WL = 12.700)	2.921	.0555
Outboard equivalent chord, m (WL = 21.463)	1.016	.01930
Ratio movable surface chord/total surface chord		
At inboard equivalent chord	.4	.4
At outboard equivalent chord	.4	.4

TABLE 1.— MODEL GEOMETRY (JSC 040A) — Concluded

	Full scale	Model scale
Sweep back angles		
Trailing edge, deg	25	25
Hingeline, deg	35	35
Body of revolution (EHOT)		
Length, m	48.4566	.9207
Maximum width (diam), m	8.2885	.1575
Fineness ratio	5.846	5.846
Maximum cross-sectional area, m^2	53.9558	.01948
Body of revolution (SRM) (each)		
Length, m	39.3835	.7483
Maximum width (diam), m	3.9624	.07529
Fineness ratio	9.939	9.939
Maximum cross-sectional area, m^2	12.3313	.004452

12

TABLE 2.– MODEL NOZZLE GEOMETRY

Orbiter nozzles
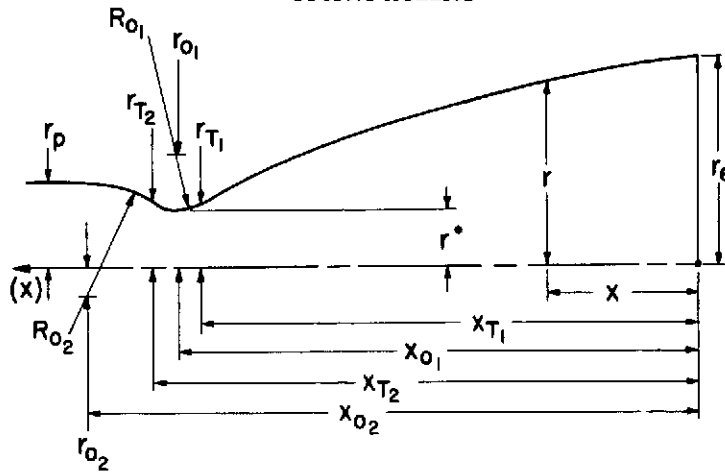
	M = 1.6 nozzle					M = 2.0 nozzle				
Coordinate	m	(in.)	Coordinate	m	(in.)	Coordinate	m	(in.)	Coordinate	m	(in.)
r_e	0.02189	(0.8619)	x_{T_2}	−0.0591	(−2.3274)	r_e	0.02189	(0.8619)	x_{T_2}	−0.0579	(−2.2814)
x_{T_1}	−.0536	(−2.1108)	r_{T_2}	.0067	(.2627)	x_{T_1}	−.0527	(−2.0740)	r_{T_2}	.0068	(.2680)
r_{T_1}	.0061	(.2383)	x_{O_2}	−.0648	(−2.5494)	r_{T_1}	.0066	(.2610)	x_{O_2}	−.0649	(−2.5558)
R_{O_1}	.0044	(.1747)	r_{O_2}	.0010	(.0408)	R_{O_1}	.0048	(.1900)	r_{O_2}	−.0031	(−.1232)
x_{O_1}	−.0560	(−2.2038)	R_{O_2}	.0080	(.3139)	x_{O_1}	−.0552	(−2.1723)	R_{O_2}	.0121	(.4779)
r_{O_1}	.0098	(.3862)	r_p	.0090	(.3547)	r_{O_1}	.0107	(.4236)	r_p	.0090	(.3547)
r^*	.0054	(.2115)				r^*	.0059	(.2336)			

Nozzle contours

x/r_e	r/r_e	x/r_e	r/r_e	x/r_e	r/r_e
−0.0340	0.9954	−1.0543	0.8098	−1.8349	0.5751
−.1043	.9856	−1.0946	.8001	−1.8987	.5504
−.1823	.9744	−1.1470	.7872	−1.9715	.5207
−.2685	.9614	−1.2143	.7700	−2.0326	.4946
−.3131	.9544	−1.2518	.7603	−2.0775	.4745
−.4134	.9380	−1.2933	.7492	−2.1435	.4438
−.5096	.9216	−1.3397	.7364	−2.2264	.4028
−.5713	.9104	−1.3908	.7219	−2.2462	.3926
−.6508	.8957	−1.4564	.7026	−2.3097	.3586
−.6951	.8871	−1.5187	.6837	−2.3427	.3401
−.7444	.8774	−1.5595	.6708	−2.3598	.3302
−.7993	.8662	−1.6111	.6543	−2.4063	.3028[a]
−.8601	.8535	−1.6724	.6337	−2.4287	.2891
−.9275	.8388	−1.7483	.6071	−2.4490	.2765[b]
−.9919	.8243	−1.7934	.5907		

[a]End of M = 2.0 nozzle.

[b]End of M = 1.6 nozzle.

TABLE 2.– MODEL NOZZLE GEOMETRY – Concluded

SRM nozzles
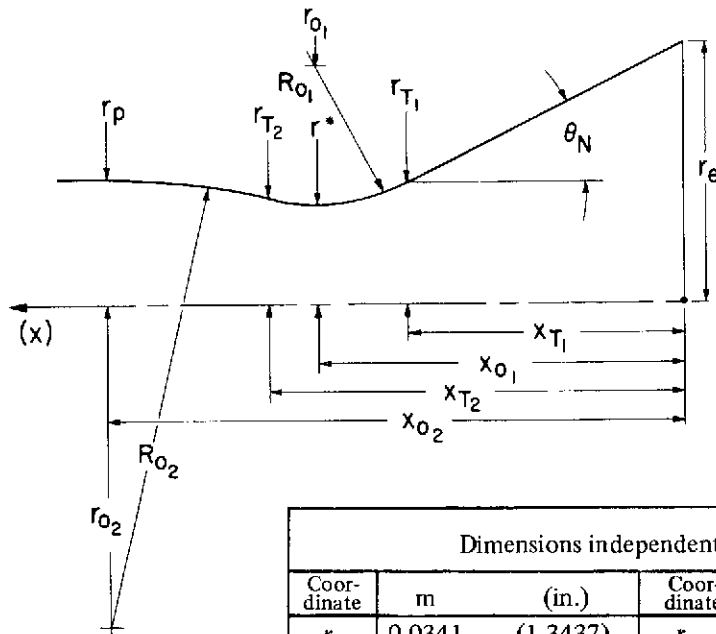
Dimensions independent of design M					
Coordinate	m	(in.)	Coordinate	m	(in.)
r_e	0.0341	(1.3437)	r_{T_2}	0.0137	(0.5412)
r_{O_1}	.0386	(1.5200)	R_{O_2}	.0876	(3.4476)
R_{O_1}	.0257	(1.0133)	r_{O_2}	−.0708	(−2.7889)
r^*	.0129	(.5067)	r_P	.0167	(.6587)

Dimensions that vary with design M							
$M = 0.9$ nozzle		$M = 1.6$ nozzle		$M = 2.0$ nozzle		$M = 3.0$ nozzle	
Coordinate	m	(in.)	m	(in.)	m	(in.)	m	(in.)
x_{T_1}	−0.0500	(−1.9693)	−0.03997	(−1.5738)	−0.0368	(−1.4494)	−0.0314	(−1.2373)
r_{T_1}	.0146	(.5759)	.0153	(.6031)	.0156	(.6147)	.0162	(.6394)
x_{O_1}	−.0594	(−2.3373)	−.0509	(−2.0052)	−.0484	(−1.9047)	−.0442	(−1.7386)
x_{T_2}	−.0660	(−2.5996)	−.0576	(−2.2675)	−.0550	(−2.1669)	−.0508	(−2.0009)
x_{O_2}	−.0887	(−3.4919)	−.0803	(−3.1598)	−.0777	(−3.0592)	−.0735	(−2.8932)
	deg		deg		deg		deg	
θ_N	21.3000		25.2000		26.7000		29.6500	

TABLE 3.– SRM SOLID PLUME SHAPES (from ref. 2)

Nozzle: $M = 1.4$ $P_c = 526.75 \times 10^4$ N/m^2 $P_\infty = 147.95 \times 10^2$ N/m^2		Nozzle: $M = 1.6$ $P_c = 513.66 \times 10^4$ N/m^2 $P_\infty = 96.239 \times 10^2$ N/m^2	
x/r_e	$\bar{r}/r_e$	x/r_e	$\bar{r}/r_e$
0	1.00	0	1.00
.164	1.149	.522	1.507
.537	1.448	1.239	2.052
1.052	1.784	2.119	2.575
1.776	2.172	2.784	2.896
2.545	2.500	3.552	3.216
3.269	2.746	4.418	3.507
4.545	3.067	5.388	3.761
6.000	3.291	7.567	4.127
6.791	3.351	8.955	4.231
7.612	3.381		
8.955	3.381		

TABLE 4.— PROTOTYPE NOZZLE–MOTOR CHARACTERISTICS

SRM	Orbiter
P_c (see figure below) $A/A^* = 8.0$ $\theta_{lip} = 17.5°$ $D_{ex} = 3.5921$ m $D_T = 1.27$ m	Area ratio $\quad \epsilon = 79.436{:}1$ $P_c = 200$ atm $\quad \theta_{lip} = 7.87°$ $D_t = 0.2585$ m $\quad D_{ex} = 2.3043$ m
Propellant composition $\quad AP \quad\quad 69.0$ $\quad A\ell \quad\quad 15.0 \quad$ } by weight $\quad PBAN \quad 9.6$ $\quad$ Binder materials $\quad 6.4\%$	Propellant composition $\quad O/F = 6.0$ Oxidizer $-O_2$ (L) $\quad\quad\quad\quad\quad\quad$ Fuel $\quad -H_2$ (L)
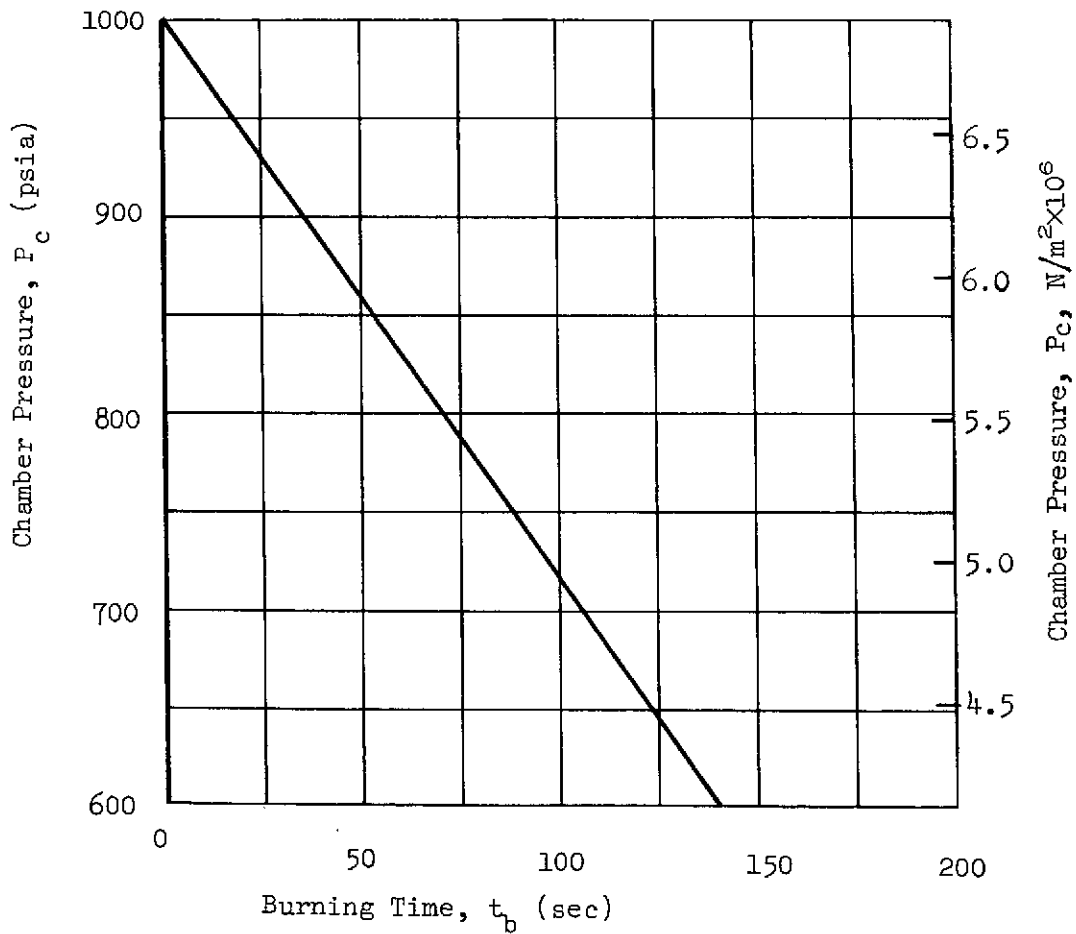
TABLE 5.— LAUNCH TRAJECTORY CONDITIONS

M_∞	$t,$ sec	Altitude $h,$ m	P_∞ N/m²
0.9	58	7,620	38,687
1.2	73	11,278	23,461
1.6	89	16,459	9,624
2.0	101	21,031	4,788
2.2	107	24,079	2,777
3.0	117	30,785	1,053

TABLE 6.— EXPERIMENTAL SRM PLUME SHAPES AND TEST CONDITIONS

Nozzle: $M = 1.6$, at $M = 1.6$
Run 2, correlation 570
SRM and orbiter engine operating
SRM data:

$(P_c/P_t)_{set} = 132$; $(P_c/P_t)_{cal} = 154$

$(\rho U)_j = 5.0179 \times 10^3$; $(\rho U)_\infty = 4.1512 \times 10^2$

$(\rho U)_j /(\rho U)_\infty = 12.1$

Nozzle: $M = 1.6$, at $M = 1.6$
Run 9, correlation 739
SRM and orbiter engine operating
SRM data:

$(P_c/P_t)_{set} = 77.6$; $(P_c/P_t)_{cal} = 90.7$

$(\rho U)_j = 1.075 \times 10^4$; $(\rho U)_\infty = 1.1108 \times 10^3$

$(\rho U)_j/(\rho U)_\infty = 9.69$

x/r_e	r_u/r_e	r_ϱ/r_e	$\bar{r}/r_e$	x/r_e	r_u/r_e	r_ϱ/r_e	$\bar{r}/r_e$
0.37	1.31	NA	NA	0.37	1.28	NA	NA
.74	1.58	NA	NA	.74	1.49	NA	NA
1.12	1.85	NA	NA	1.12	1.70	NA	NA
1.49	2.08	NA	NA	1.49	1.87	NA	NA
1.86	2.26	NA	NA	1.86	2.02	NA	NA
2.23	2.50	NA	NA	2.23	2.14	NA	NA
2.61	2.62	2.77	2.70	2.61	2.23	NA	NA
2.98	2.80	3.01	2.91	2.98	2.35	NA	NA
3.35	2.92	3.12	3.02	3.35	2.41	2.89	2.65
3.72	3.07	3.30	3.19	3.72	2.47	3.01	2.74
4.47	3.27	3.54	3.41	4.47	2.62	3.18	2.90
5.21	3.45	3.75	3.60	5.21	2.68	3.36	3.02
5.96	3.63	3.93	3.78	5.96	2.74	3.51	3.13
6.67	3.75	4.11	3.93	6.67	2.80	3.66	3.23
7.44	3.87	4.26	4.07	7.44	2.89	3.81	3.35
8.93	3.96	4.55	4.26	8.93	2.89	3.98	3.44
10.42	3.87	NA	NA	10.42	2.83	4.08	3.46

TABLE 6.– EXPERIMENTAL SRM PLUME SHAPES AND TEST CONDITIONS – Continued

Nozzle: $M = 3.0$, at $M = 1.6$
Run 79, correlation 1676
SRM engine operating
SRM data:

$(P_c/P_t)_{set} = 225$; $(P_c/P_t)_{cal} = 262$

$(\rho U)_j = 1.2229 \times 10^4$; $(\rho U)_\infty = 7.6273 \times 10^2$

$(\rho U)_j/(\rho U)_\infty = 16.03$

x/r_e	r_u/r_e	r_ϱ/r_e	$\bar{r}/r_e$
0.37	1.40	NA	NA
.74	1.76	NA	NA
1.12	2.08	NA	NA
1.49	2.35	NA	NA
1.86	2.65	2.80	2.72
2.23	2.95	3.07	3.01
2.61	3.18	3.30	3.24
2.98	3.39	3.54	3.47
3.35	3.57	3.75	3.66
3.72	NA	NA	NA
4.47	4.11	NA	NA
5.21	4.40	NA	NA
5.96	4.70	NA	NA
6.67	4.91	NA	NA
7.44	5.15	NA	NA
8.93	5.45	NA	NA
10.42	5.62	NA	NA

TABLE 6.– EXPERIMENTAL SRM PLUME SHAPES AND TEST CONDITIONS – Continued

Nozzle: $M = 1.6$, at $M = 1.6$ Run 14, correlation 812 SRM and orbiter engine operating SRM data:				Nozzle: $M = 1.6$, at $M = 1.6$ Run 13, correlation 798 SRM engine operating SRM data:			
$(P_c/P_t)_{set} = 177; (P_c/P_t)_{cal} = 206$				$(P_c/P_t)_{set} = 137; (P_c/P_t)_{cal} = 160$			
$(\rho U)_j = 1.1937 \times 10^4; (\rho U)_\infty = 8.5754 \times 10^2$				$(\rho U)_j = 1.4220 \times 10^4; (\rho U)_\infty = 1.1348 \times 10^3$			
$(\rho U)_j/(\rho U)_\infty = 13.92$				$(\rho U)_j/(\rho U)_\infty = 12.53$			
x/r_e	r_u/r_e	r_ϱ/r_e	$\bar{r}/r_e$	x/r_e	r_u/r_e	r_ϱ/r_e	$\bar{r}/r_e$
0.37	1.28	NA	NA	0.37	1.34	NA	NA
.74	1.61	NA	NA	.74	1.58	NA	NA
1.12	1.85	NA	NA	1.12	1.85	NA	NA
1.49	2.14	NA	NA	1.49	2.05	NA	NA
1.86	2.32	NA	NA	1.86	2.23	NA	NA
2.23	2.50	2.92	2.71	2.23	2.41	2.83	2.62
2.61	2.65	3.18	2.92	2.61	2.59	3.01	2.80
2.98	2.83	3.36	3.10	2.98	2.77	3.18	2.98
3.35	2.95	3.54	3.25	3.35	2.92	3.30	3.11
3.72	3.07	3.72	3.40	3.72	3.07	3.48	3.28
4.47	3.24	3.99	3.62	4.47	3.27	3.75	3.51
5.21	3.42	4.26	3.84	5.21	3.48	3.99	3.74
5.96	3.60	NA	NA	5.96	3.66	4.20	3.93
6.67	3.72	NA	NA	6.67	3.81	4.40	4.11
7.44	3.84	NA	NA	7.44	3.93	4.58	4.26
8.93	4.08	NA	NA	8.93	4.17	4.88	4.53
10.42	4.26	NA	NA	10.42	4.26	NA	NA

19

TABLE 6.— EXPERIMENTAL SRM PLUME SHAPES AND TEST CONDITIONS — Continued

Nozzle: $M = 0.9$, at $M = 1.6$
Run 75, correlation 1642
SRM engine operating
SRM data:

$(P_c/P_t)_{set} = 141$; $(P_c/P_t)_{cal} = 165$

$(\rho U)_j = 1.5274 \times 10^4$; $(\rho U)_\infty = 1.2545 \times 10^3$

$(\rho U)_j/(\rho U)_\infty = 12.2$

Nozzle: $M = 0.9$, at $M = 1.6$
Run 69, correlation 1587
SRM engine operating
SRM data:

$(P_c/P_t)_{set} = 96.4$; $(P_c/P_t)_{cal} = 113$

$(\rho U)_j = 1.5752 \times 10^4$; $(\rho U)_\infty = 1.5465 \times 10^3$

$(\rho U)_j/(\rho U)_\infty = 10.2$

x/r_e	r_u/r_e	r_ℓ/r_e	$\bar{r}/r_e$	x/r_e	r_u/r_e	r_ℓ/r_e	$\bar{r}/r_e$
0.74	1.36	NA	NA	0.74	1.31	NA	NA
1.49	1.84	NA	NA	1.49	1.73	NA	NA
2.23	2.20	NA	NA	2.23	2.02	NA	NA
2.98	2.56	NA	NA	2.98	2.32	NA	NA
3.35	2.68	2.68	2.68	3.35	2.44	2.32	2.38
3.72	2.80	2.74	2.77	3.72	2.56	2.50	2.53
4.47	3.03	3.15	3.09	4.47	2.68	2.92	2.80
5.21	3.33	3.33	3.33	5.21	2.92	3.03	2.97
5.76	3.45	3.63	3.54	5.96	2.98	3.15	3.07
6.67	3.57	3.81	3.69	6.67	3.03	3.39	3.21
7.44	3.75	3.99	3.87	7.44	3.09	3.51	3.30
8.93	3.93	4.11	4.02	8.93	NA	NA	NA
10.42	3.99	4.34	4.17	10.42	NA	NA	NA

TABLE 6.– EXPERIMENTAL SRM PLUME SHAPES AND TEST CONDITIONS – Continued

Nozzle: $M = 3.0$, at $M = 1.6$
Run 80, correlation 1686
SRM engine operating
SRM data:

$(P_c/P_t)_{set} = 156$; $(P_c/P_t)_{cal} = 182$

$(\rho U)_j = 1.0222 \times 10^4$; $(\rho U)_\infty = 7.4789 \times 10^2$

$(\rho U)_j/(\rho U)_\infty = 13.67$

Nozzle: $M = 3.0$, at $M = 1.6$
Run 78, correlation 1666
SRM engine operating
SRM data:

$(P_c/P_t)_{set} = 189$; $(P_c/P_t)_{cal} = 221$

$(\rho U)_j = 1.1625 \times 10^4$; $(\rho U)_\infty = 7.8093 \times 10^2$

$(\rho U)_j/(\rho U)_\infty = 14.89$

x/r_e	r_u/r_e	r_ℓ/r_e	$\bar{r}/r_e$	x/r_e	r_u/r_e	r_ℓ/r_e	$\bar{r}/r_e$
0.37	1.25	NA	NA	0.37	1.34	NA	NA
.74	1.64	NA	NA	.74	1.64	NA	NA
1.12	1.93	NA	NA	1.12	1.87	NA	NA
1.49	2.20	NA	NA	1.49	2.20	NA	NA
1.86	2.49	NA	NA	1.86	2.47	2.77	2.62
2.23	2.65	2.89	2.77	2.23	2.71	2.95	2.83
2.61	2.89	3.12	3.01	2.61	2.95	3.18	3.07
2.98	3.07	3.27	3.17	2.98	3.15	3.36	3.26
3.35	3.24	3.45	3.35	3.35	3.30	3.54	3.42
3.72	3.42	3.66	3.54	3.72	3.45	3.75	3.60
4.47	3.72	3.96	3.84	4.47	3.78	4.14	3.96
5.21	3.90	4.23	4.07	5.21	4.08	NA	NA
5.96	4.11	4.32	4.22	5.96	4.29	NA	NA
6.67	4.29	4.52	4.41	6.67	4.46	NA	NA
7.44	4.40	4.67	4.54	7.44	4.67	NA	NA
8.93	4.61	4.97	4.79	8.93	4.97	NA	NA
10.42	4.72	5.21	4.97	10.42	5.24	NA	NA

TABLE 6.– EXPERIMENTAL SRM PLUME SHAPES AND TEST CONDITIONS – Continued

Nozzle: $M = 2.0$, at $M = 2.0$
Run 32, correlation 1090
SRM and orbiter engine operating
SRM data:

$(P_c/P_t)_{set} = 141; (P_c/P_t)_{cal} = 165$

$(\rho U)_j = 1.1396 \times 10^4; (\rho U)_\infty = 7.8524 \times 10^2$

$(\rho U)_j/(\rho U)_\infty = 14.5$

Nozzle: $M = 2.0$, at $M = 2.0$
Run 37, correlation 1156
SRM and orbiter engine operating
SRM data:

$(P_c/P_t)_{set} = 71; (P_c/P_t)_{cal} = 83$

$(\rho U)_j = 8.1396 \times 10^3; (\rho U)_\infty = 7.7566 \times 10^2$

$(\rho U)_j/(\rho U)_\infty = 10.5$

x/r_e	r_u/r_e	r_ϱ/r_e	$\bar{r}/r_e$	x/r_e	r_u/r_e	r_ϱ/r_e	$\bar{r}/r_e$
0.37	1.28	NA	NA	0.37	1.19	NA	NA
.74	1.58	NA	NA	.74	1.43	NA	NA
1.12	1.90	NA	NA	1.12	1.64	NA	NA
1.49	2.20	NA	NA	1.49	1.85	NA	NA
1.86	2.44	2.86	2.65	1.86	1.99	NA	NA
2.23	2.65	3.10	2.88	2.23	2.14	NA	NA
2.61	2.83	3.30	3.06	2.61	2.29	2.98	2.64
2.98	2.98	3.48	3.23	2.98	2.47	3.07	2.76
3.35	3.12	3.69	3.40	3.35	2.53	3.24	2.89
3.72	3.27	3.90	3.59	3.72	2.62	3.39	3.00
4.47	3.51	4.20	3.86	4.47	2.80	3.66	3.23
5.21	3.69	4.55	4.12	5.21	2.98	3.87	3.43
5.96	3.87	4.76	4.31	5.96	3.07	4.11	3.59
6.67	3.99	NA	NA	6.67	3.18	4.26	3.72
7.44	4.11	NA	NA	7.44	3.27	4.37	3.82
8.93	4.37	NA	NA	8.93	3.45	4.61	4.03
10.42	4.52	NA	NA	10.42	3.60	NA	NA

TABLE 6.– EXPERIMENTAL SRM PLUME SHAPES AND TEST CONDITIONS – Concluded

Nozzle: $M = 2.0$, at $M = 2.0$
Run 38, correlation 1166
SRM and orbiter engine operating
SRM data:

$(P_c/P_t)_{set} = 181$; $(P_c/P_t)_{cal} = 211$

$(\rho U)_j = 9.8154 \times 10^3$; $(\rho U)_\infty = 5.9372 \times 10^2$

$(\rho U)_j/(\rho U)_\infty = 16.5$

Nozzle: $M = 2.0$, at $M = 2.0$
Run 43, correlation 1210
SRM engine operating
SRM data:

$(P_c/P_t)_{set} = 127$; $(P_c/P_t)_{cal} = 149$

$(\rho U)_j = 1.1683 \times 10^4$; $(\rho U)_\infty = 8.4269 \times 10^2$

$(\rho U)_j/(\rho U)_\infty = 13.9$

x/r_e	r_u/r_e	r_ϱ/r_e	$\bar{r}/r_e$	x/r_e	r_u/r_e	r_ϱ/r_e	$\bar{r}/r_e$
0.37	1.34	NA	NA	0.37	1.31	NA	NA
.74	1.64	NA	NA	.74	1.61	NA	NA
1.12	1.93	NA	NA	1.12	1.87	NA	NA
1.49	2.20	2.62	2.41	1.49	2.11	NA	NA
1.86	2.50	2.83	2.67	1.86	2.35	NA	NA
2.23	2.74	3.10	2.92	2.23	2.53	3.04	2.78
2.61	2.98	3.33	3.16	2.61	2.74	3.27	3.00
2.98	3.12	3.51	3.31	2.98	2.92	3.48	3.20
3.35	3.27	3.72	3.50	3.35	3.07	3.66	3.37
3.72	3.42	3.90	3.66	3.72	3.27	3.84	3.55
4.47	3.69	4.26	3.98	4.47	3.54	4.14	3.84
5.21	3.90	4.55	4.23	5.21	3.87	4.47	4.17
5.96	4.05	4.82	4.44	5.96	4.11	4.73	4.42
6.67	4.20	5.09	4.65	6.67	4.37	4.94	4.66
7.44	4.32	5.36	4.84	7.44	4.55	5.15	4.85
8.93	4.55	NA	NA	8.93	4.82	NA	NA
10.42	4.67	NA	NA	10.42	4.94	NA	NA

TABLE 7.-- NOZZLE TEST CONDITIONS

Run	Correlation	M_∞	M_{nozzle}	$(\rho U)_j/(\rho U)_\infty$	$P_{c_{set}}$	Orbiter[a]			Design	SRM[b]		Design
						P_{c_1}/P_{t_∞}	P_{c_2}/P_{t_∞}	P_{c_3}/P_{t_∞}	P_c/P_{t_∞}	P_{c_4}/P_{t_∞}	P_{c_5}/P_{t_∞}	P_c/P_{t_∞}
2	510	1.6	1.6	12.1	Nom.	151.4	147.7	148.1	118.0	147.6	154.2	155.9
3	598			12.41	Nom.	110.4	107.8	108.8	118.0	150.6	156.6	155.9
9	739			9.67	$A/A^* = 12$	120.5	117.8	118.0	118.0	86.9	90.67	91.03
12	781			—	Nom. ORB only	113.5	111.0	111.1	118.0	—	—	—
13	798			12.53	Nom. SRM only	—	—	—	—	153.8	159.8	155.9
14	812			13.92	$1.3P_c$ Nom.	149.4	146.0	146.3	153.4	198.1	206.4	202.7
32	1090	2.0	2.0	14.50	Nom.	98.37	95.33	97.16	101.2	158.0	164.8	165.6
37	1156			10.53	$A/A^* = 12$	103.6	100.9	102.9	101.2	80.19	83.28	84.66
38	1166			16.09	$1.3P_c$	131.8	123.2	130.7	131.6	203.3	211.1	215.3
42	1200			NA	Nom. ORB only	96.46	93.80	95.31	101.2	—	—	—
43	1210			13.83	Nom. SRM only	—	—	—	—	143.0	143.8	165.6
44	1225	2.2		16.31	Nom.	170.1	165.6	167.2	169.5	176.6	188.4	185.8
45	1242	2.0		14.43	Nom. SRM only	—	—	—	—	158.4	165.5	165.6
47	1269	2.2		16.51	Nom.	162.2	158.1	160.4	169.5	182.7	190.2	185.8
78	1666	1.6	3.0	14.89	Nom. SRM only	—	—	—	—	213.6	221.1	228.2
79	1676			16.03	$1.2P_c$, SRM only	—	—	—	—	253.8	262.4	273.8
80	1686			13.67	$.8P_c$, SRM only	—	—	—	—	175.5	182.0	182.5
75	1642		0.9	12.20	$1.1P_c$, SRM only	—	—	—	—	160.3	165.1	162.8
69	1587			10.17	SRM only	—	—	—	—	109.1	112.8	—
72	1612			10.76	SRM only	—	—	—	—	170.1	124.1	—

[a]$P_{c_{1,2,3}} = P_{c_{1,2,3}}$ tunnel output/0.931.

[b]$P_{c_{4,5}} = P_{c_{4,5}}$ tunnel output/0.855.

TABLE 8.– INDEX OF DATA FIGURES

Figure	Title
1	Axes system showing direction and sense of force and moment coefficients, angle of attack, and sideslip angles
2	Model description
3	Installation of the 0.019-scale model launch configuration of the Space Shuttle Vehicle with the 040A orbiter
4	Average plume shape variations with the viscous mixing parameter $(\rho U)_j/(\rho U)_\infty$ for various SRM nozzle designs at $M = 1.6$
5	Average SRM plume shape variations with the viscous mixing parameter $(\rho U)_j/(\rho U)_\infty$ for $M = 2.0$ nozzle design at $M = 2.0$
6	Variation of the average gaseous SRM plume shape with the viscous mixing parameter at a given distance from the nozzle exit
7	Effect of plume size on the longitudinal characteristics at $\beta = 0°$
8	Effect of plume size on lateral characteristics at $\alpha = 0°$
9	Effect of nozzle design point on longitudinal characteristics at $\beta = 0°$ and $M = 1.60$
10	Effect of the orbiter and the solid rocket motor (SRM) plumes on longitudinal characteristics at $\beta = 0°$
11	Effect of the orbiter and the solid rocket motor (SRM) plumes on lateral characteristics at $\alpha = 0°$
12	Comparison of gaseous and solid simulated SRM jet plumes at $M = 1.60$
13	Comparison of the control effectiveness with gaseous and solid simulated SRM jet plumes at $M = 1.60$
14	Plume effects with and without the orbital maneuvering system (OMS) at $M = 1.60$
15	Effect of angle of attack and plumes on the lateral characteristics at $M = 1.60$ with OMS
16	Effect of angle of attack and plumes on the lateral characteristics at $M = 1.98$ without the OMS
17	Effect of plumes on the elevon and rudder power at $\beta = 0°$
18	Effect of plumes on the elevon and rudder power at $\alpha = 0°$
19	Effect of plumes on the aileron power at $\beta = 0°$ and $M = 1.98$
20	Effect of plumes on the aileron power at $\alpha = 0°$

TABLE 8.– INDEX OF DATA FIGURES — Concluded

Figure	Title
21	Effect of the size of the plumes on the elevon and rudder power at $\beta = 0°$
22	Effect of the size of the plumes on the elevon and rudder power at $\alpha = 0°$
23	Effect of the orbiter and the solid rocket motor (SRM) plumes on the elevon and rudder power at $\beta = 0°$
24	Effect of the orbiter and the solid rocket motor (SRM) plumes on the elevon and rudder power at $\alpha = 0°$
25	Effect of the orbiter and the solid rocket motor (SRM) plumes on the elevon effectiveness parameters at $\beta = 0°$
26	Effect of the orbiter and the solid rocket motor (SRM) plumes on the rudder effectiveness parameters at $\beta = 0°$
27	Effect of the orbiter and the solid rocket motor (SRM) plumes on the aileron effectiveness parameters at $\alpha = 0°$
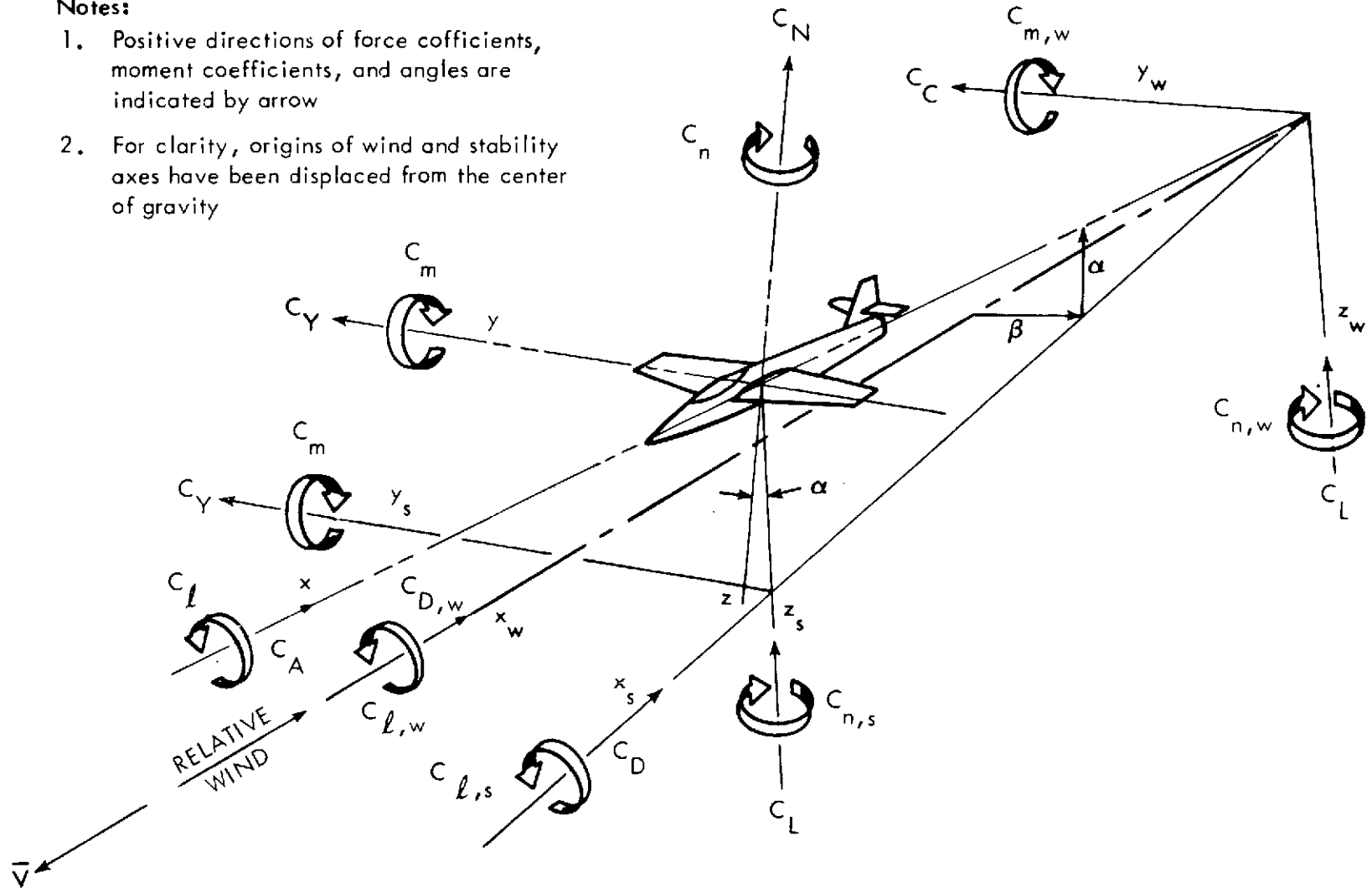
Figure 1.— Axes system showing direction and sense of force and moment coefficients, angle of attack, and sideslip angle.

DIMENSIONS IN METERS

14°
0.001588

40°
.07529
0.1575
20°
3°
15°
S₁

O₁
18°
ORB. W.L. .1930
13°
3.0° 0.006858
1° UP
0.02316
0.1915
0.3378
0.5005
0.9207

(a) 040A integrated vehicle.

DIMENSIONS IN METERS

B1 C1
B.L. 0.2128
0.4257
B.L. 0.000
W1
P_IV
F.S. 0.7130
V₂
0.01880
0.1782   0.2843
W.L. 0.1930
W.L. 0.2413
W.L. 0.1352
0.6346
0.09845
0.09652
F.S. 0.7311

28

DIMENSIONS IN METERS
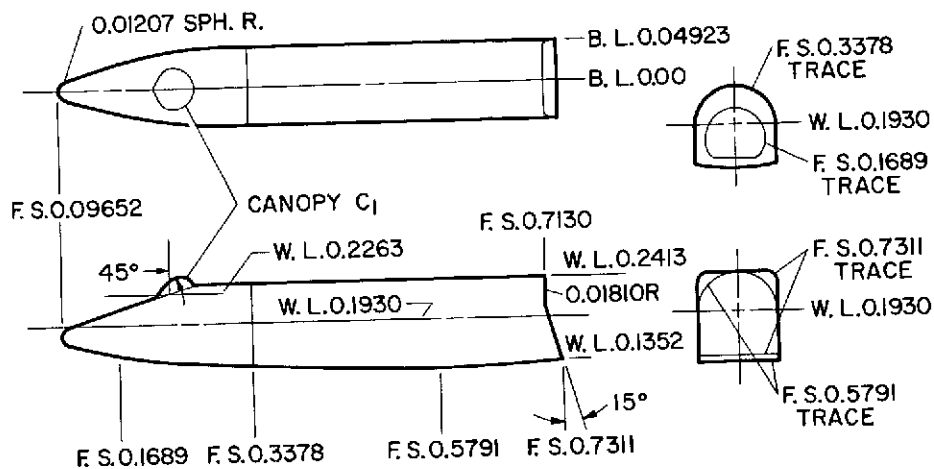
(c) Orbiter fuselage.

DIMENSIONS IN METERS
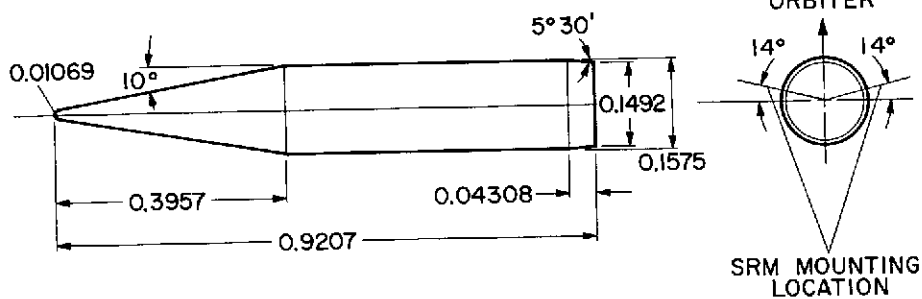
(d) EHOT.

Figure 2.— Continued.

DIMENSIONS IN METERS

0.008077

20°   0.07529   72°

0.07529

TOP
RIGHT SRM

TOP
LEFT SRM

15°

1°   1°

0.08788

0.06929

0.7483   0.03764
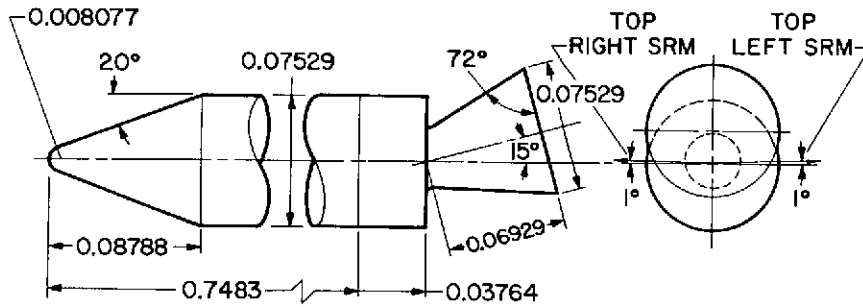
(e) Solid rocket motors, S1.

DIMENSIONS IN METERS

ONE HALF BODY OF REVOLUTION
CREATED THROUGH USE OF NASA
633-018 AIRFOIL.
TYPICAL EACH CORNER.
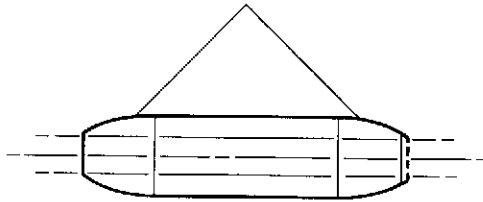
X, m	Y, m
0	0
0.0002769	0.0008941
0.0004140	0.001092
0.0006883	0.001412
0.001379	0.001979
0.002758	0.002779
0.004138	0.003381
0.005514	0.003866
0.008273	0.004602
0.01103	0.005126
0.01379	0.005479
0.01655	0.005677
0.01930	0.005733

L.E. RAD.=0.001168

0.01930   0.01930

0.04971   0.005733

0.009652

Y   X   34°

0.009652   0.01147
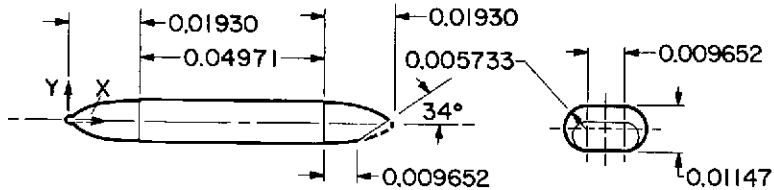
(f) Vertical tail ACPS pods P1V.

Figure 2.– Continued.

NOTE: ALL DIMENSIONS ARE MODEL SCALE IN METERS
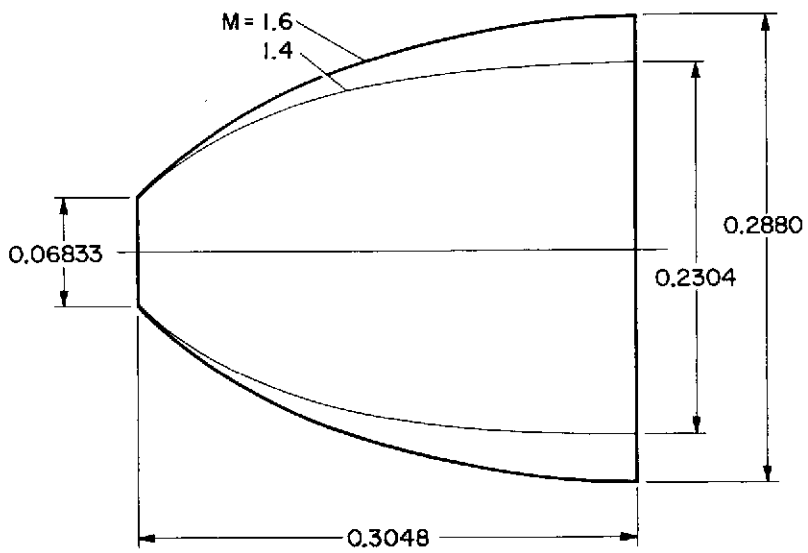
(g) SRM plumes.

Figure 2.— Concluded.
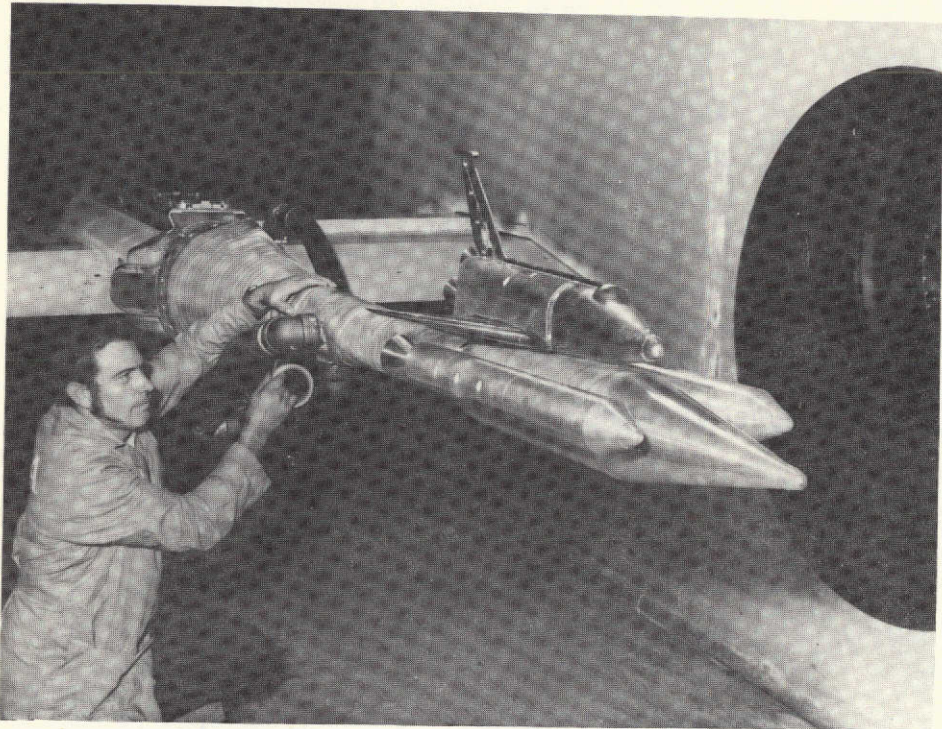
(a) Front view.
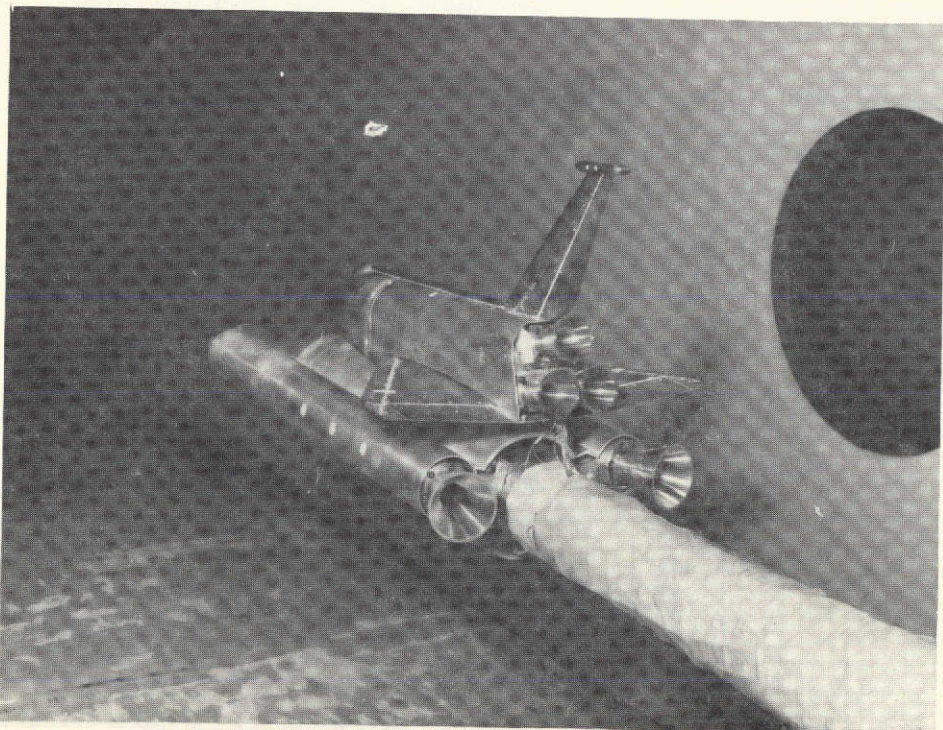
(b) Rear view.

Figure 3.– Installation of the 0.019-scale model launch configuration of the Space Shuttle Vehicle with the 040A orbiter.
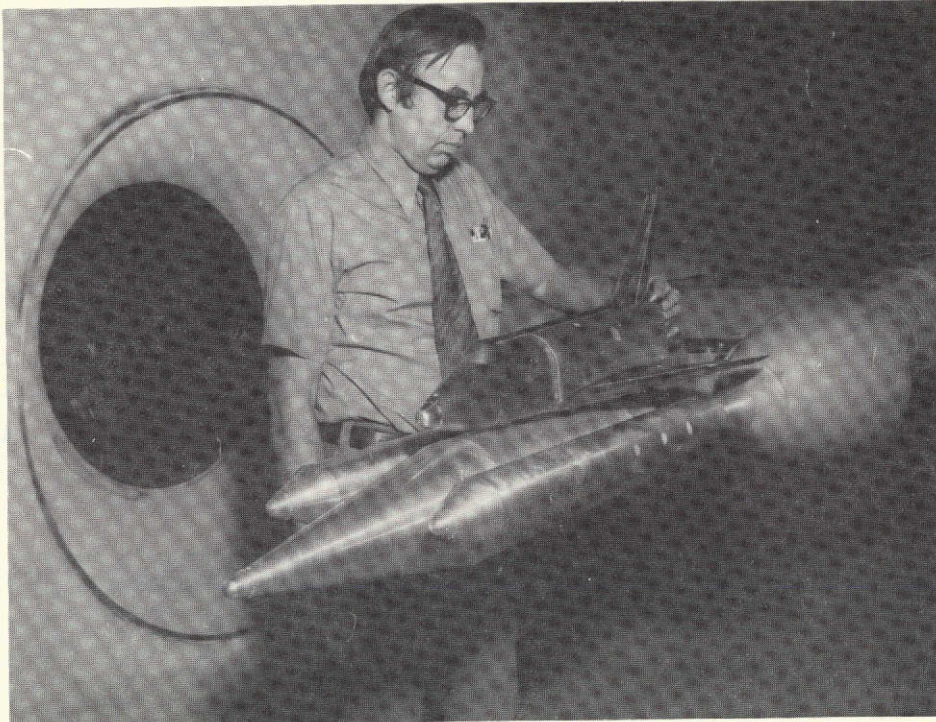
(c) Front view with $M = 1.4$ nozzle design solid plume simulators.

Figure 3.– Concluded.
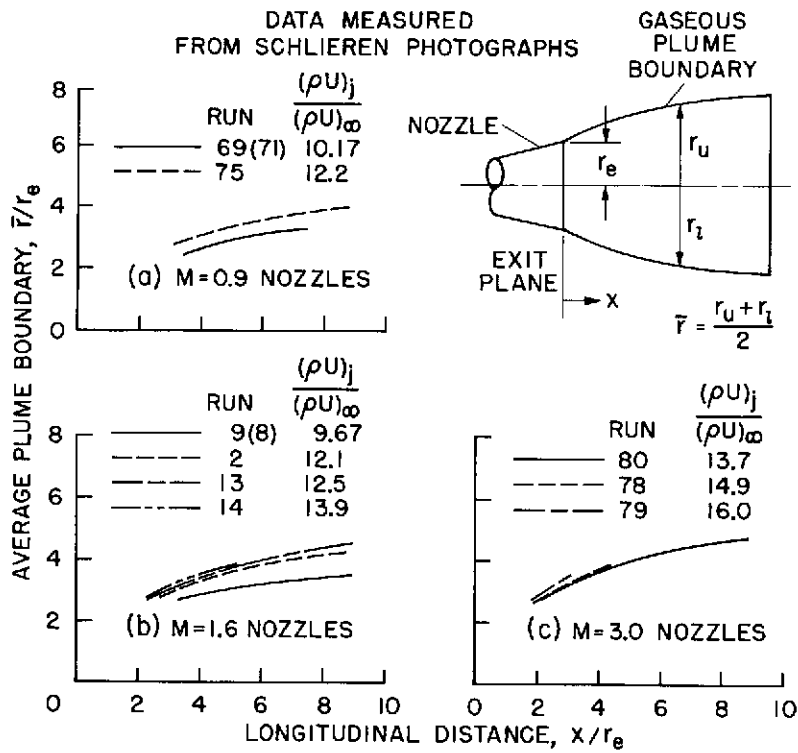
Figure 4.– Average plume shape variations with the viscous mixing parameter $(\rho U)_j/(\rho U)_\infty$ for various SRM nozzle designs at $M = 1.6$.
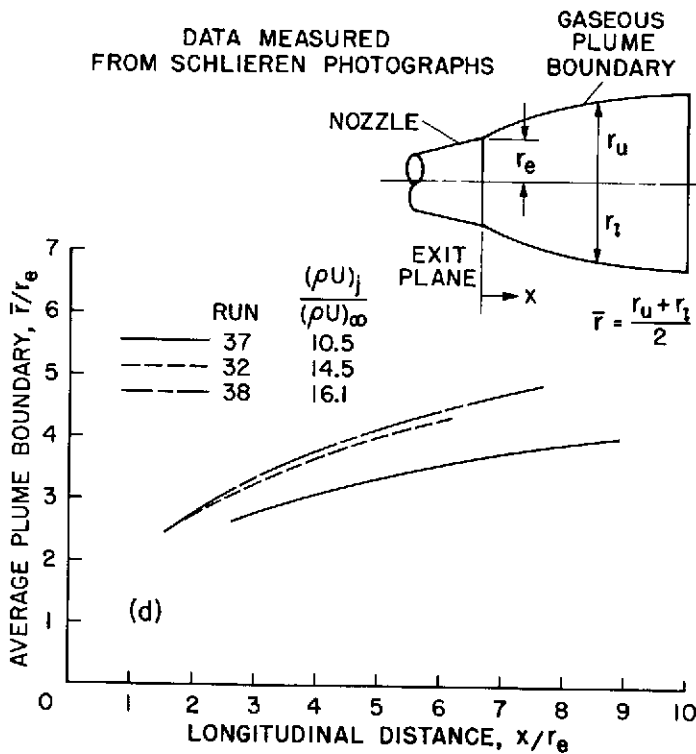
Figure 5.– Average SRM plume shape variations with the viscous mixing parameter $(\rho U)_j/(\rho U)_\infty$ for $M = 2.0$ nozzle design at $M = 2.0$.
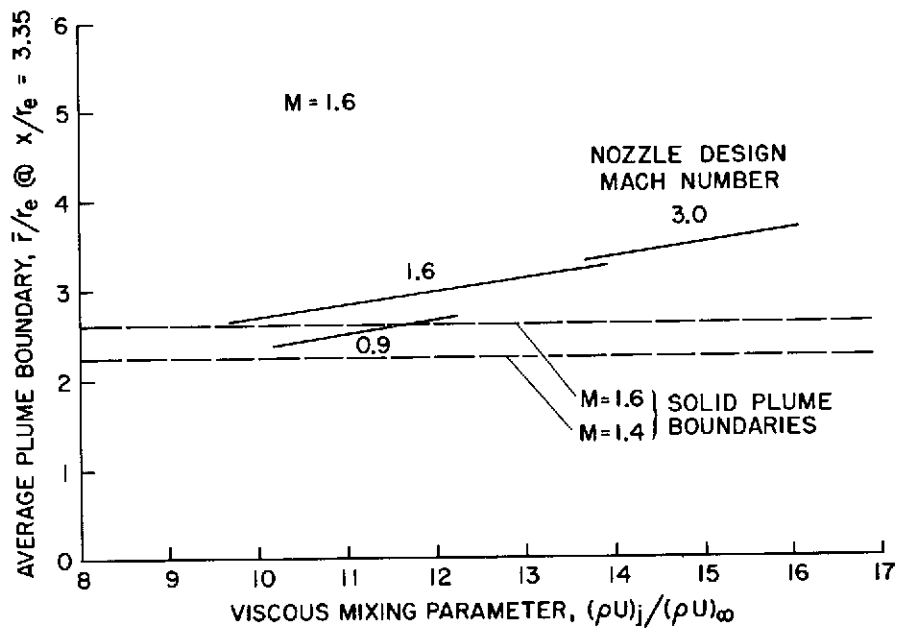
Figure 6.— Variation of the average gaseous SRM plume shape with the viscous mixing parameter at a given distance from the nozzle exit.
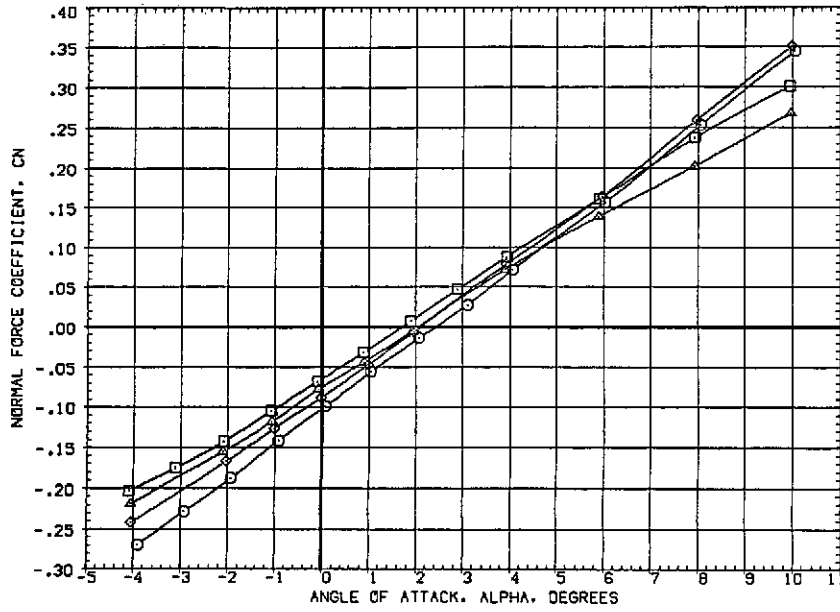
(a) Normal force vs. angle of attack at $M = 1.60$.
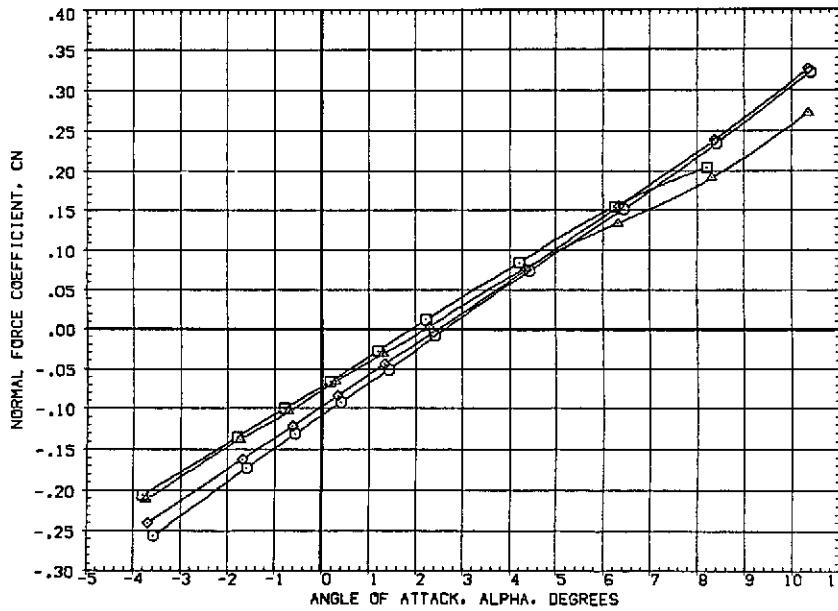
(b) Normal force vs. angel of attack at $M = 1.98$.

Figure 7.– Effect of plume size on the longitudinal characteristics at $\beta = 0°$.

36

$\delta_e = \delta_a = \delta_r = 0°$

○ No plumes
□ Nominal plumes (P_c/P_{t_∞} Nom; SRM $A/A^* = 8$)
◇ Smaller SRM plumes (Nom. orb. plumes; SRM $A/A^* = 12$)
△ Larger plumes (Orb. and SRM $P_c/P_{t_\infty} = 1.3$ Nom.)
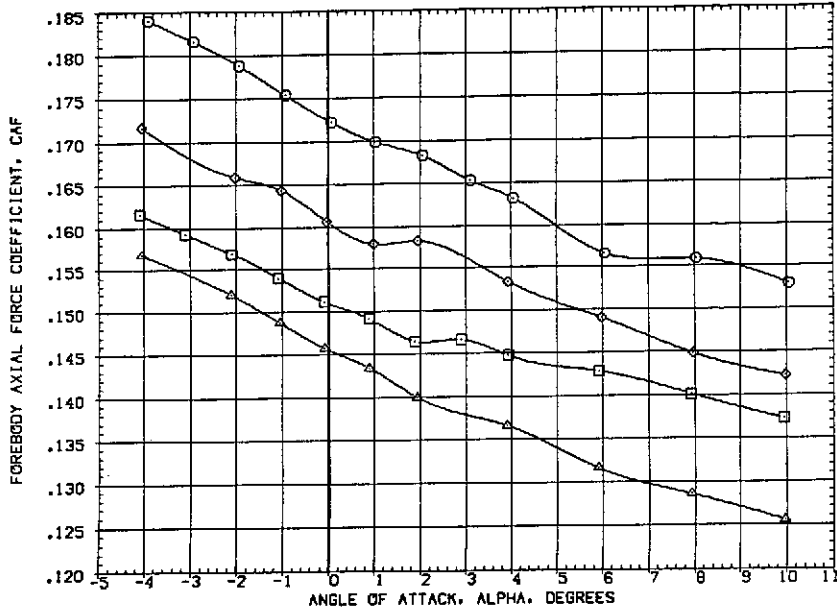
(c) Forebody axial force at $M = 1.60$.
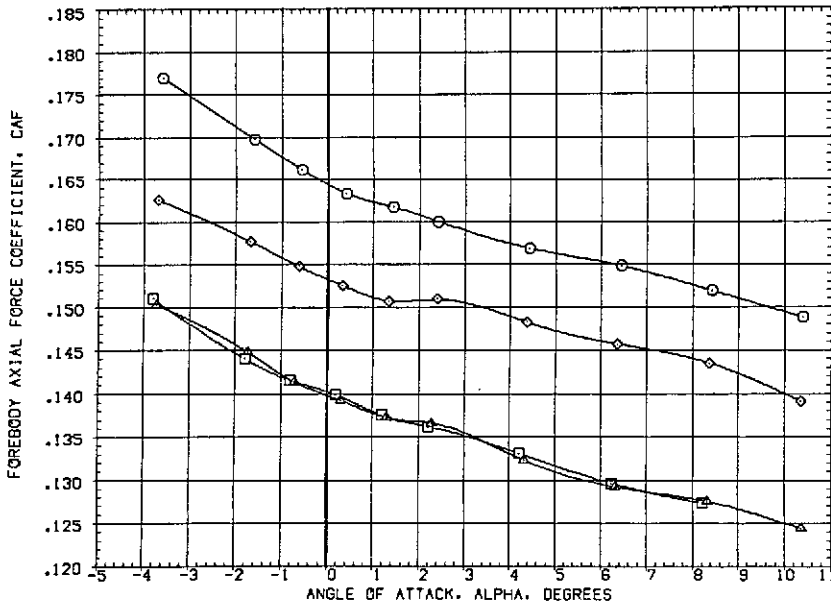
(d) Forebody axial force at $M = 1.98$.

Figure 7.– Continued.

37

$\delta_c = \delta_a = \delta_r = 0°$

○ No plumes
□ Nominal plumes $(P_c/P_{t_\infty}$ Nom; SRM $A/A^* = 8)$
◇ Smaller SRM plumes (Nom. orb. plumes; SRM $A/A^* = 12$)
△ Larger plumes (Orb. and SRM $P_c/P_{t_\infty} = 1.3$ Nom.)

(e) Pitching moment at $M = 1.60$.
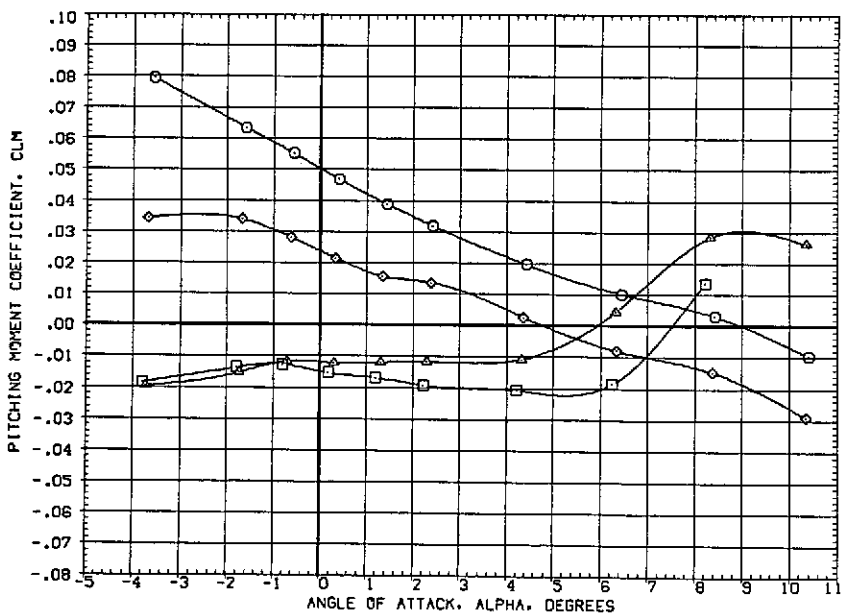
(f) Pitching moment at $M = 1.98$.

Figure 7.– Continued.

38

○   No plumes
□   Nominal plumes (P_c/P_{t_∞} Nom; SRM $A/A^* = 8$)
◇ .   Smaller SRM plumes (Nom. orb. plumes; SRM $A/A^* = 12$)
△   Larger plumes (Orb. and SRM $P_c/P_{t_\infty} = 1.3$ Nom.)
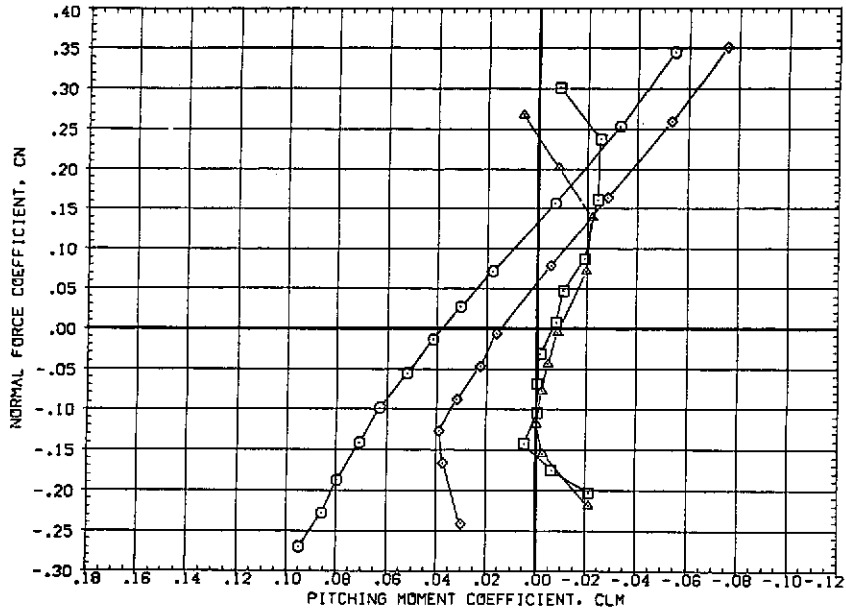
(g) Normal force vs. pitching moment at $M = 1.6$.
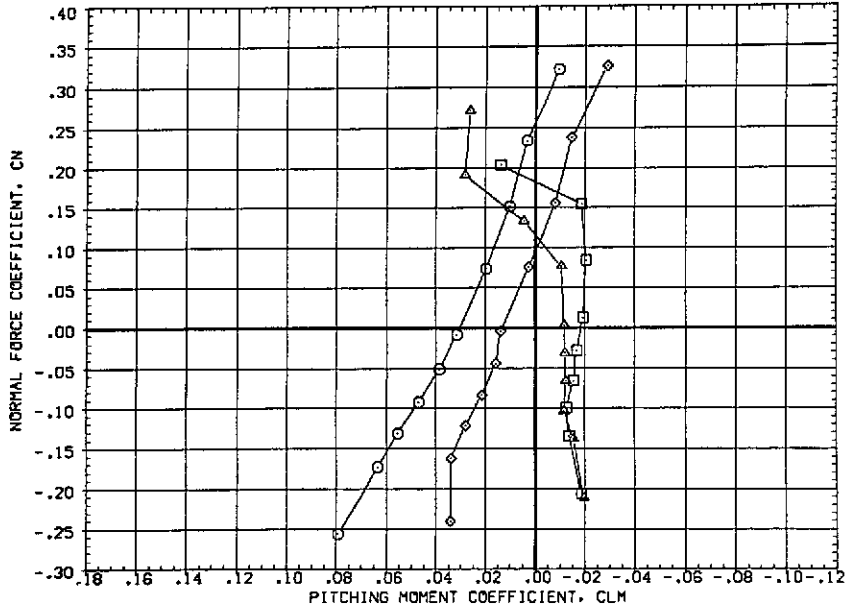
(h) Normal force vs. pitching moment at $M = 1.98$.
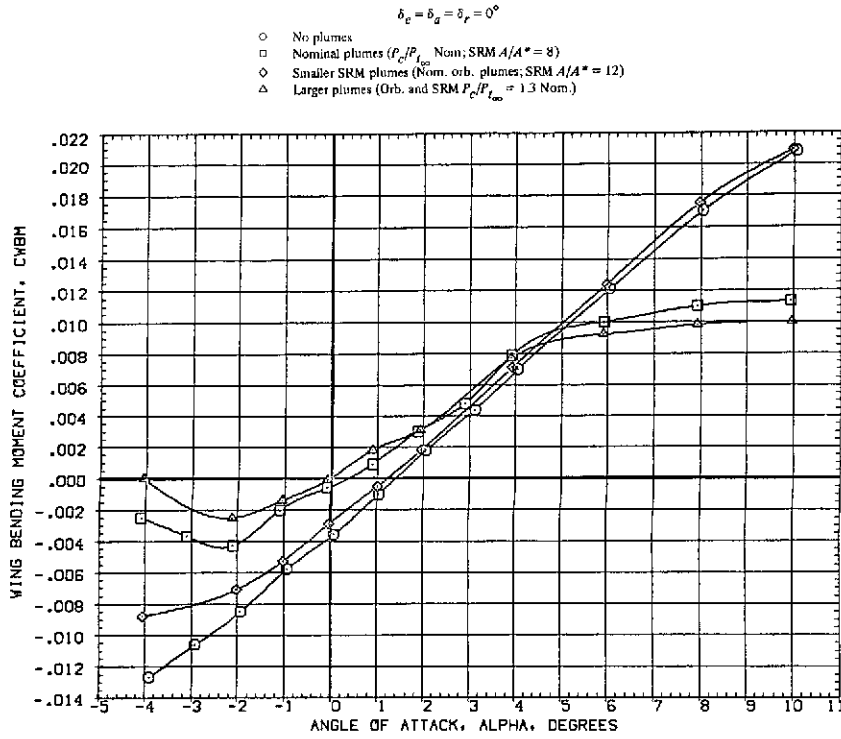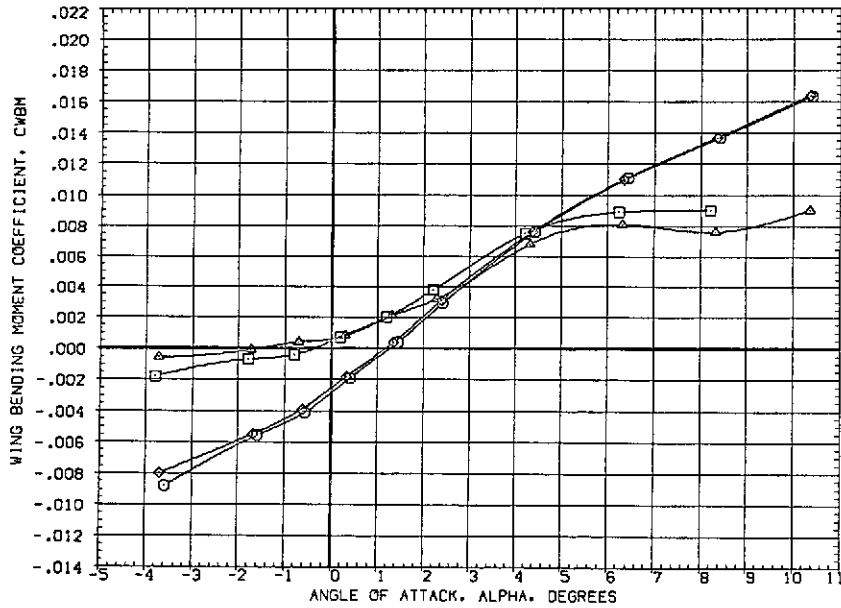
Figure 7.– Continued.

39

$\delta_e = \delta_a = \delta_r = 0°$

○   No plumes
□   Nominal plumes $(P_c/P_{t_\infty}$ Nom; SRM $A/A^* = 8)$
◇   Smaller SRM plumes (Nom. orb. plumes; SRM $A/A^* = 12$)
△   Larger plumes (Orb. and SRM $P_c/P_{t_\infty} = 1.3$ Nom.)

(i) Wing bending moment at $M = 1.6$.

(j) Wing bending moment at $M = 1.98$.

Figure 7.-- Continued.

40

$\delta_e = \delta_a = \delta_r = 0°$

○   No plumes
□   Nominal plumes $(P_c/P_{t_\infty}$ Nom; SRM $A/A^* = 8)$
◇   Smaller SRM plumes (Nom. orb. plumes; SRM $A/A^* = 12)$
△   Larger plumes (Orb. and SRM $P_c/P_{t_\infty} = 1.3$ Nom.)
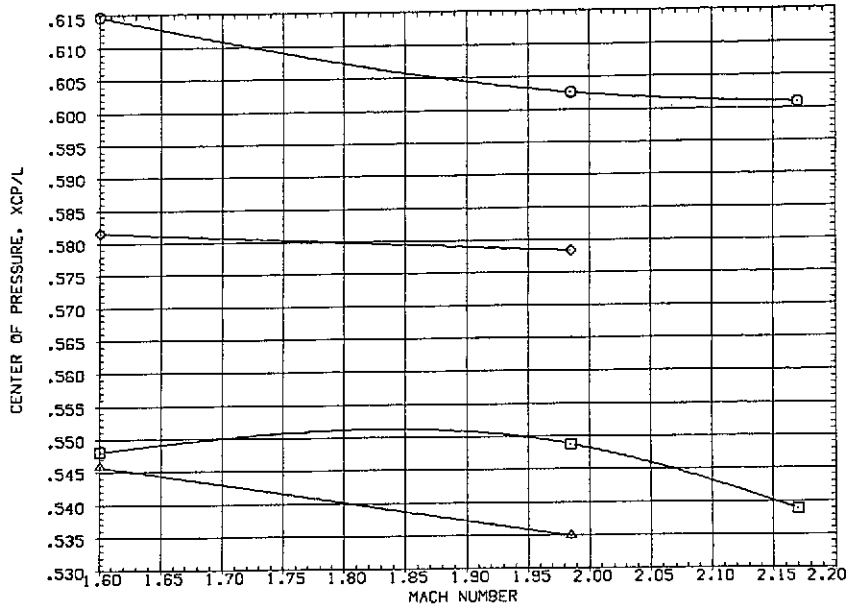
(k) Center of pressure vs. M.
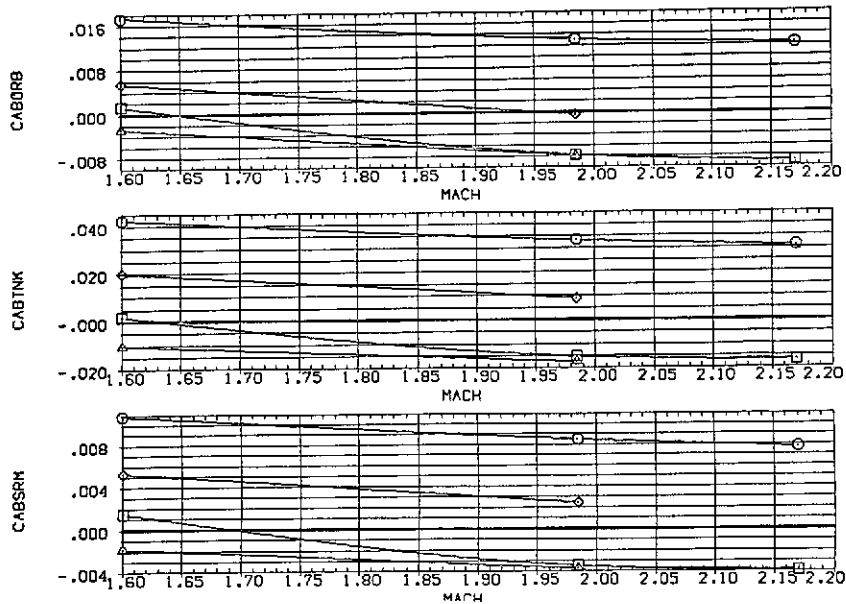
(l) Base forces vs. M.

Figure 7.— Concluded.

$$\delta_e = \delta_a = \delta_r = 0°$$

○ No plumes
□ Nominal plumes (P_c/P_{t_∞} Nom; SRM $A/A^* = 8$)
◇ Smaller SRM plumes (Nom. orb. plumes; SRM $A/A^* = 12$)
△ Larger plumes (Orb. and SRM $P_c/P_{t_\infty} = 1.3$ Nom)
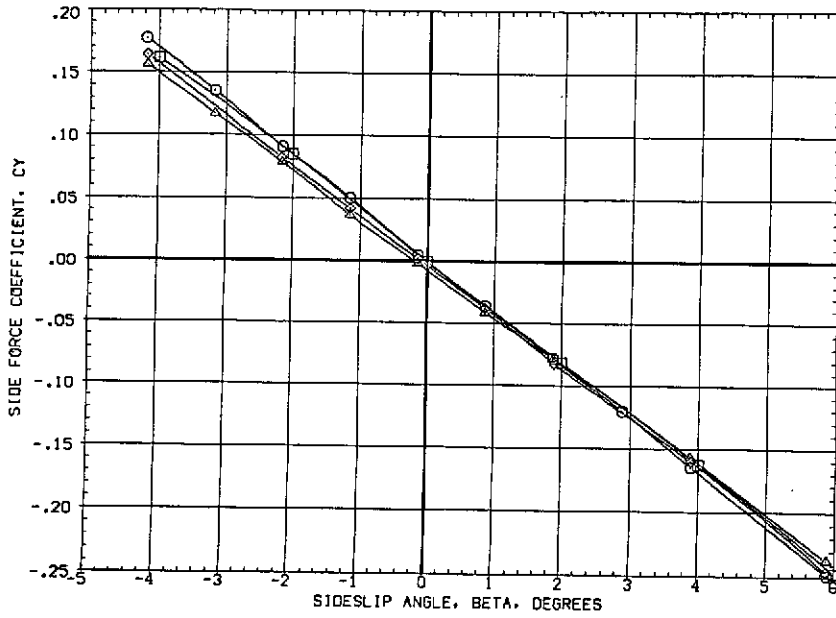
(a) Side force at $M = 1.6$.
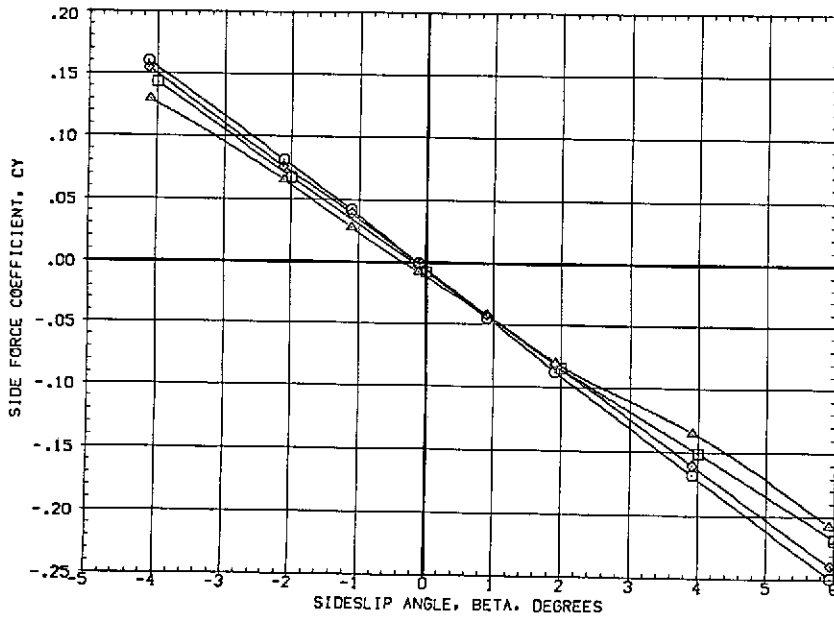
(b) Side force at $M = 1.98$.

Figure 8.— Effect of plume size on the lateral characteristics at $\alpha = 0°$.

(c) Yawing moment at $M = 1.60$.

(d) Yawing moment at $M = 1.98$.

Figure 8.– Continued.

$\delta_e = \delta_a = \delta_r = 0°$

○ No plumes
□ Nominal plumes (P_c/P_{t_∞} Nom; SRM $A/A^* = 8$)
◇ Smaller SRM plumes (Nom. orb. plumes; SRM $A/A^* = 12$)
△ Larger plumes (Orb. and SRM $P_c/P_{t_\infty} = 1.3$ Nom)

(e) Rolling moment at $M = 1.60$.

(f) Rolling moment at $M = 1.98$.

Figure 8.– Continued.

44

(g) Pitching moment at $M = 1.60$.

(h) Pitching moment at $M = 1.98$.

Figure 8.– Continued.

○ No plumes
□ Nominal plumes $(P_c/P_t, \text{ Nom}; \text{SRM } A/A^* = 8)$
◊ Smaller SRM plumes (Nom. orb. plumes; SRM $A/A^* = 12$)
△ Larger plumes (Orb. and SRM $P_c/P_{t_\infty} = 1.3$ Nom.)
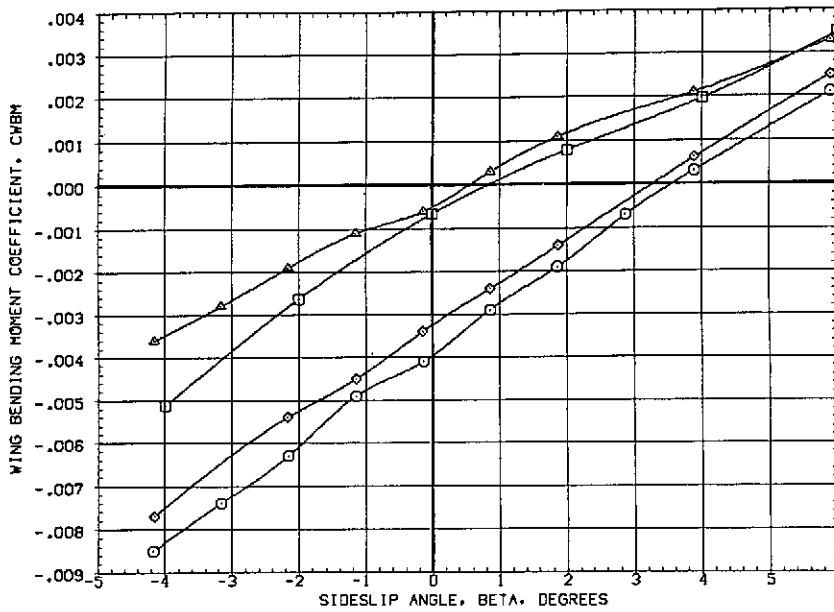
(i) Wing bending moment at $M = 1.60$.
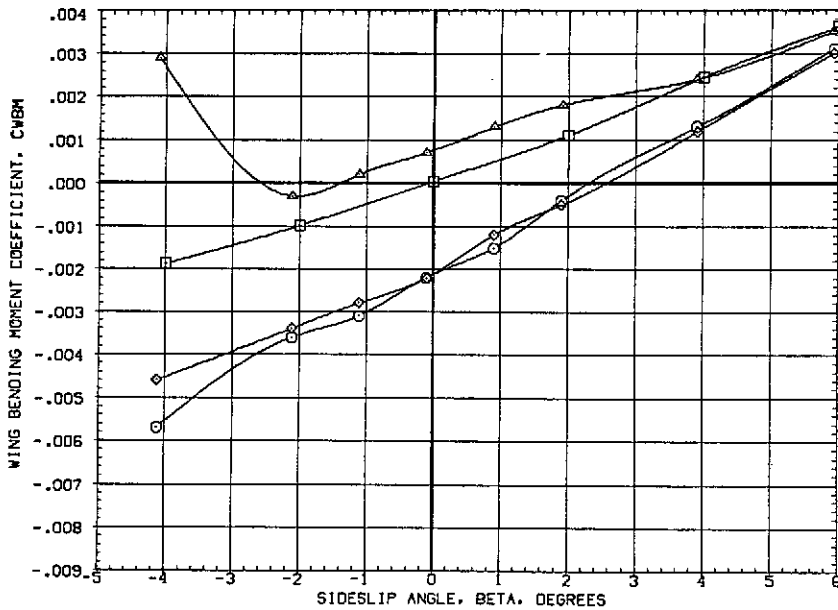
(j) Wing bending moment at $M = 1.98$.

Figure 8.– Concluded.

$$\delta_e = \delta_a = \delta_r = 0°$$

	Nozzle design, M	P_c/P_{∞}	
		SRM	Orb.
○	1.6	Nom. ($A/A^* = 8$)	Nom.
□	0.9	0.82 Nom.	—
◇	0.9	1.10 Nom.	—
△	3.0	Nom. ($A/A^* = 8$)	—
⊿	3.0	1.2 Nom.	—
◁	3.0	0.8 Nom.	—
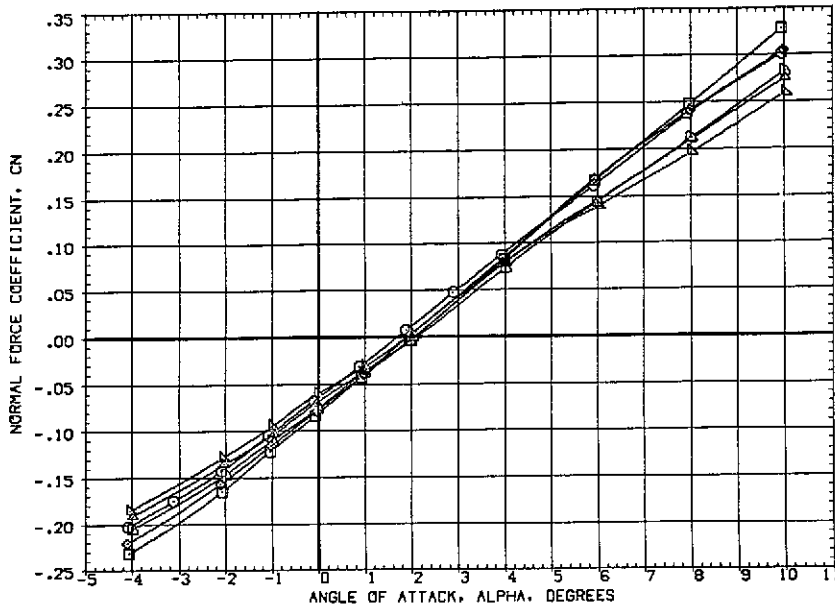
(a) Normal force vs. angle of attack.
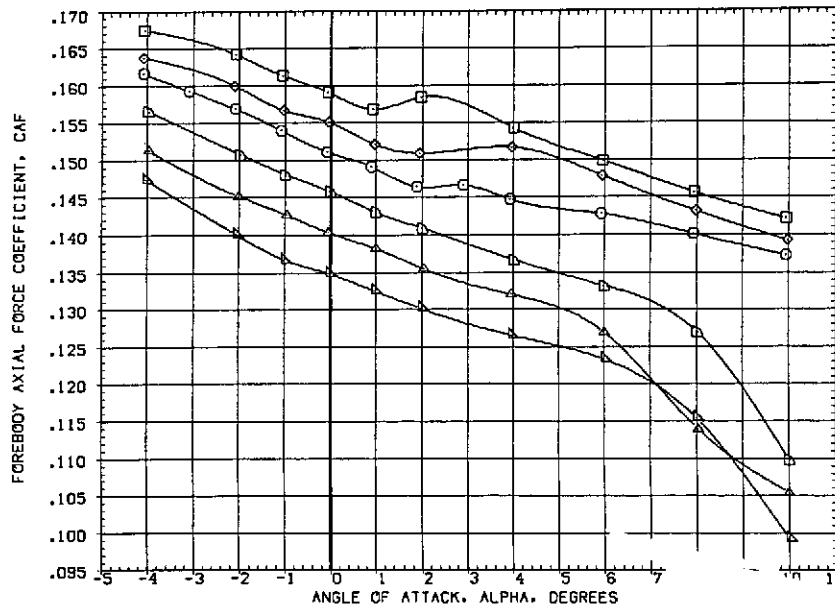
(b) Forebody axial force.

Figure 9.— Effect of nozzle design point on the longitudinal characteristics at $\beta = 0°$ and $M = 1.60$.

$$\delta_e = \delta_a = \delta_r = 0°$$

	Nozzle design, M	P_c/P_{t_∞}	
		SRM	Orb.
○	1.6	Nom. $(A/A^* = 8)$	Nom.
□	0.9	0.82 Nom.	—
◇	0.9	1.10 Nom.	—
△	3.0	Nom. $(A/A^* = 8)$	—
◁	3.0	1.2 Nom.	—
▷	3.0	0.8 Nom.	—
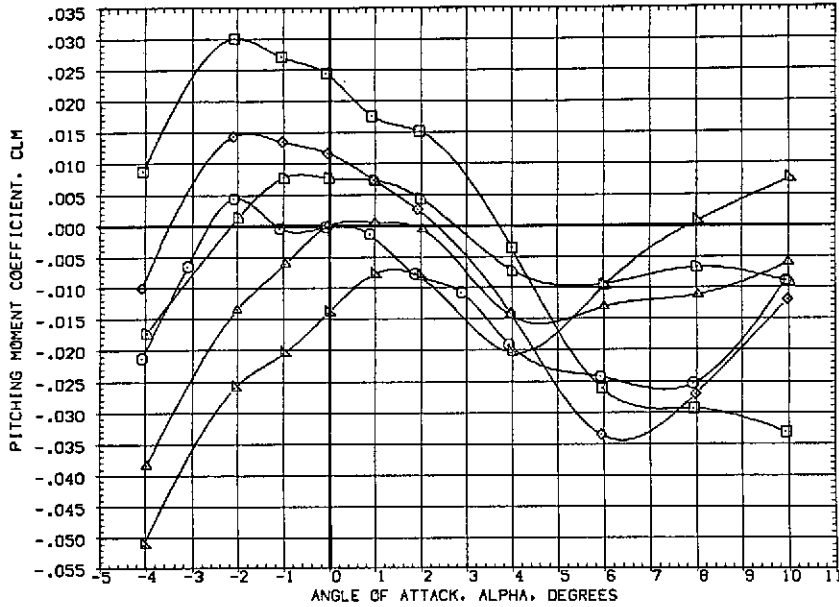
(c) Pitching moment.
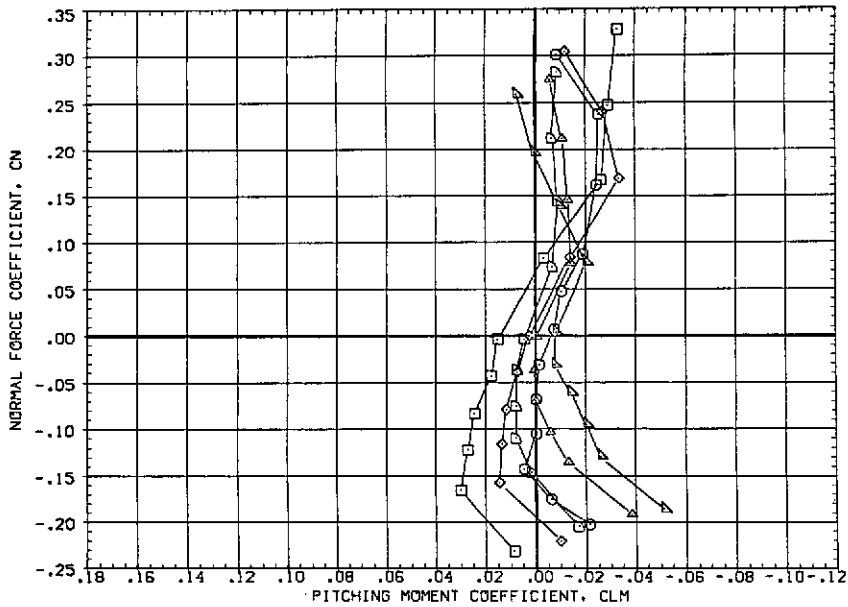
(d) Normal force vs. pitching moment.

Figure 9.— Continued.

48
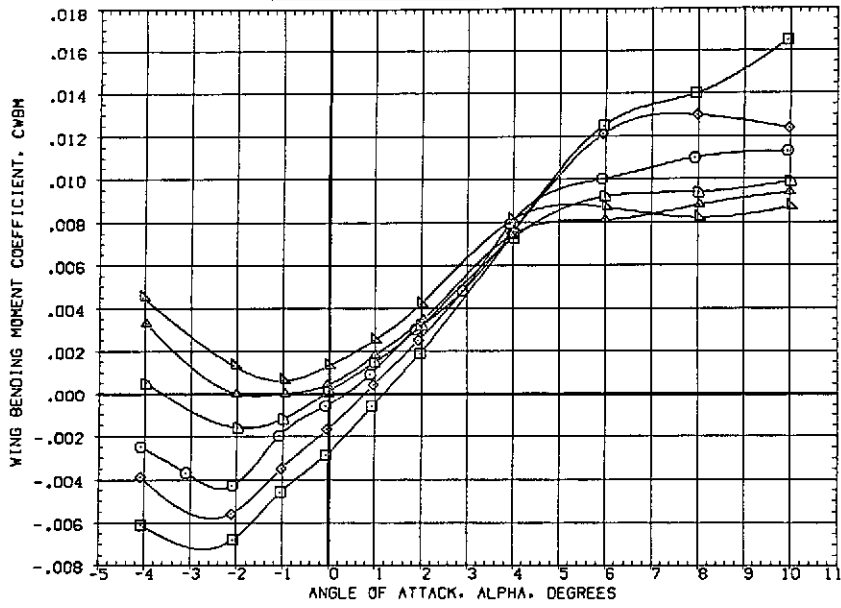
(e) Wing bending moment.

Figure 9.– Concluded.
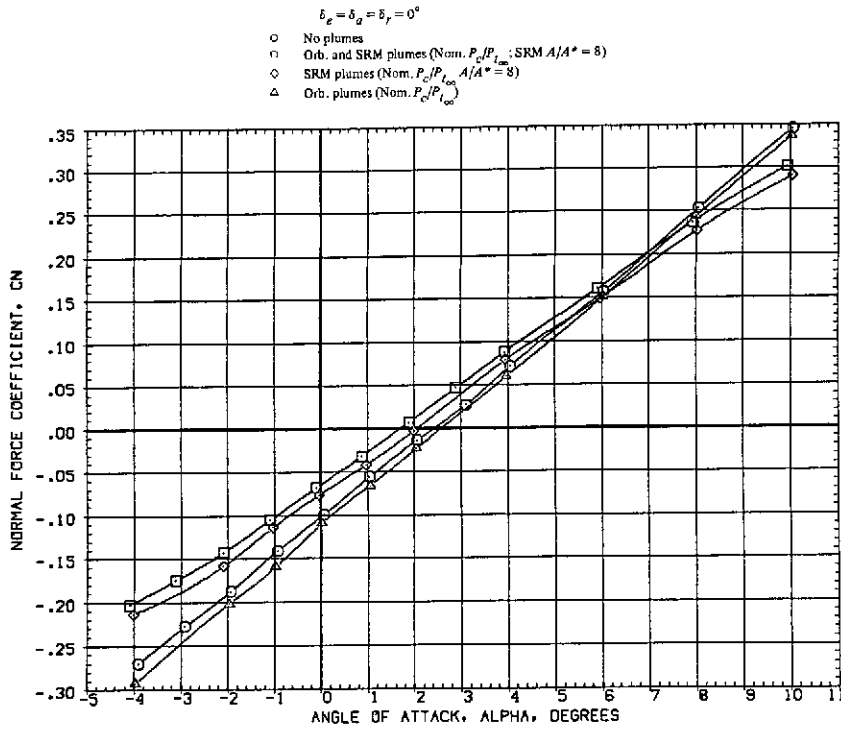
(a) Normal force vs. angle of attack at $M = 1.60$.
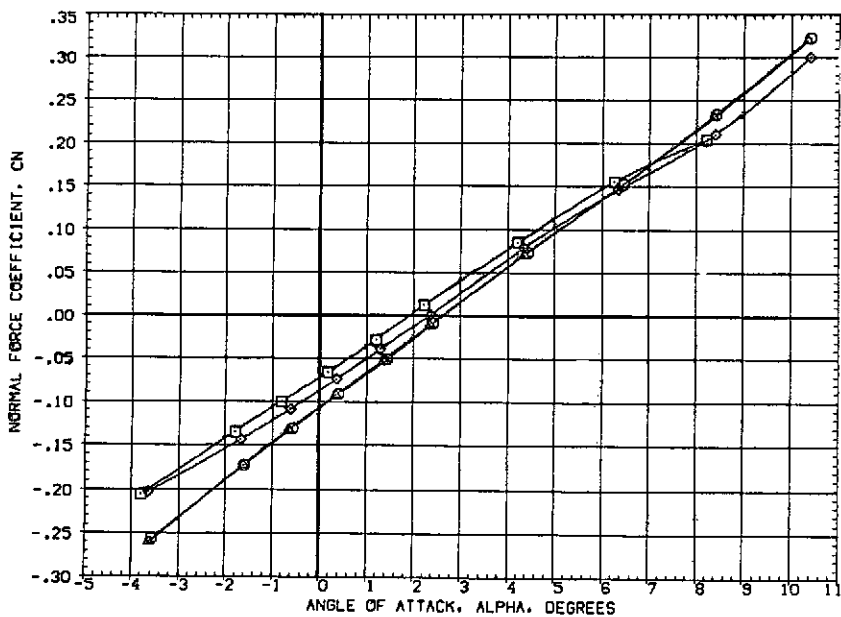
(b) Normal force vs. angle of attack at $M = 1.98$.

Figure 10.— Effect of the orbiter and the solid rocket motor (SRM) plumes on the longitudinal characteristics at $\beta = 0°$.

$\delta_e = \delta_a = \delta_r = 0°$

○ No plumes
□ Orb. and SRM plumes (Nom. P_c/P_{t_∞}; SRM $A/A^* = 8$)
◇ SRM plumes (Nom. P_c/P_{t_∞}, $A/A^* = 8$)
△ Orb. plumes (Nom. P_c/P_{t_∞})

(c) Forebody axial force at $M = 1.60$.

(d) Forebody axial force at $M = 1.98$.

Figure 10.– Continued.

51
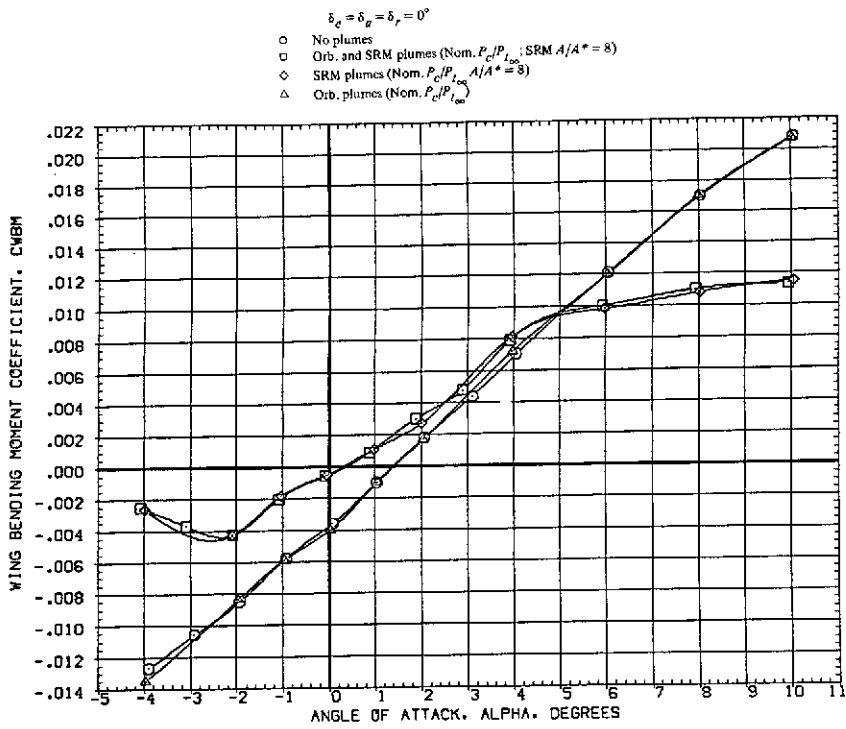
(e) Pitching moment at $M = 1.60$.

(f) Pitching moment at $M = 1.98$.

Figure 10.— Continued.

$\delta_e = \delta_a = \delta_r = 0°$

○   No plumes
□   Orb. and SRM plumes (Nom. P_c/P_{t_∞} ; SRM $A/A^* = 8$)
◇   SRM plumes (Nom. P_c/P_{t_∞} $A/A^* = 8$)
△   Orb. plumes (Nom. P_c/P_{t_∞})

(g) Normal force vs. pitching moment at $M = 1.60$.

(h) Normal force vs. pitching moment at $M = 1.98$.

Figure 10.-- Continued.

53

$\delta_e = \delta_a = \delta_r = 0°$

o   No plumes
□   Orb. and SRM plumes (Nom. P_c/P_{t_∞}; SRM $A/A^* = 8$)
◇   SRM plumes (Nom. P_c/P_{t_∞}, $A/A^* = 8$)
△   Orb. plumes (Nom. P_c/P_{t_∞})

(i) Wing bending moment at $M = 1.60$.

(j) Wing bending moment at $M = 1.98$.

Figure 10.– Continued.
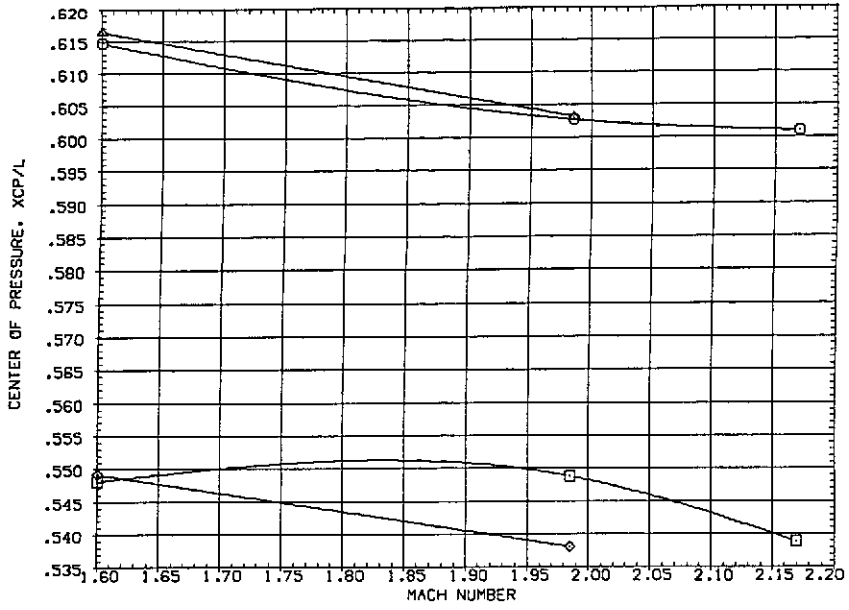
(k) Center of pressure vs. M.
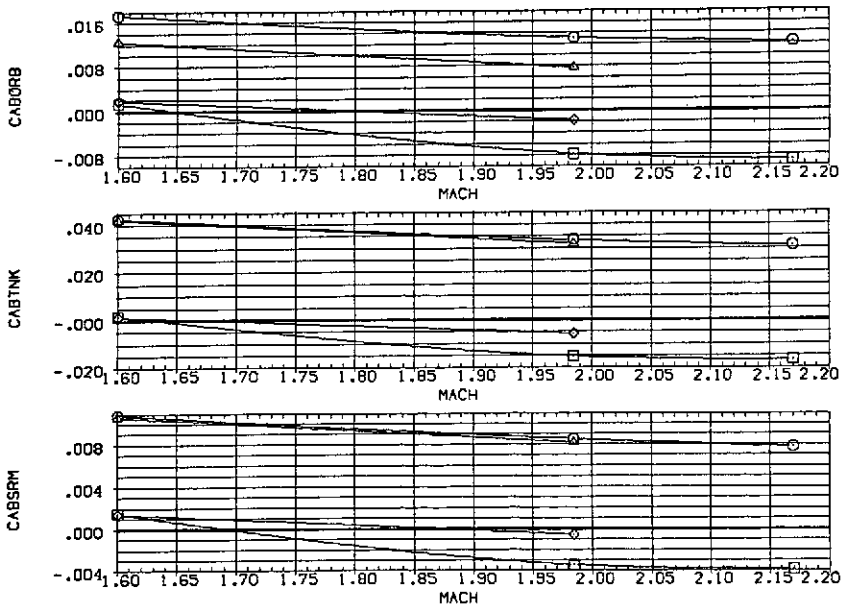
(l) Base forces vs. M.

Figure 10.– Concluded.

55
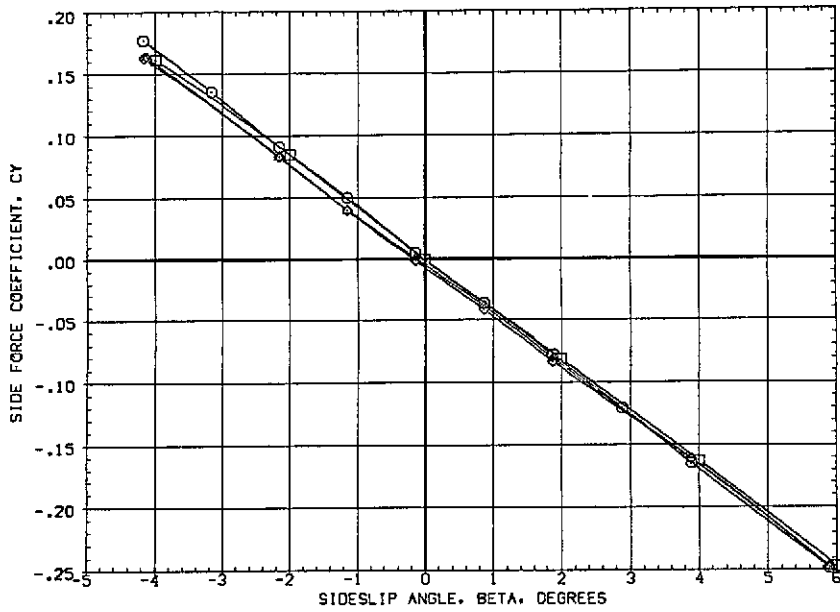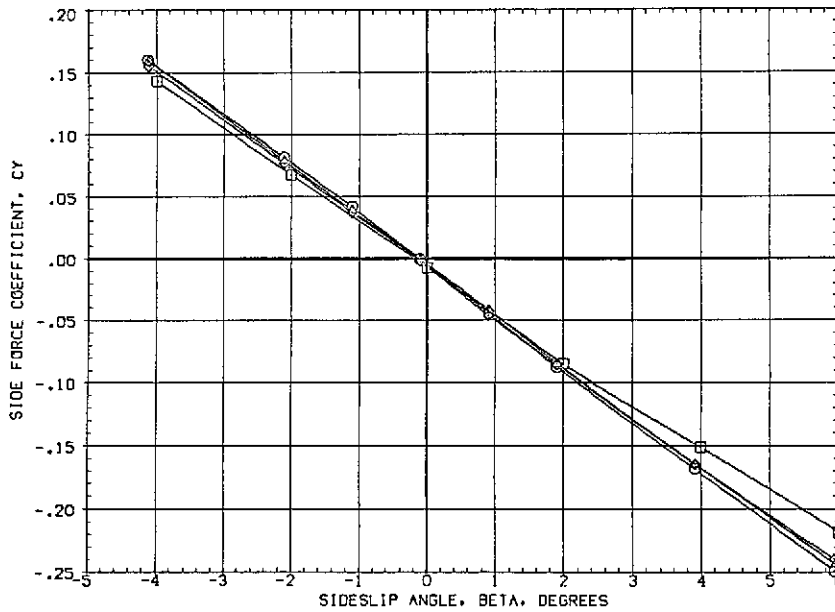
(a) Side force at $M = 1.60$.

(b) Side force at $M = 1.98$.

Figure 11.— Effect of the orbiter and the solid rocket motor (SRM) plumes on the lateral characteristics at $\alpha = 0^\circ$.
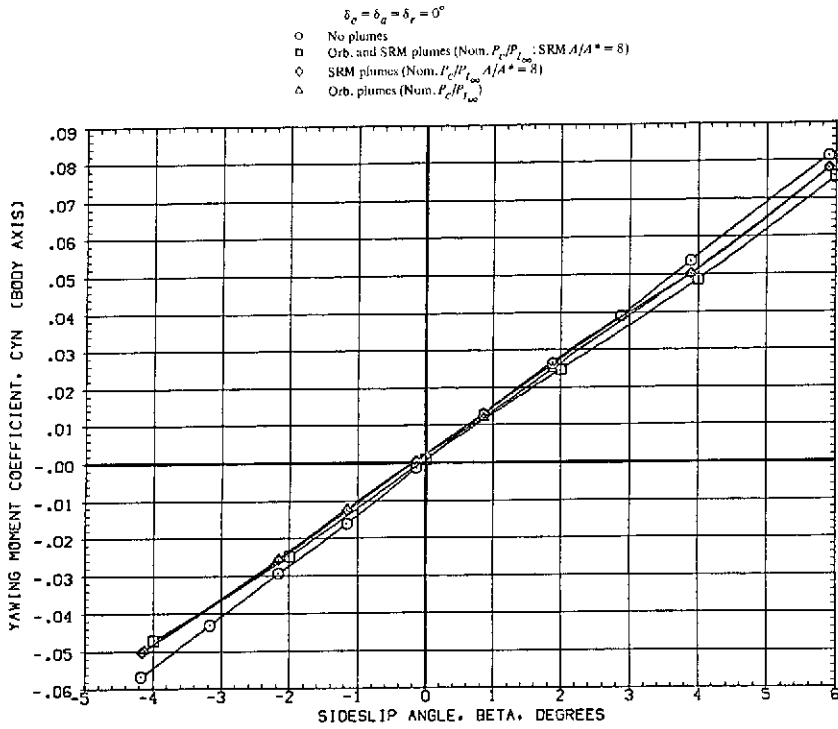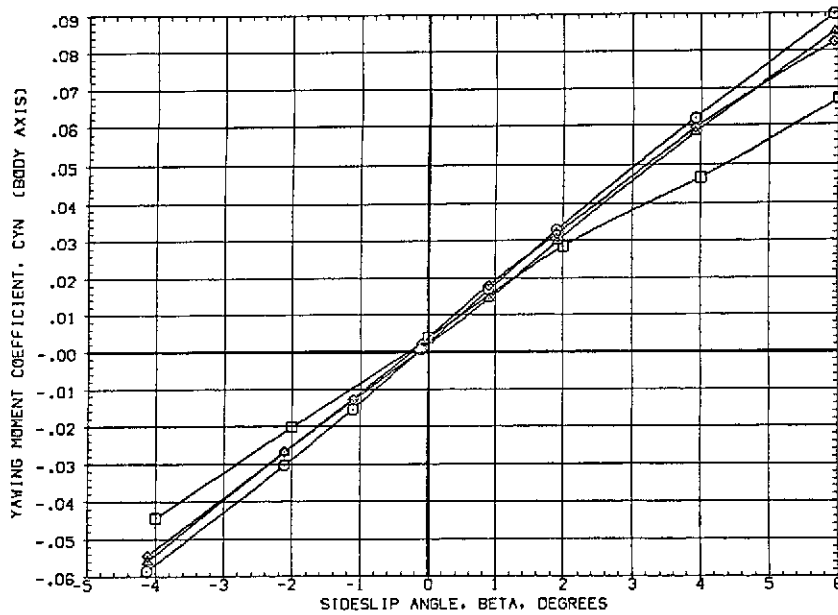
$\delta_c = \delta_a = \delta_r = 0°$

○ No plumes
□ Orb. and SRM plumes (Nom. P_c/P_{t_∞} : SRM $A/A^* = 8$)
◇ SRM plumes (Nom. P_c/P_{t_∞} $A/A^* = 8$)
△ Orb. plumes (Nom. P_c/P_{t_∞})

(c) Yawing moment at $M = 1.60$.

(d) Yawing moment at $M = 1.98$.

Figure 11.– Continued.

δ_c δ_a · δ_r = 0
No plumes
Orb. and SRM plumes (Nom. P_c/P_{t_∞} : SRM $A/A^* = 8$)
◇   SRM plumes (Nom. P_c/P_{t_∞} $A/A^* = 8$)
△   Orb. plumes (Nom. P_c/P_{t_∞})
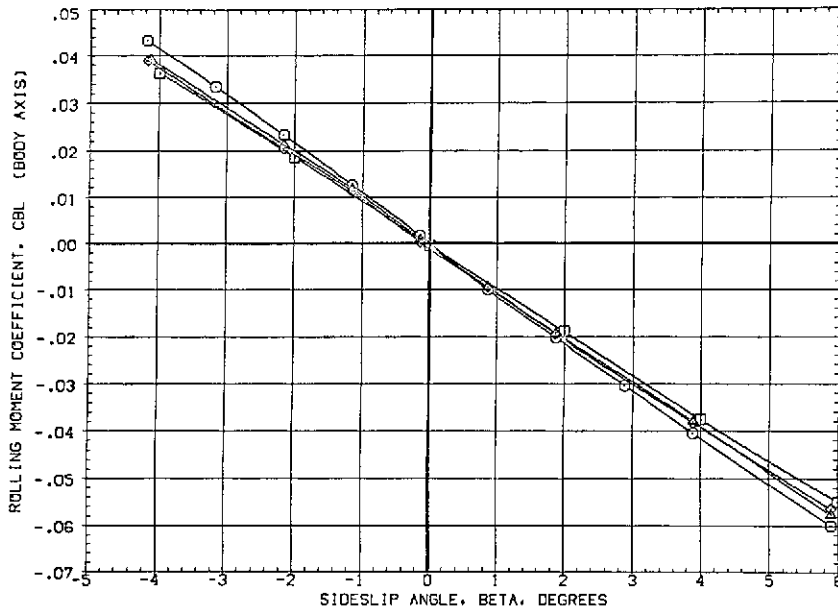
(e) Rolling moment at $M = 1.60$.
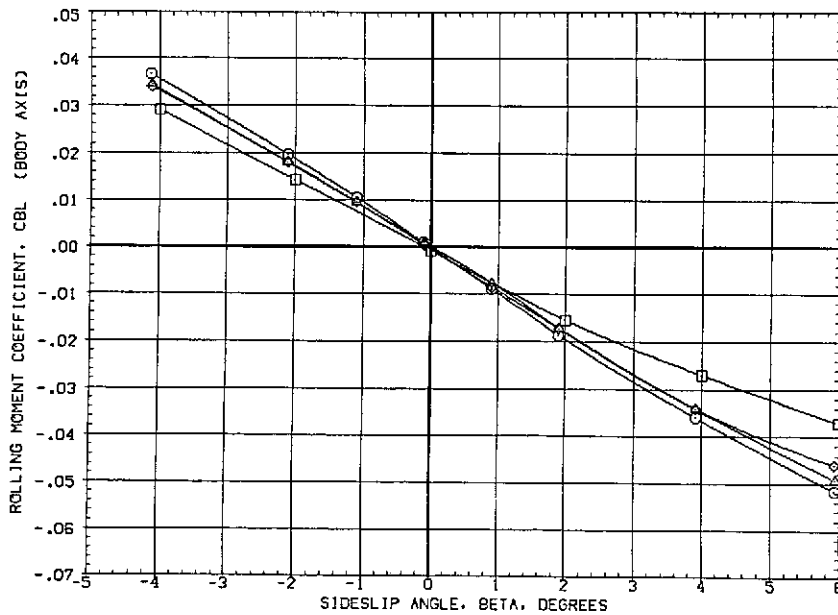
(f) Rolling moment at $M = 1.98$.

Figure 11.– Continued.
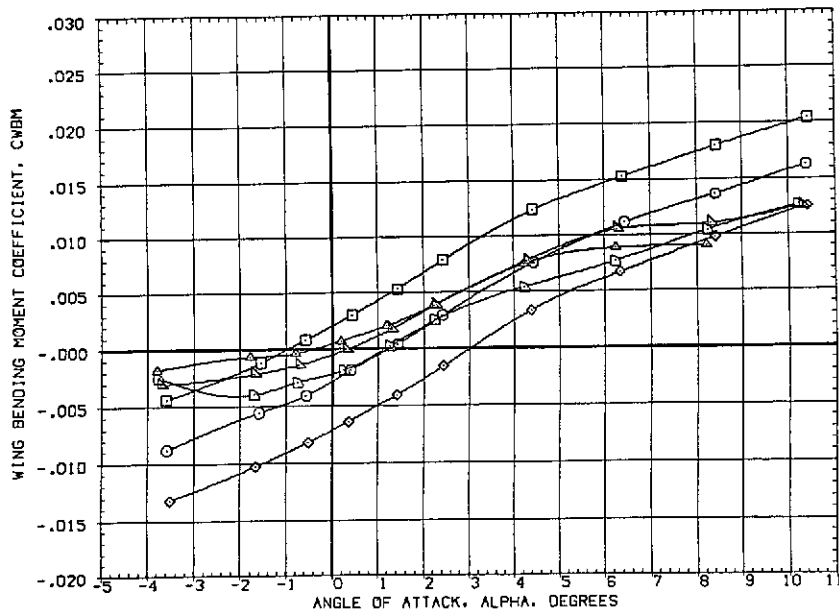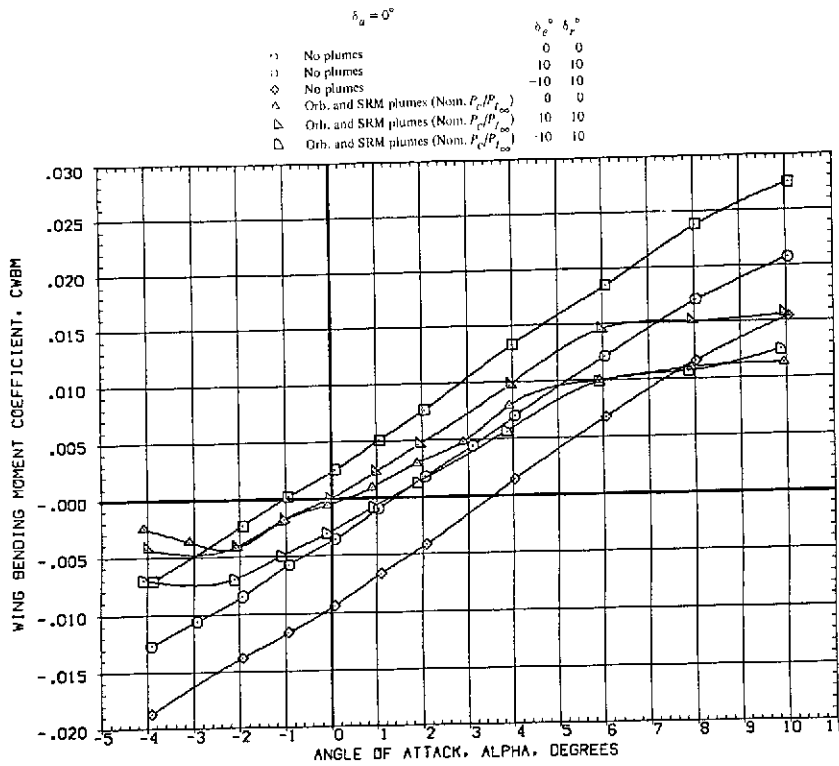
(g) Pitching moment at $M = 1.60$.
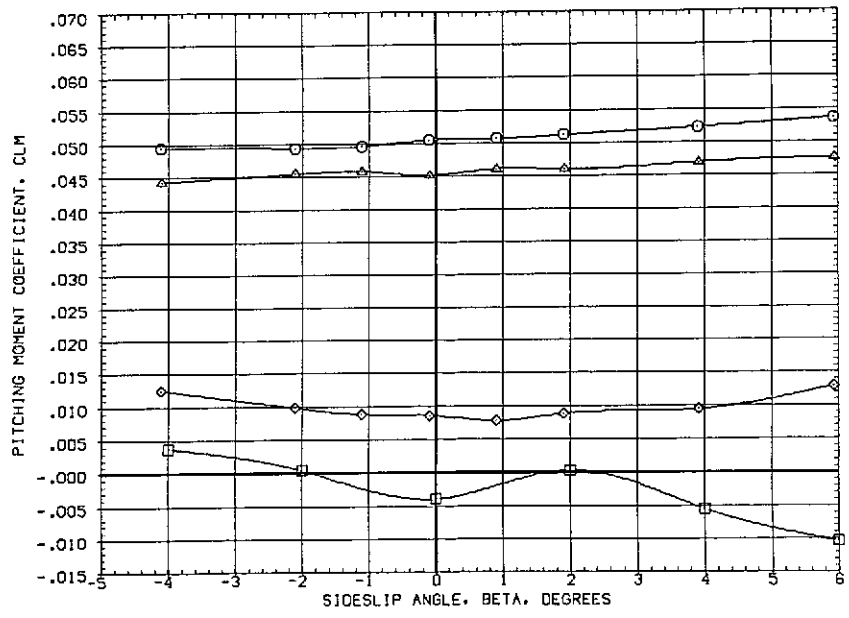
(h) Pitching moment at $M = 1.98$.

Figure 11.– Continued.

(i) Wing bending moment at $M = 1.60$.

(j) Wing bending moment at $M = 1.98$.

Figure 11.– Continued.

60
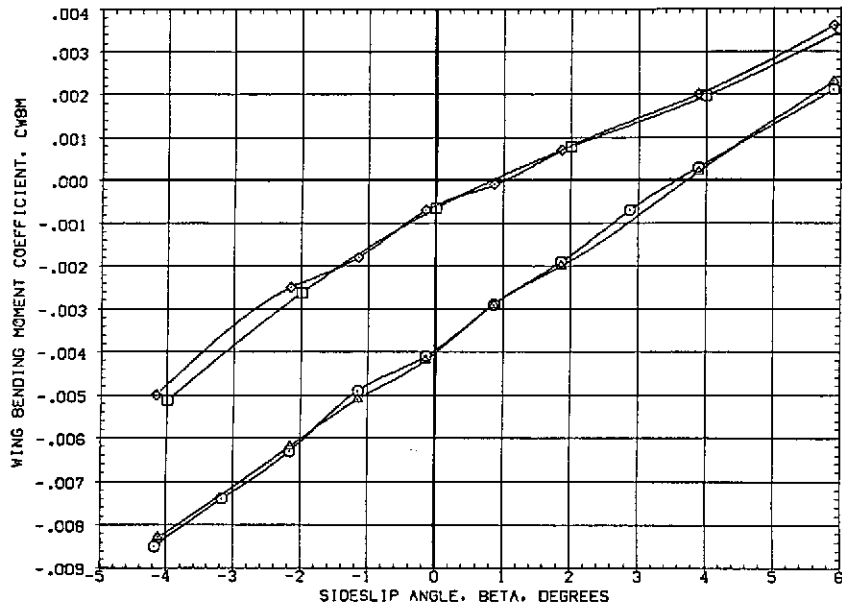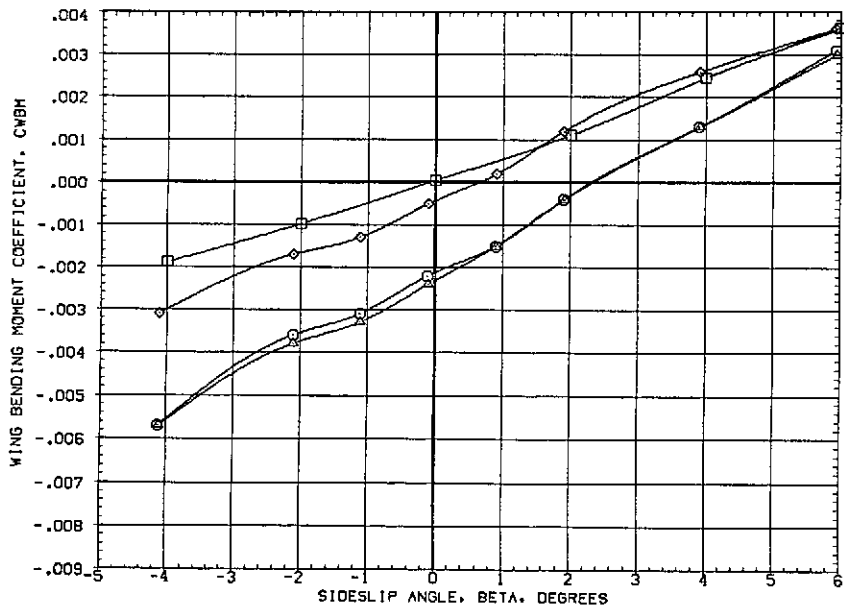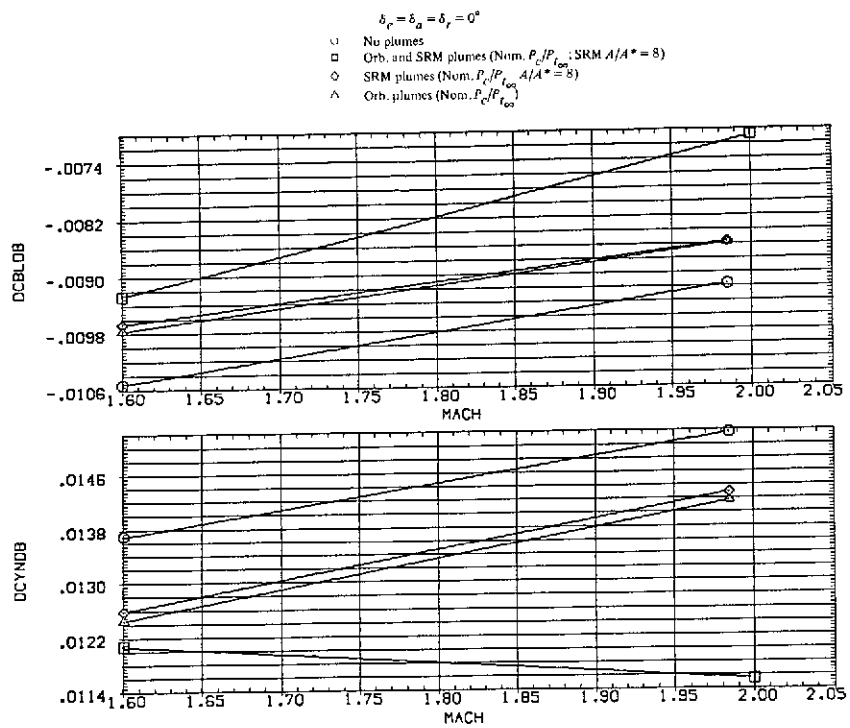
(k) Rolling and yawing-moment derivatives vs. *M*.

Figure 11.— Concluded.
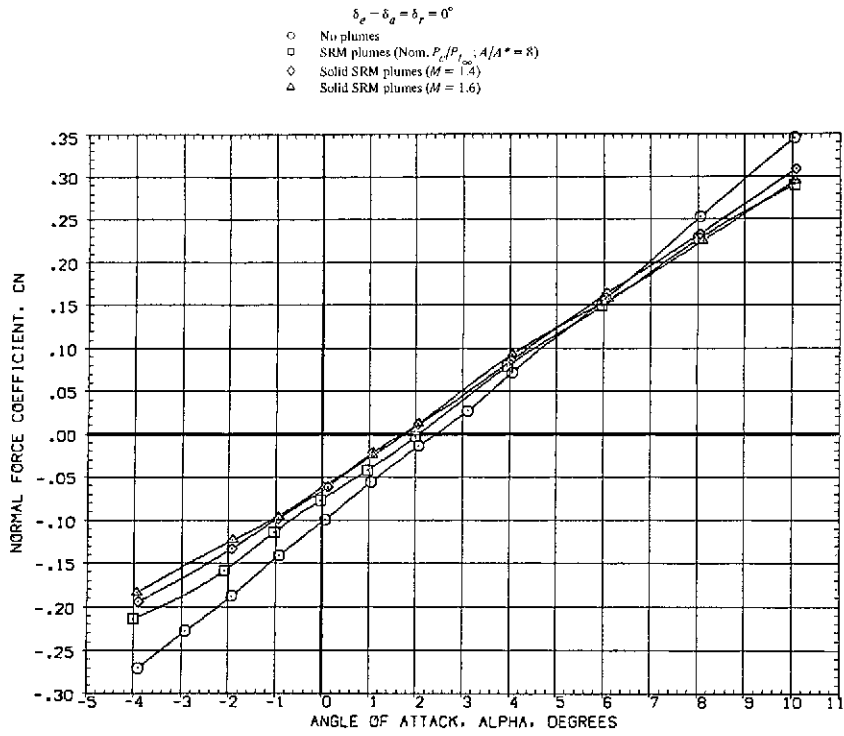
(a) Normal force vs. angle of attack.
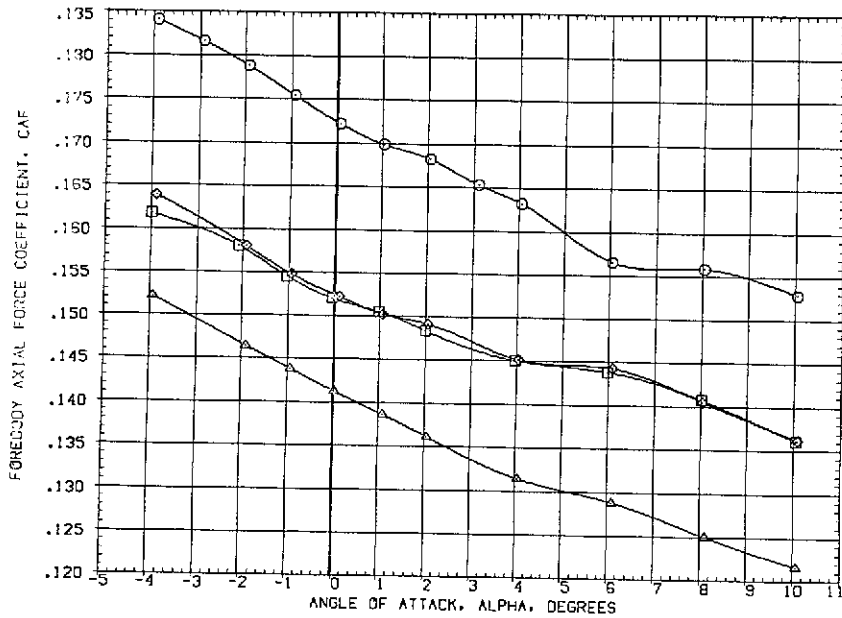
(b) Forebody axial force.

Figure 12.— Comparison of gaseous and solid simulated SRM jet plumes at $M = 1.60$.
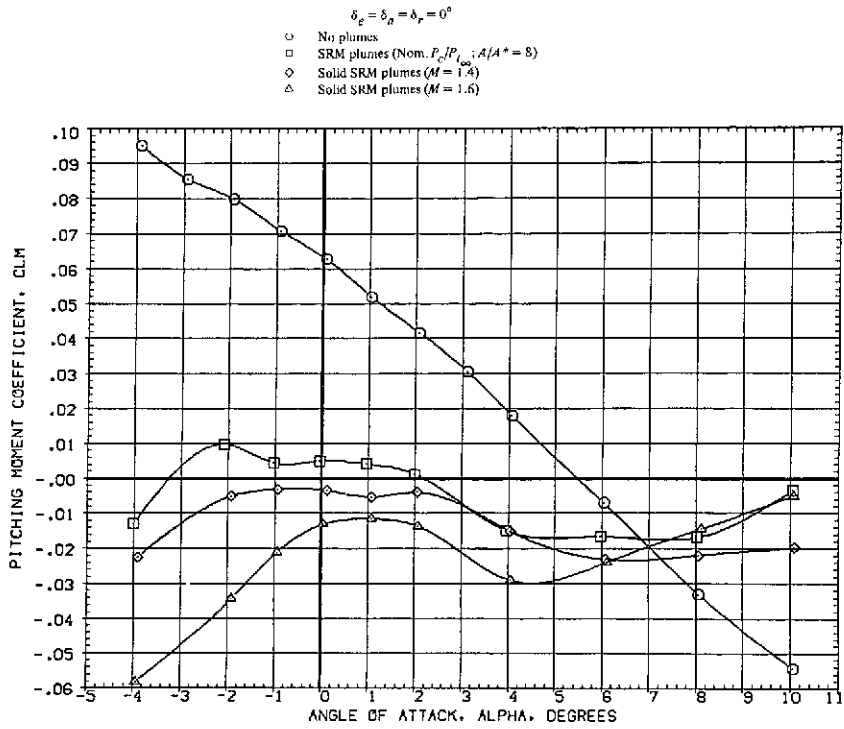
$\delta_e = \delta_a = \delta_r = 0°$

○   No plumes
□   SRM plumes (Nom. P_c/P_{t_∞} ; $A/A^* = 8$)
◇   Solid SRM plumes ($M = 1.4$)
△   Solid SRM plumes ($M = 1.6$)

(c) Pitching moment vs. angle of attack.
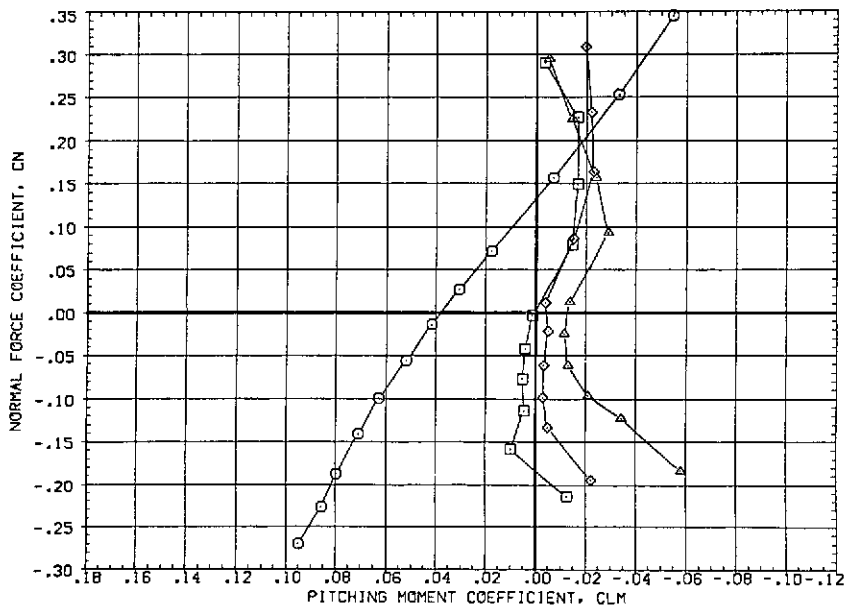
(d) Normal force vs. pitching moment.

Figure 12.– Continued.
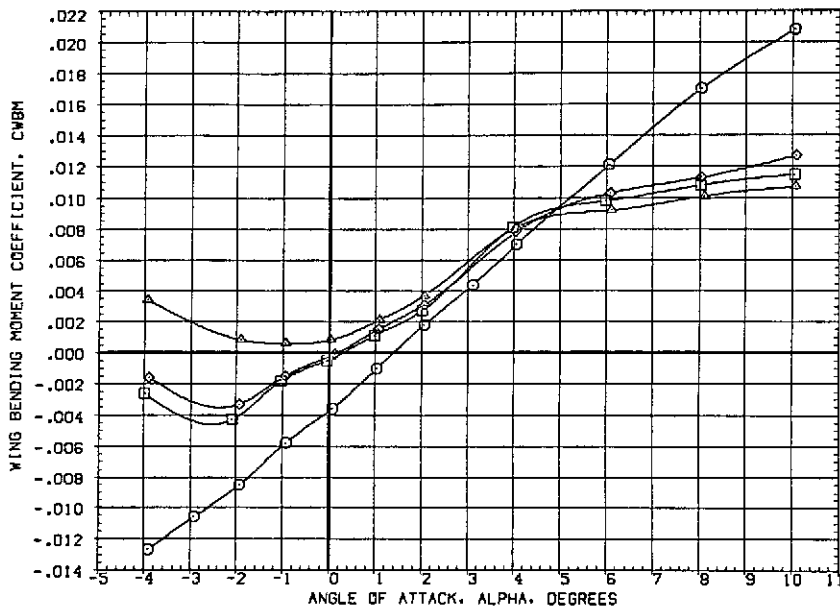
(e) Wing bending moment.
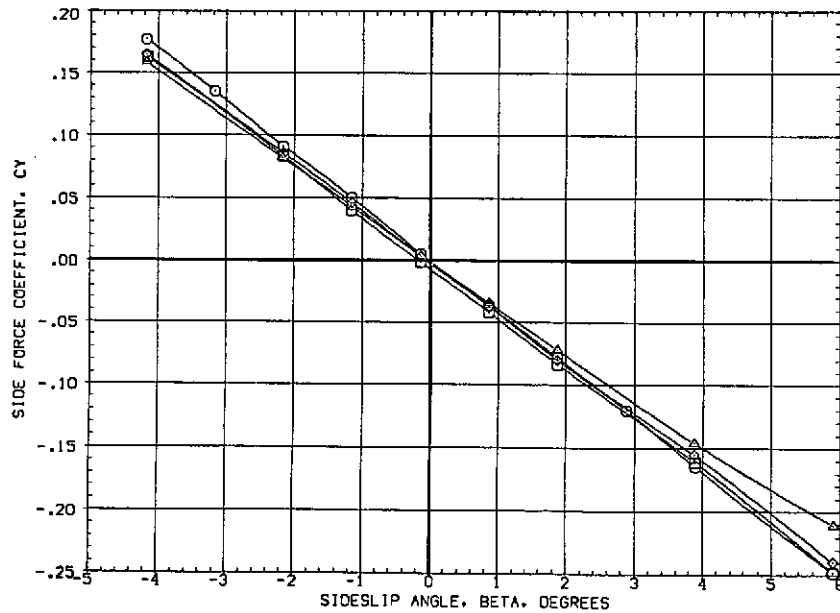
(f) Side force.

Figure 12.– Continued.

64

(g) Yawing moment.

(h) Rolling moment.

Figure 12.— Continued.

65

$\delta_e = \delta_a = \delta_r = 0°$

○	No plumes
□	SRM plumes (Nom. P_t/P_{t_∞} ; $A/A^* = 8$)
◇	Solid SRM plumes ($M = 1.4$)
△	Solid SRM plumes ($M = 1.6$)
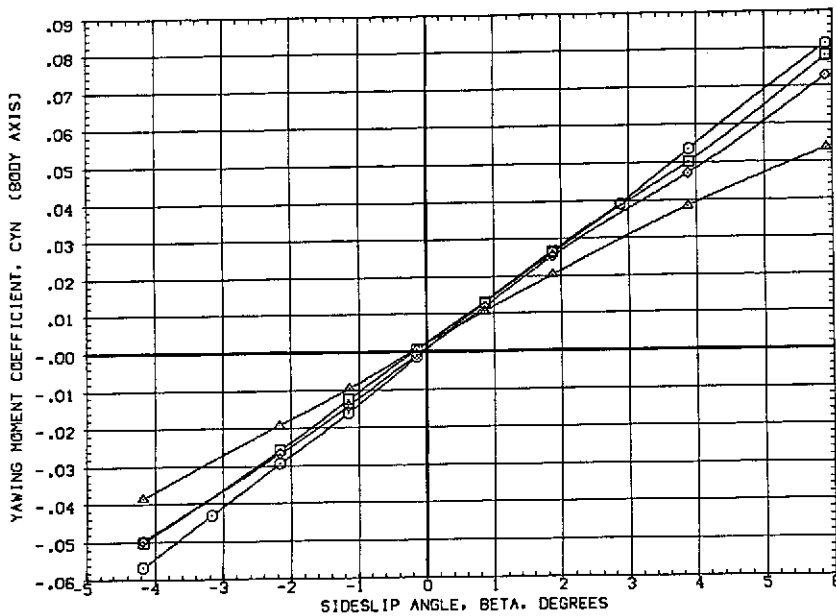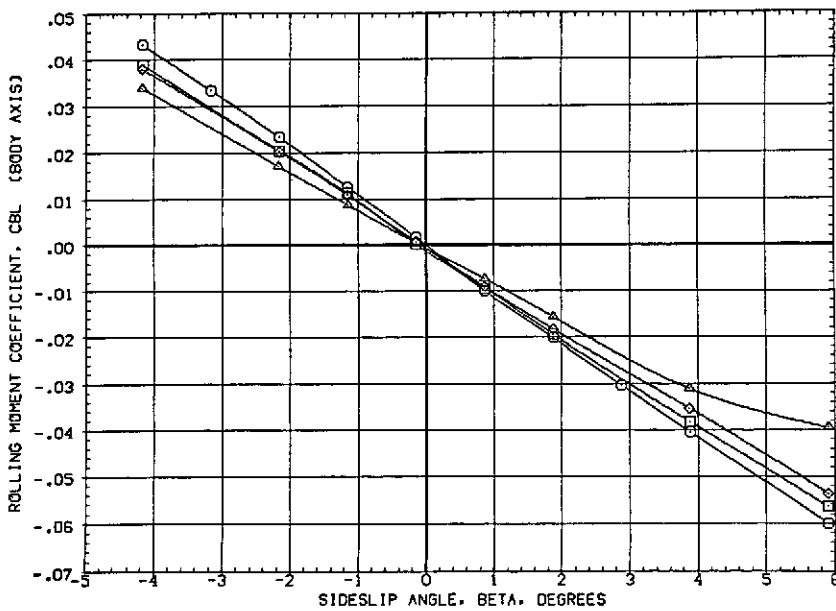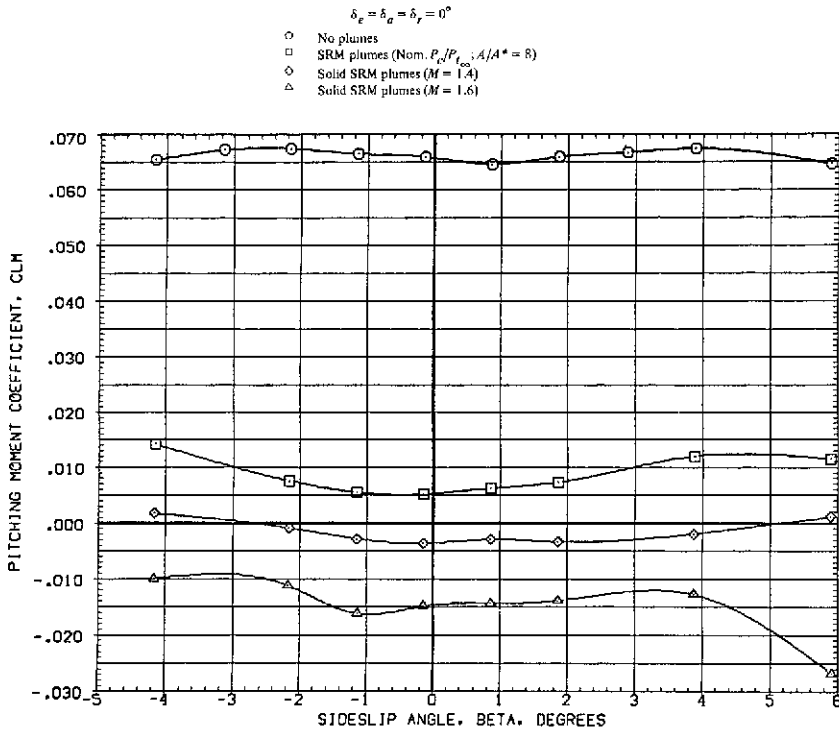
(i) Pitching moment vs. angle of sideslip.
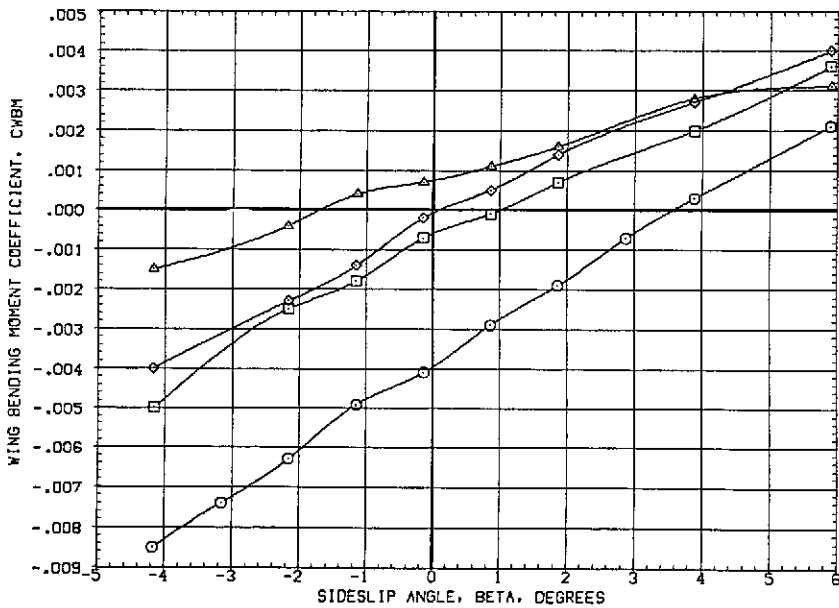
(j) Wing bending moment.

Figure 12.– Concluded.

(a) Normal force vs. angle of attack.

(b) Forebody axial force.

Figure 13.— Comparison of the control effectiveness with gaseous and solid simulated SRM jet plumes at $M = 1.60$.

		$\delta_e{}^\circ$	$\delta_a{}^\circ$	$\delta_r{}^\circ$
○	SRM plumes (P_c/P_{t_∞} Nom.: $A/A^* = 8$)	0	0	0
□	SRM plumes (P_c/P_{t_∞} Nom.: $A/A^* = 8$)	10	0	10
◇	Solid SRM plumes ($M = 1.4$)	0	0	0
△	Solid SRM plumes ($M = 1.4$)	10	0	10

(c) Pitching moment vs. angle of attack.

(d) Normal force vs. pitching moment.

Figure 13.– Continued.

68
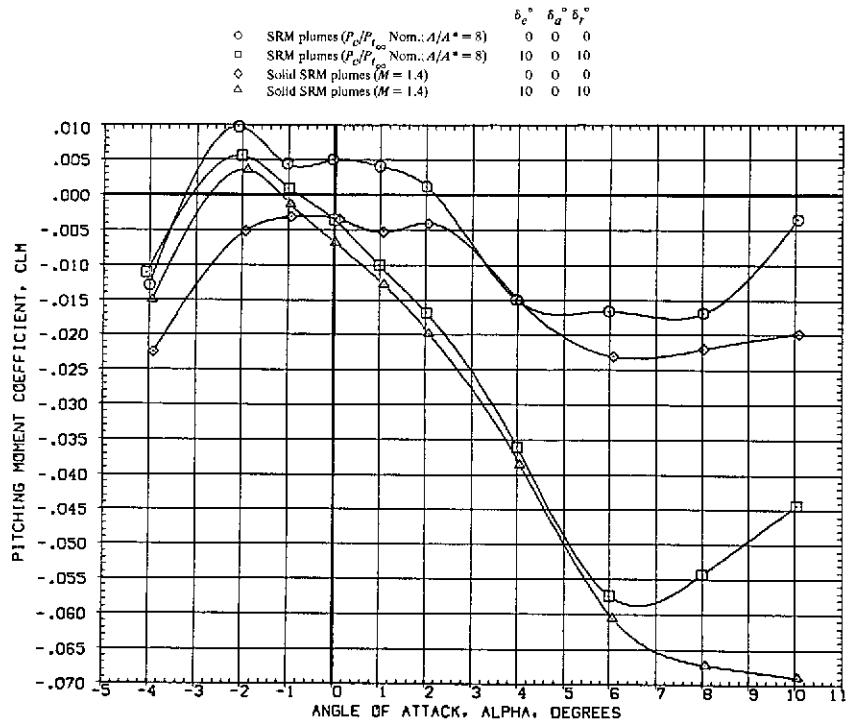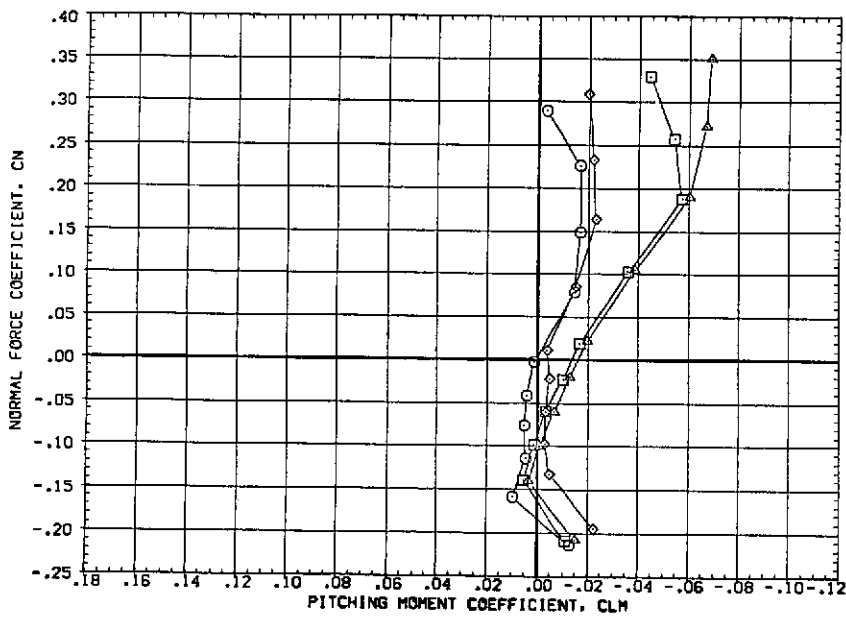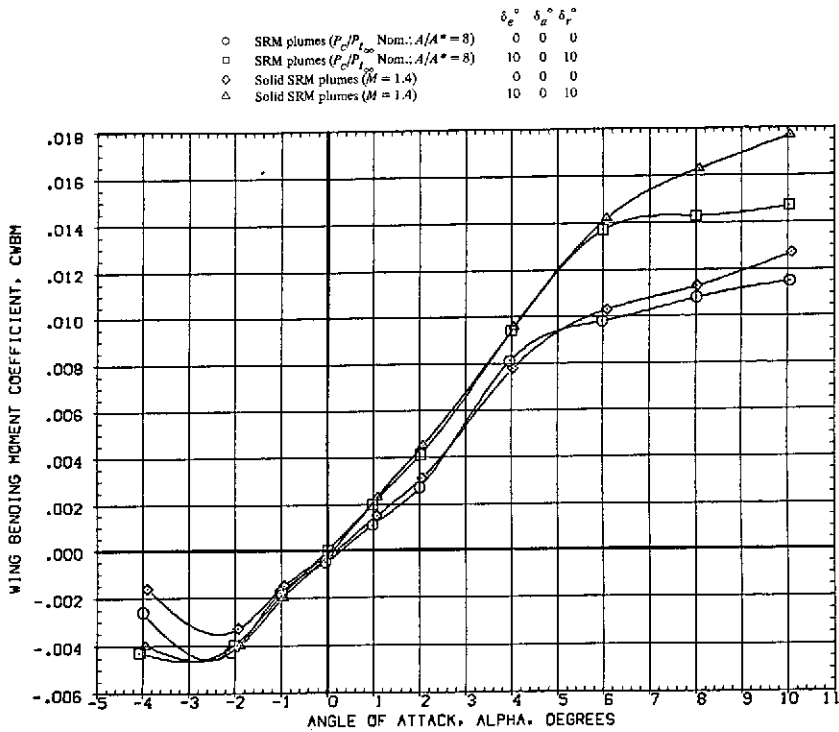
(e) Wing bending moment vs. angle of attack.
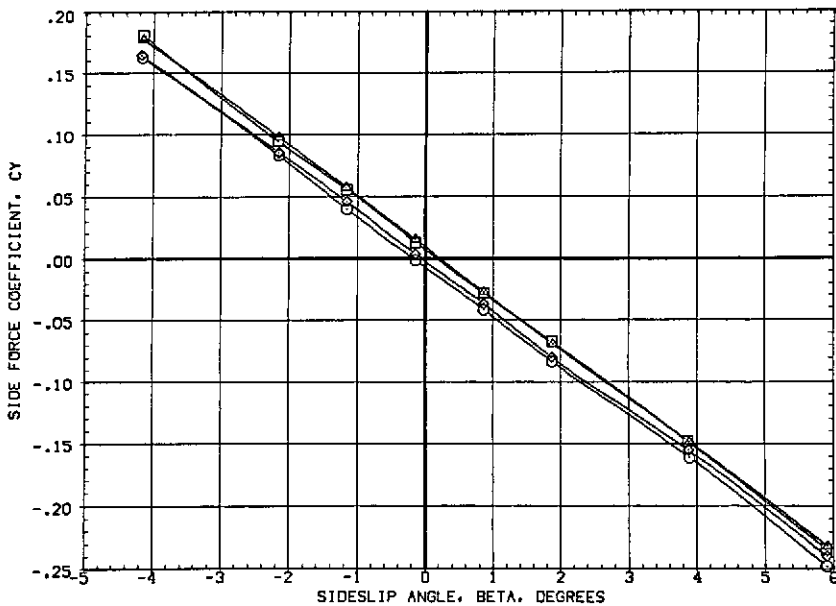
(f) Side force.

Figure 13.– Continued.

		$\delta_e^{\,\circ}$	$\delta_a^{\,\circ}$	$\delta_r^{\,\circ}$
□	SRM plumes $(P_c/P_{t_\infty}$ Nom.; $A/A^* = 8)$	0	0	0
□	SRM plumes $(P_c/P_{t_\infty}$ Nom.; $A/A^* = 8)$	10	0	10
◇	Solid SRM plumes $(M = 1.4)$	0	0	0
△	Solid SRM plumes $(M = 1.4)$	10	0	10

(g) Yawing moment.

(h) Rolling moment.

Figure 13.– Continued.

		$\delta_e^{\,\circ}$	$\delta_a^{\,\circ}$	$\delta_r^{\,\circ}$
○	SRM plumes $(P_c/P_{t_\infty}$ Nom.; $A/A^* = 8)$	0	0	0
□	SRM plumes $(P_c/P_{t_\infty}$ Nom.; $A/A^* = 8)$	10	0	10
◇	Solid SRM plumes $(M = 1.4)$	0	0	0
△	Solid SRM plumes $(M = 1.4)$	10	0	10

(i) Pitching moment vs. angle of sideslip.
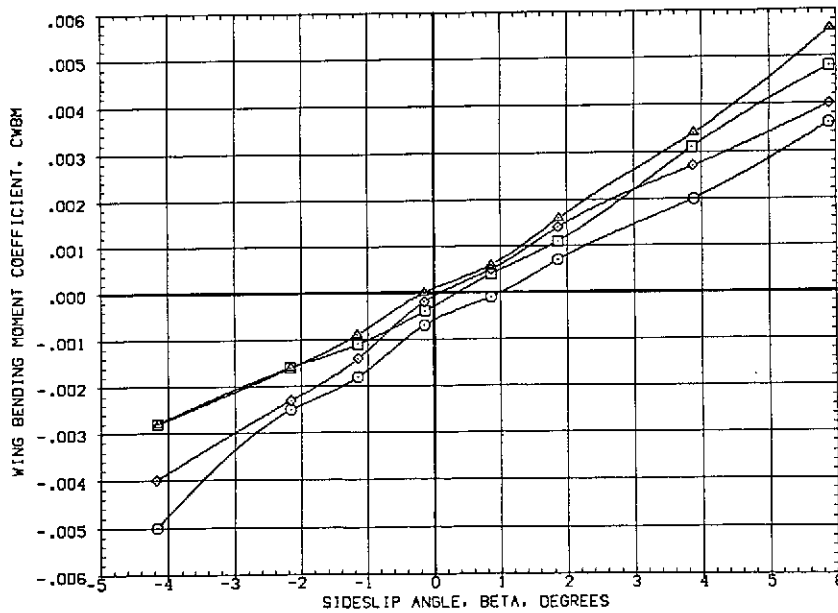
(j) Wing bending moment vs. angle of sideslip.

Figure 13.-- Concluded.

$$\delta_c = \delta_a = \delta_r = 0°$$

o No plumes
□ Orb. and SRM plumes (Nom. P_c/P_{t_∞}; SRM $A/A^* = 8$)
◇ No plumes with OMS
△ Orb. and SRM plumes with OMS (Nom. P_c/P_∞; SRM $A/A^* = 8$)
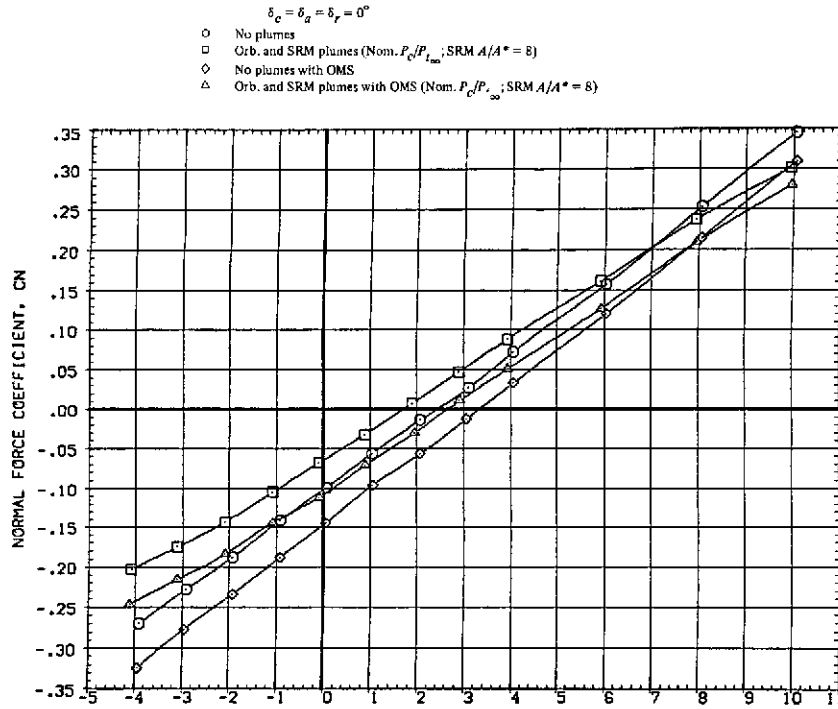
(a) Normal force vs. angle of attack.
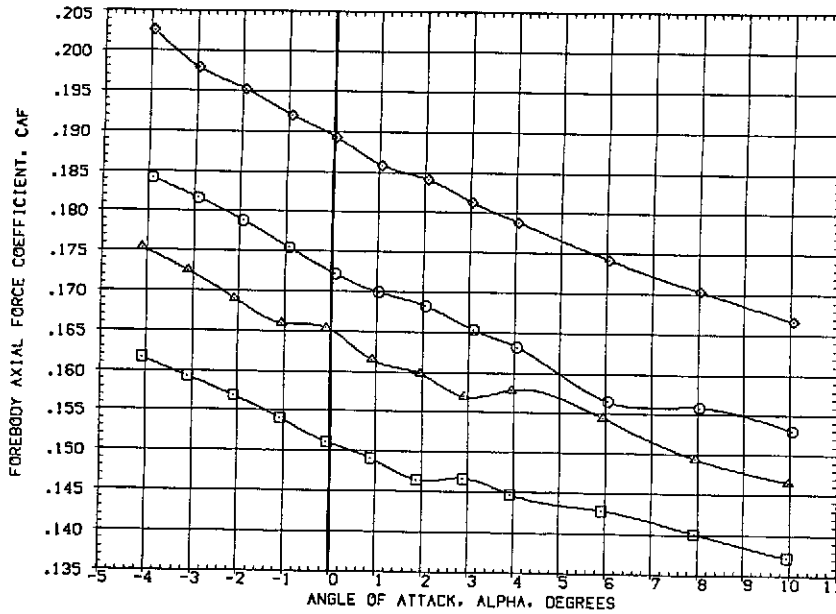
(b) Forebody axial force.

Figure 14.— Plume effects with and without the orbital maneuvering system (OMS) at $M = 1.60$.
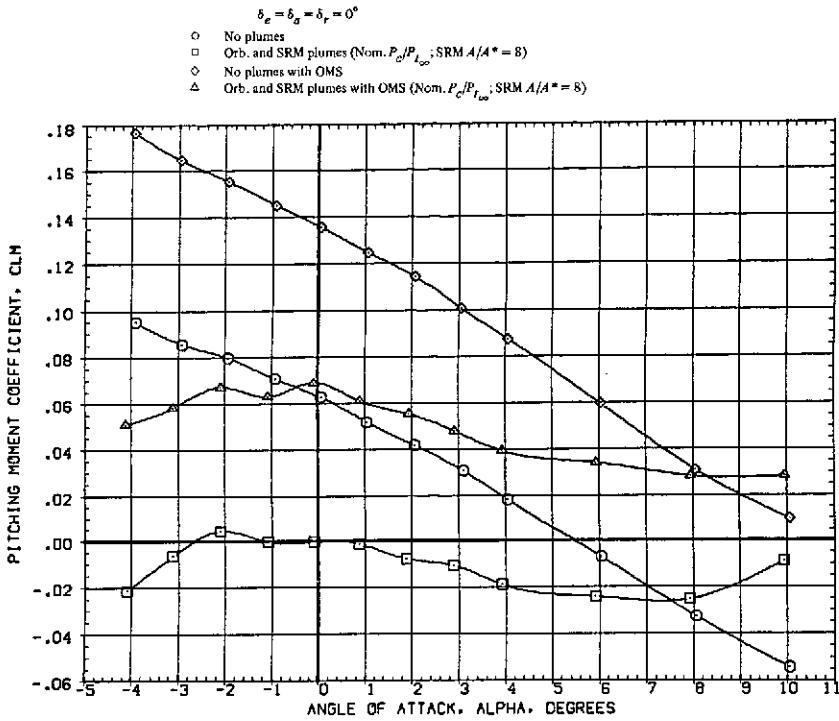
$\delta_e = \delta_a = \delta_r = 0°$

o   No plumes
□   Orb. and SRM plumes (Nom. P_o/P_{t_∞}; SRM $A/A^* = 8$)
◇   No plumes with OMS
△   Orb. and SRM plumes with OMS (Nom. P_o/P_{t_∞}; SRM $A/A^* = 8$)

(c) Pitching moment vs. angle of attack.

(d) Normal force vs. pitching moment.

Figure 14.– Continued.

73
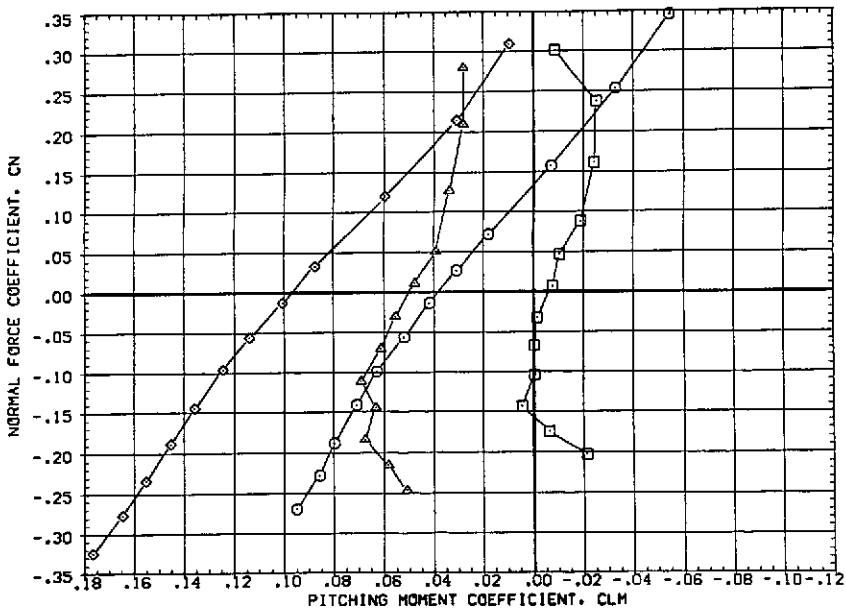
$$\delta_e = \delta_a = \delta_r = 0°$$

○ No plumes
⊔ Orb. and SRM plumes (Nom. P_c/P_{t_∞}; SRM $A/A^* = 8$)
◇ No plumes with OMS
△ Orb. and SRM plumes with OMS (Nom. P_c/P_{t_∞}; SRM $A/A^* = 8$)
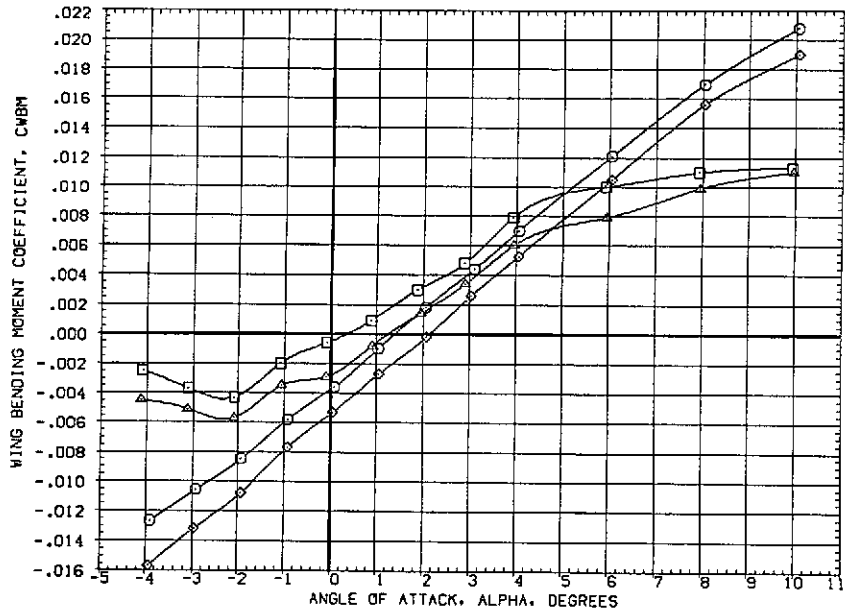
(e) Wing bending moment vs. angle of attack.
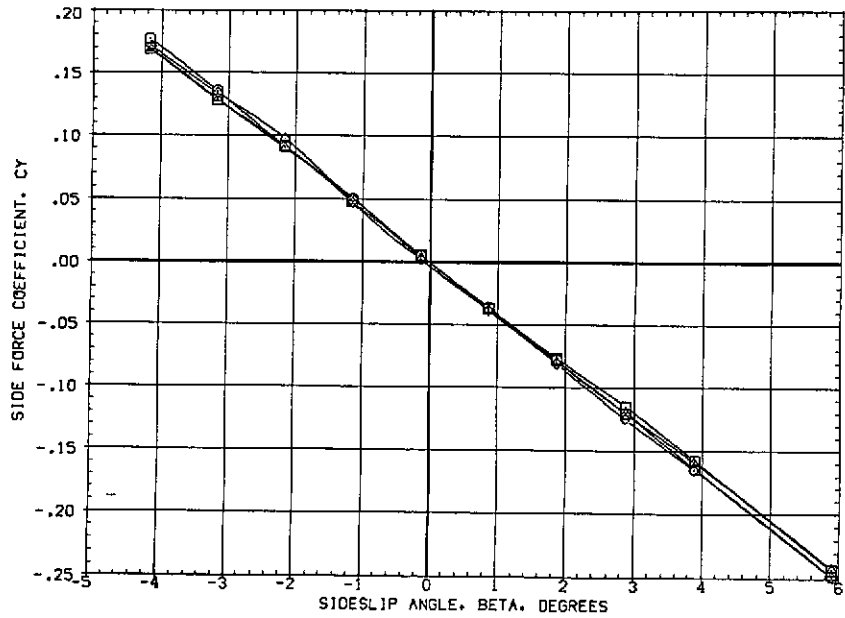
(f) Side force.

Figure 14.– Continued.
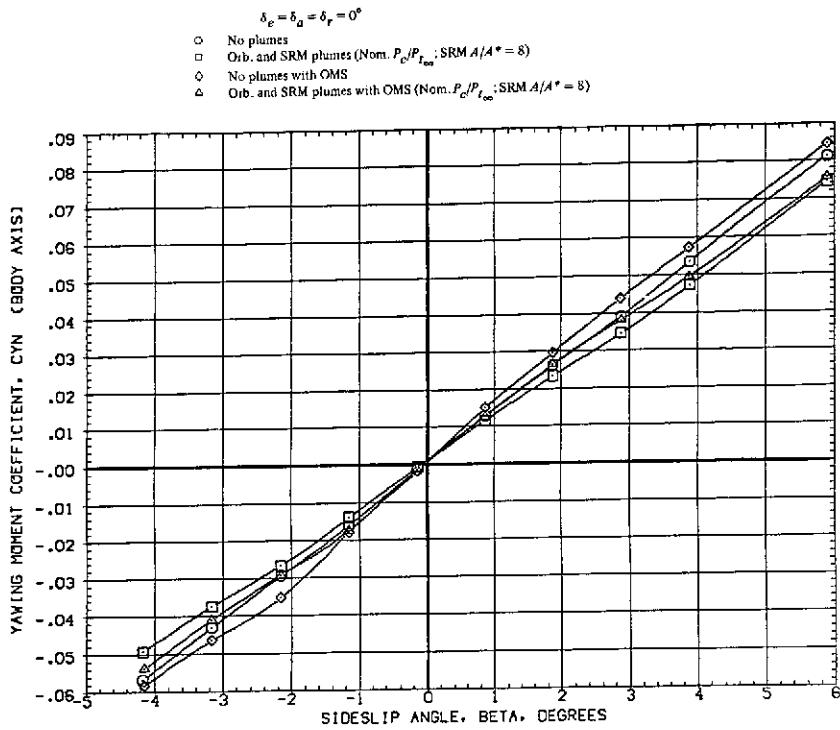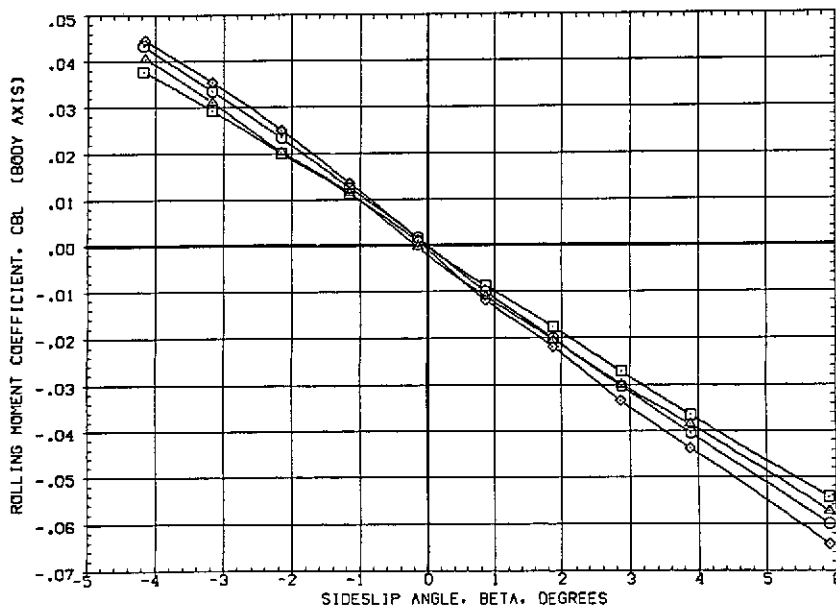
74

(g) Yawing moment.

(h) Rolling moment.

Figure 14.-- Continued.

75

$\delta_e = \delta_a = \delta_r = 0°$

○ No plumes
□ Orb. and SRM plumes (Nom. P_c/P_{t_∞}; SRM $A/A^* = 8$)
◇ No plumes with OMS
△ Orb. and SRM plumes with OMS (Nom. P_c/P_{t_∞}; SRM $A/A^* = 8$)
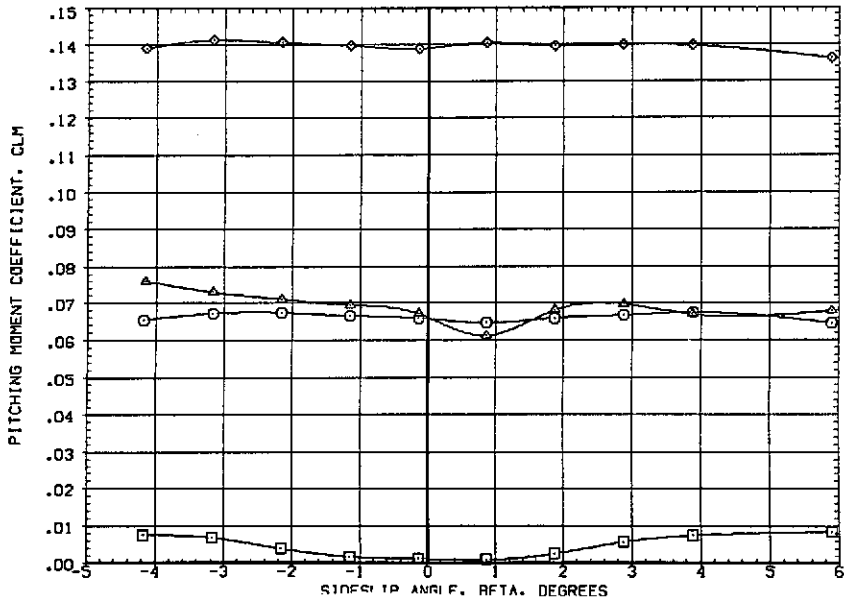
(i) Pitching moment vs. angle of sideslip.
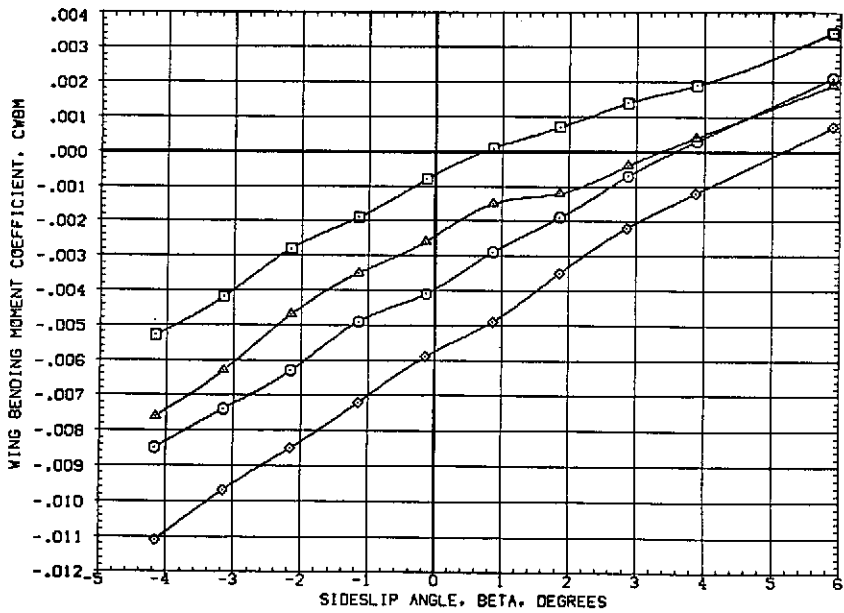
(j) Wing bending moment vs. angle of sideslip.

Figure 14.– Concluded.

76

OMS on; $\delta_e = \delta_a \approx \delta_r = 0°$ $\alpha°$

○   No plumes   −5
□   No plumes   0
◇   No plumes   5
△   Orb. and SRM plumes (Nom. P_c/P_{t_∞})   −5
◁   Orb. and SRM plumes (Nom. P_c/P_{t_∞})   0
▷   Orb. and SRM plumes (Nom. P_c/P_{t_∞})   5
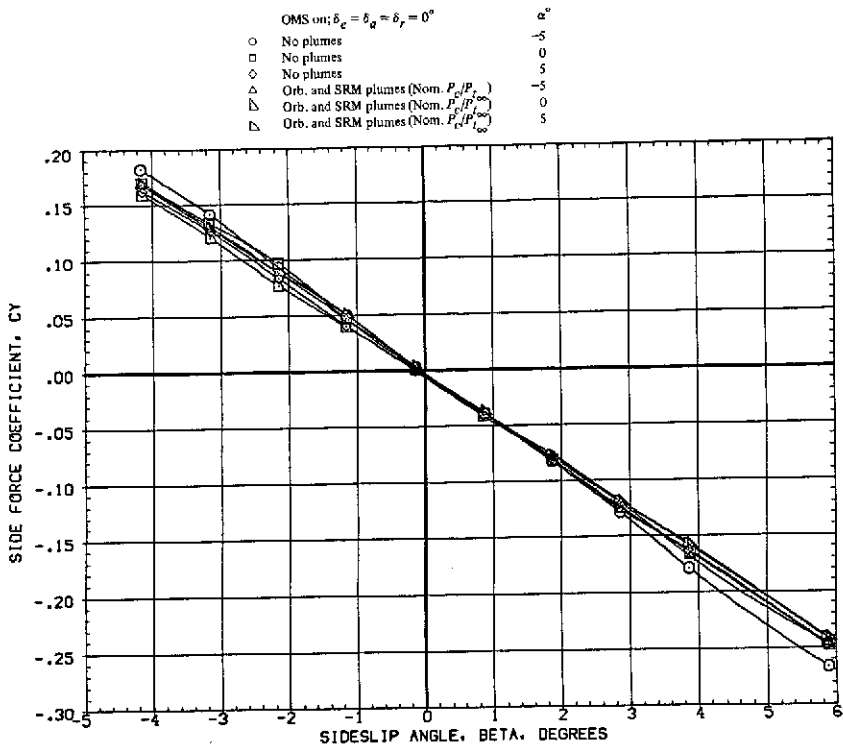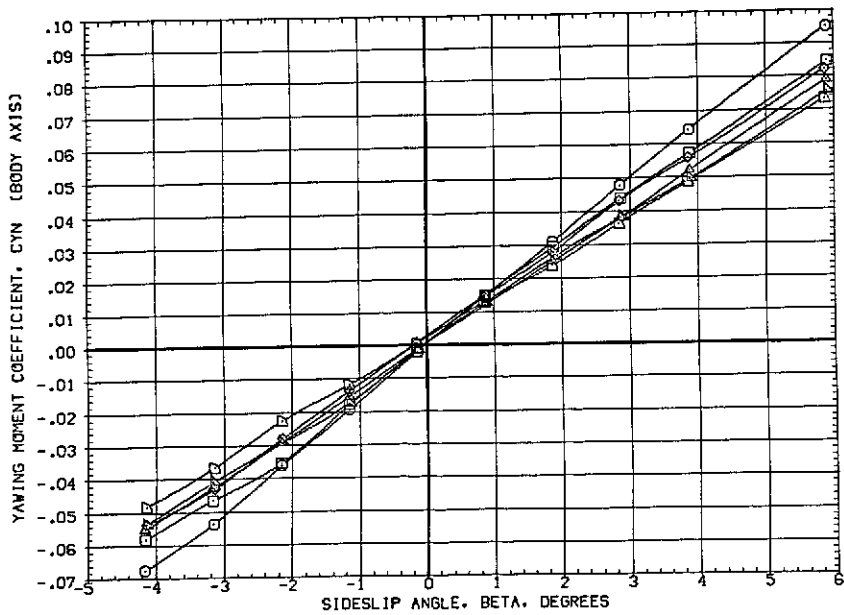
(a) Side force.

(b) Yawing moment.

Figure 15.— Effect of angle of attack and plumes on the lateral characteristics at $M = 1.60$ with OMS.
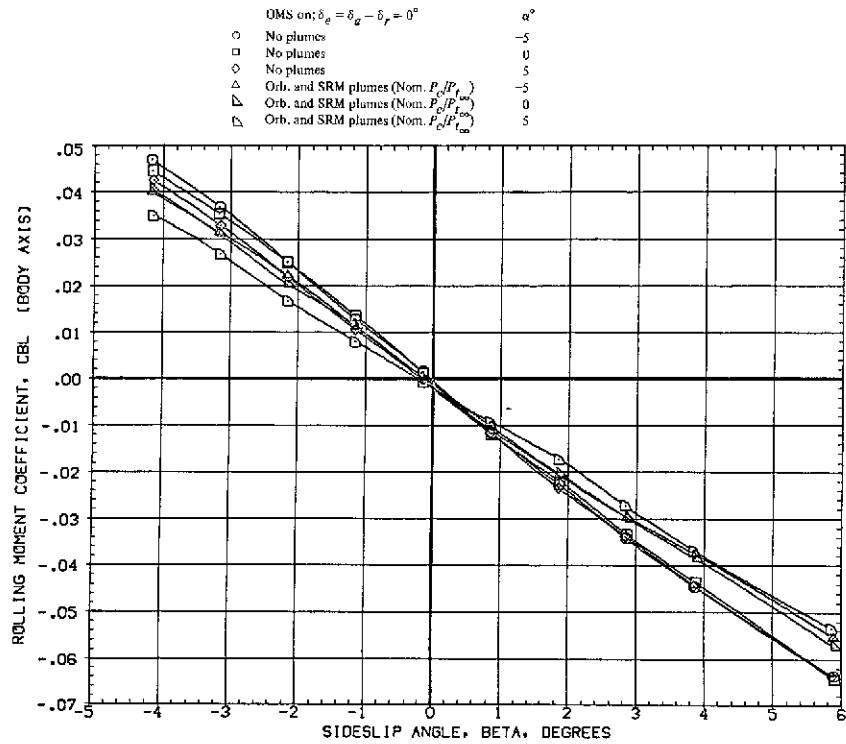
(c) Rolling moment.
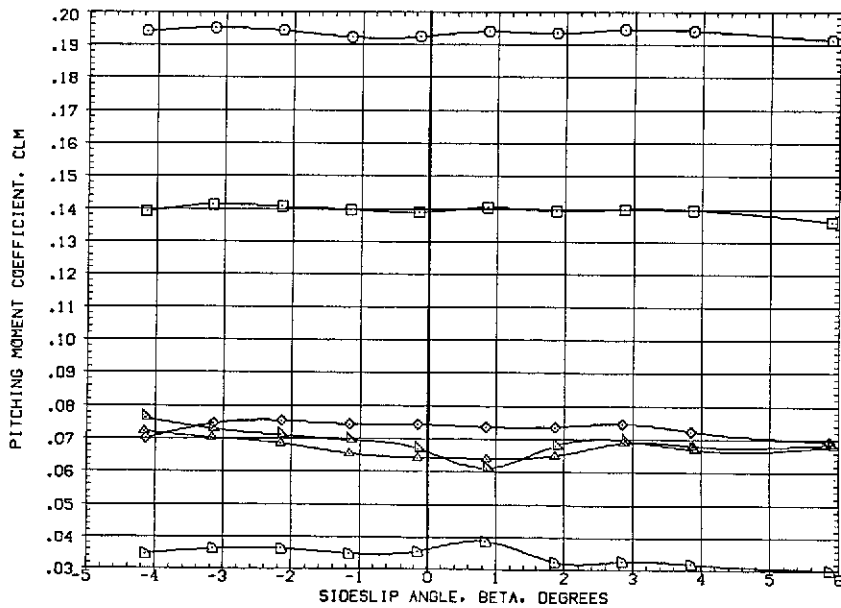
(d) Pitching moment.

Figure 15.– Continued.
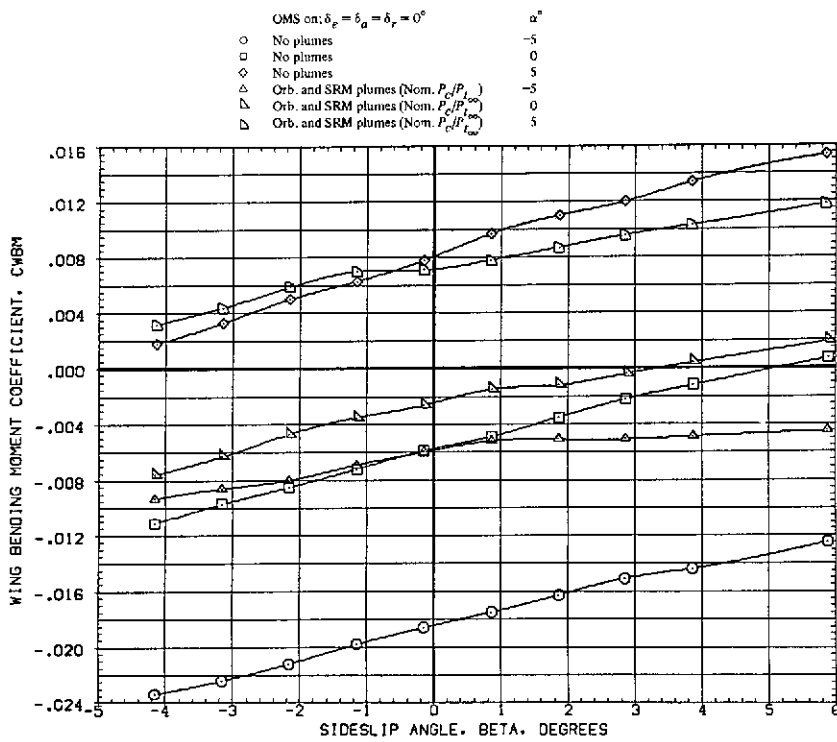
(e) Wing bending moment.

Figure 15.– Concluded.
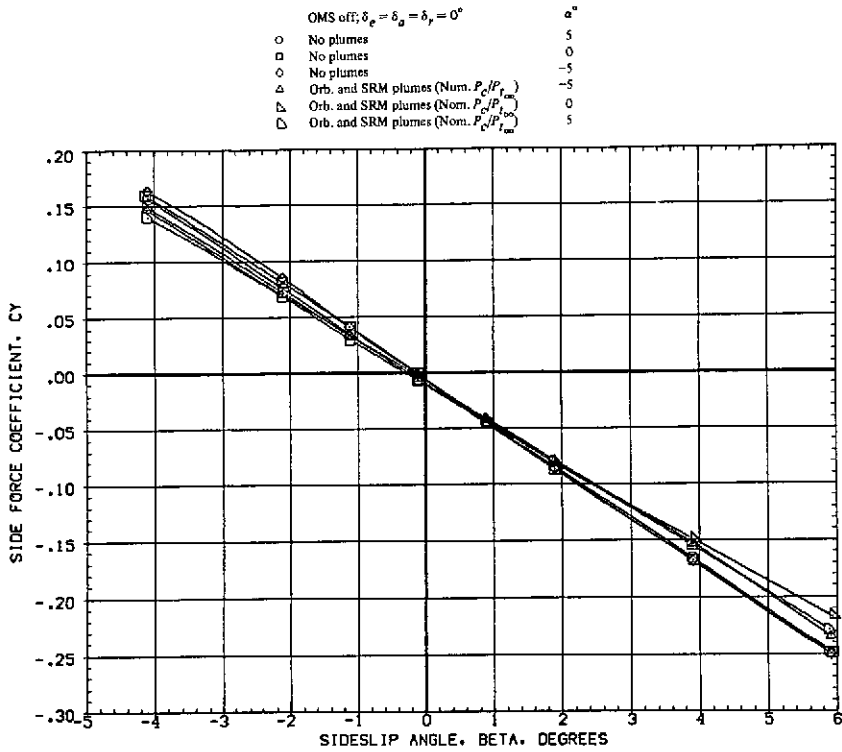
(a) Side force.
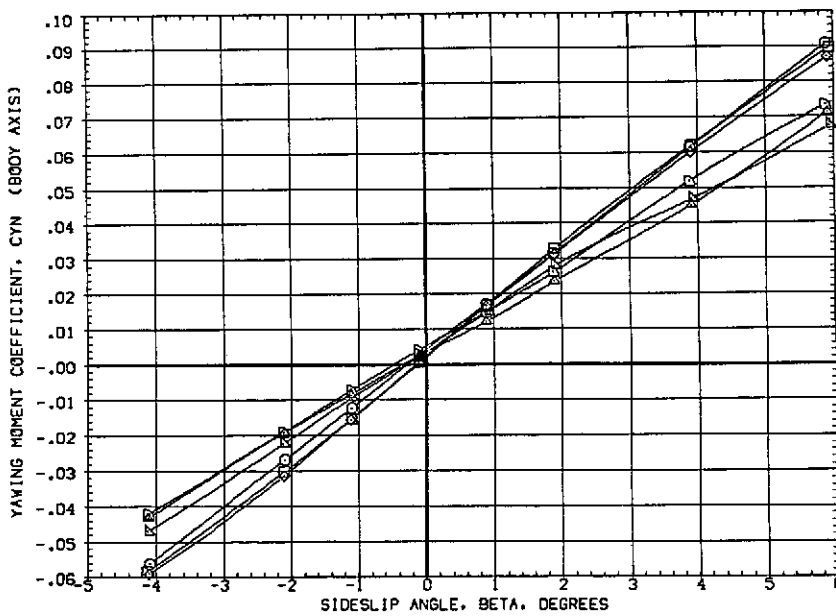
(b) Yawing moment.

Figure 16.— Effect of angle of attack and plumes on the lateral characteristics at $M = 1.98$ without the OMS.

	OMS off; $\delta_e = \delta_a = \delta_r = 0°$	$\alpha°$
○	No plumes	5
□	No plumes	0
◇	No plumes	−5
△	Orb. and SRM plumes (Nom. P_c/P_{t_∞})	−5
◁	Orb. and SRM plumes (Nom. P_c/P_{t_∞})	0
▷	Orb. and SRM plumes (Nom. P_c/P_{t_∞})	5
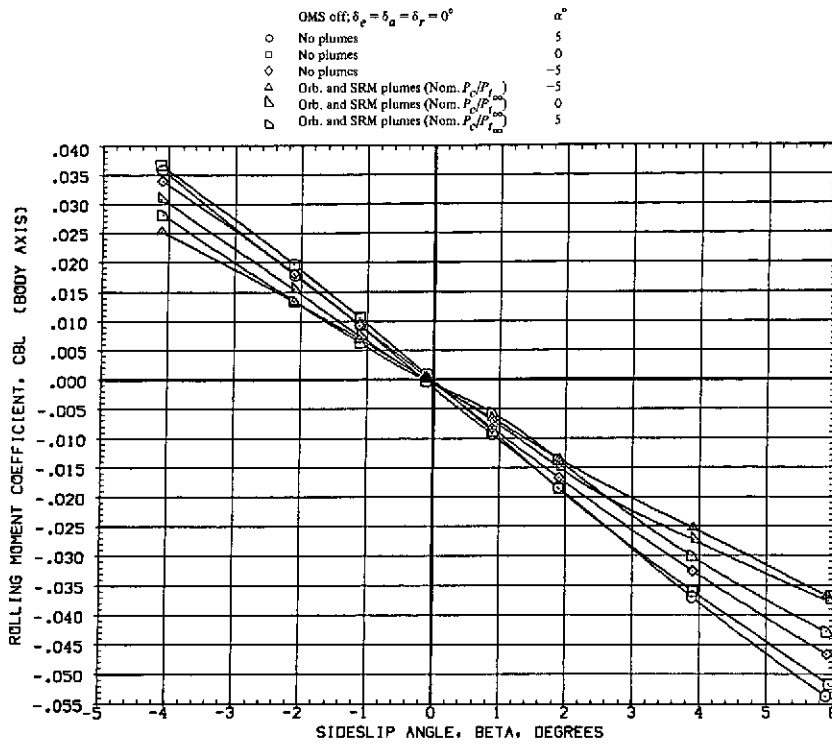
(c) Rolling moment.
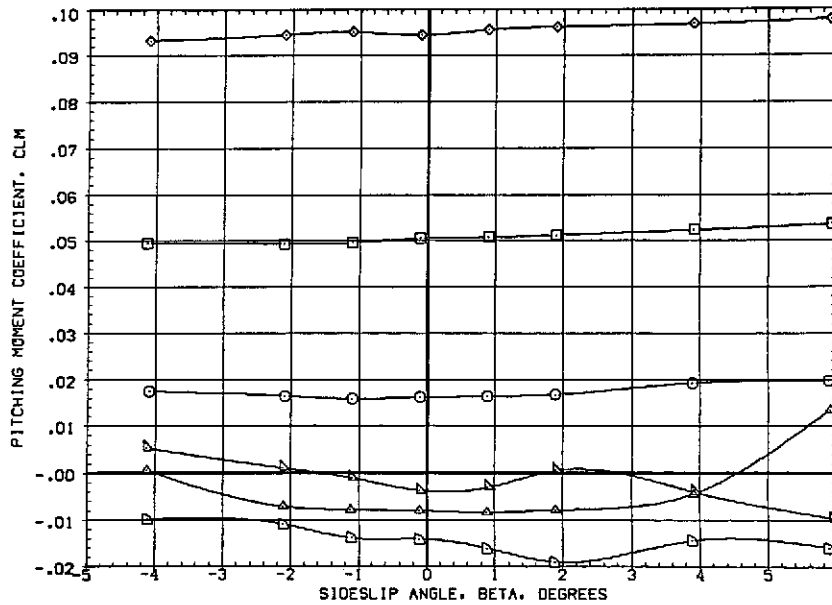
(d) Pitching moment.

Figure 16.— Continued.
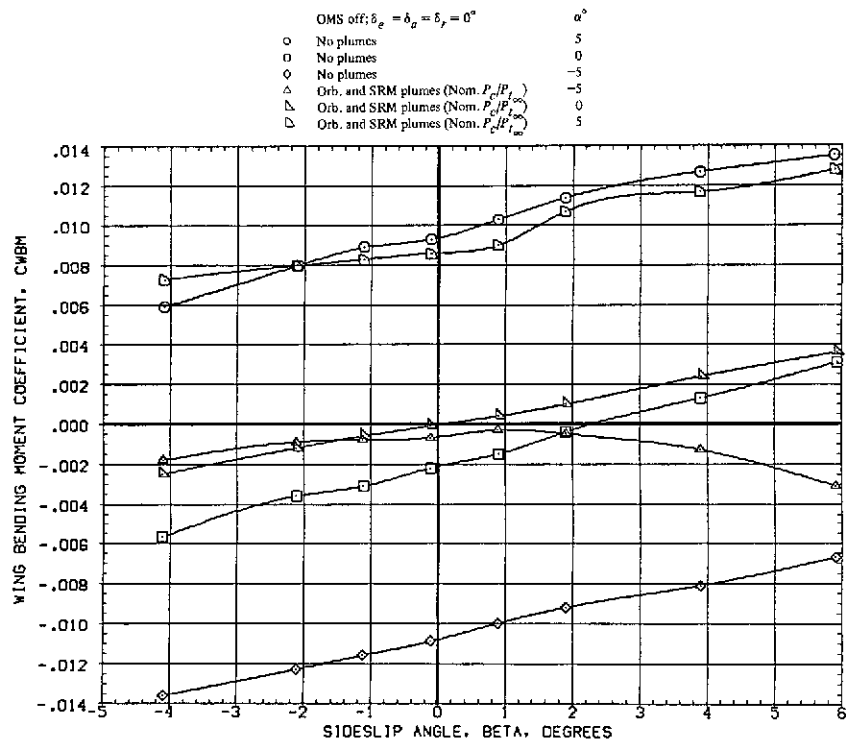
(e) Wing bending moment.

Figure 16.– Concluded.
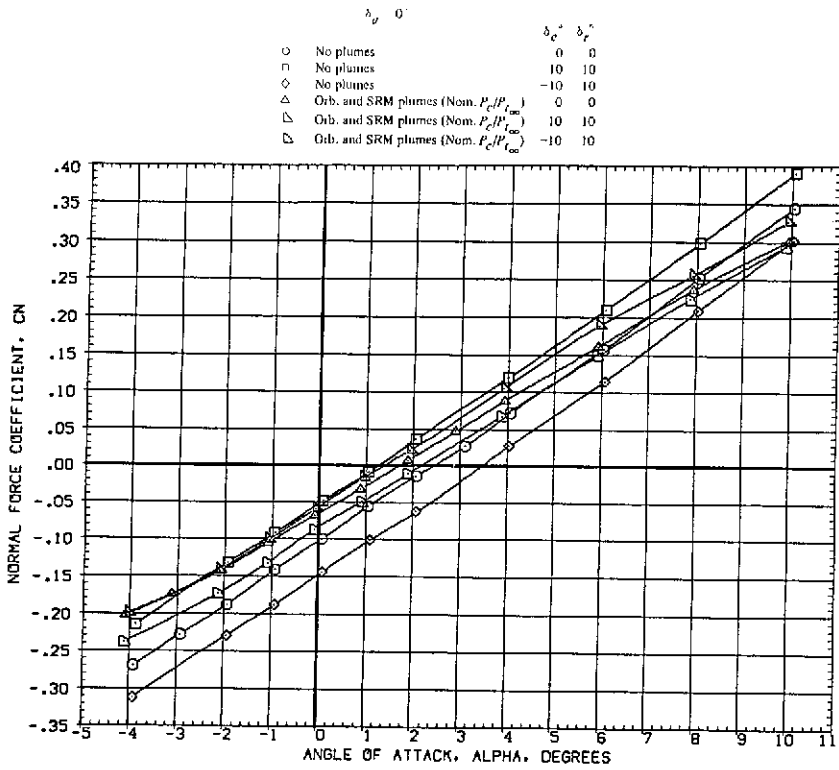
(a) Normal force vs. angle of attack at $M = 1.60$.
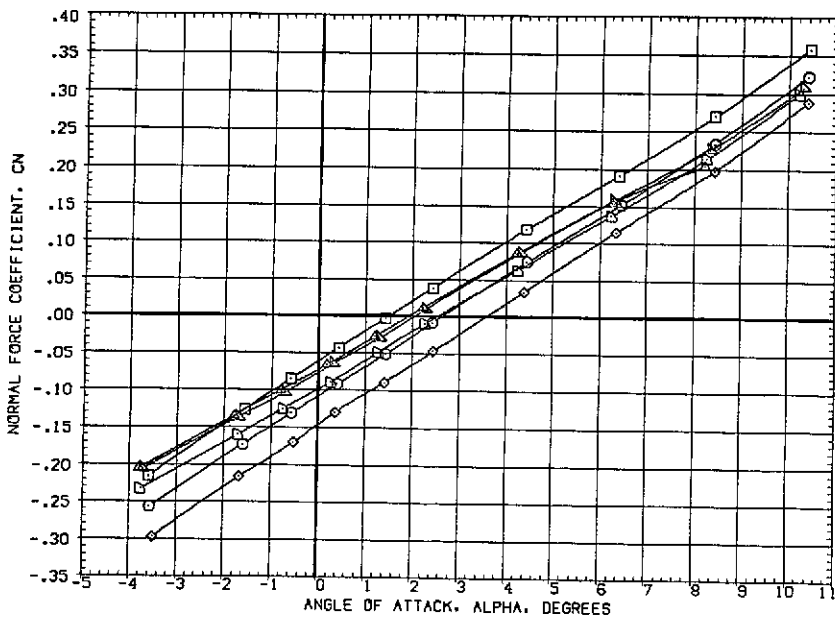
(b) Normal force vs. angle of attack at $M = 1.98$.

Figure 17.— Effect of plumes on the elevon and rudder power at $\beta = 0°$.
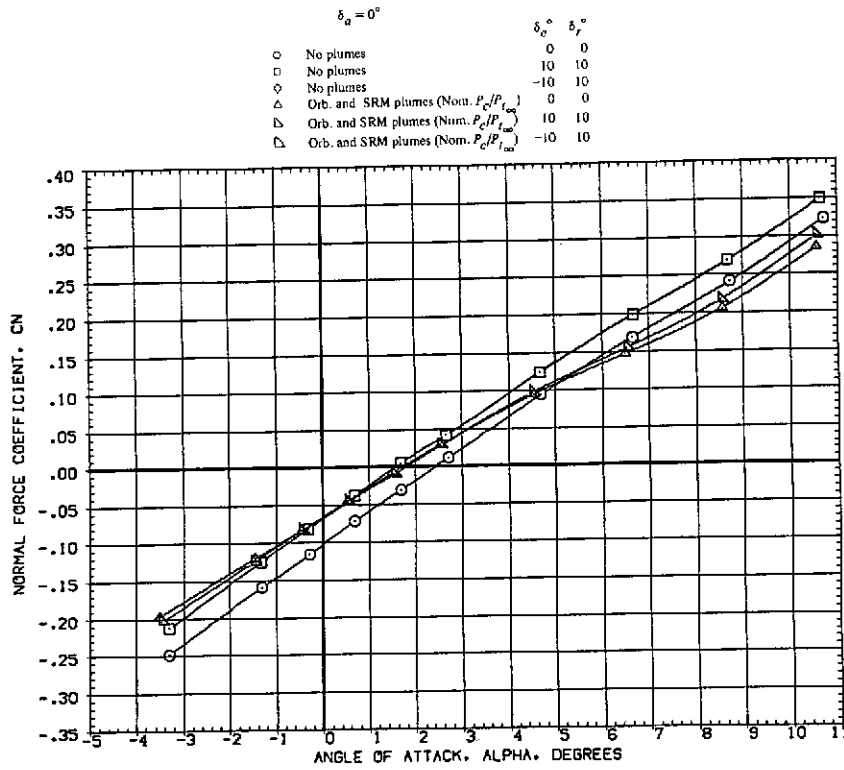
(c) Normal force vs. angle of attack at $M = 2.17$.
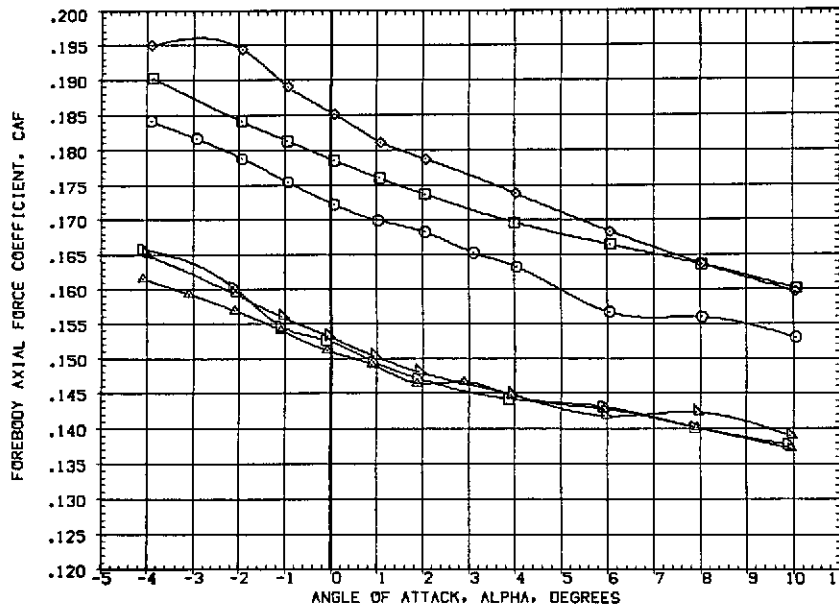
(d) Forebody axial force at $M = 1.60$.

Figure 17.—Continued.

$\delta_a = 0°$

		$\delta_e°$	$\delta_r°$
○	No plumes	0	0
□	No plumes	10	10
◇	No plumes	−10	10
△	Orb. and SRM plumes (Nom. P_c/P_{t_∞})	0	0
◁	Orb. and SRM plumes (Nom. P_c/P_{t_∞})	10	10
▷	Orb. and SRM plumes (Nom. P_c/P_{t_∞})	−10	10

FOREBODY AXIAL FORCE COEFFICIENT, CAF

ANGLE OF ATTACK, ALPHA, DEGREES

(e) Forebody axial force at $M = 1.98$.

FOREBODY AXIAL FORCE COEFFICIENT, CAF

ANGLE OF ATTACK, ALPHA, DEGREES
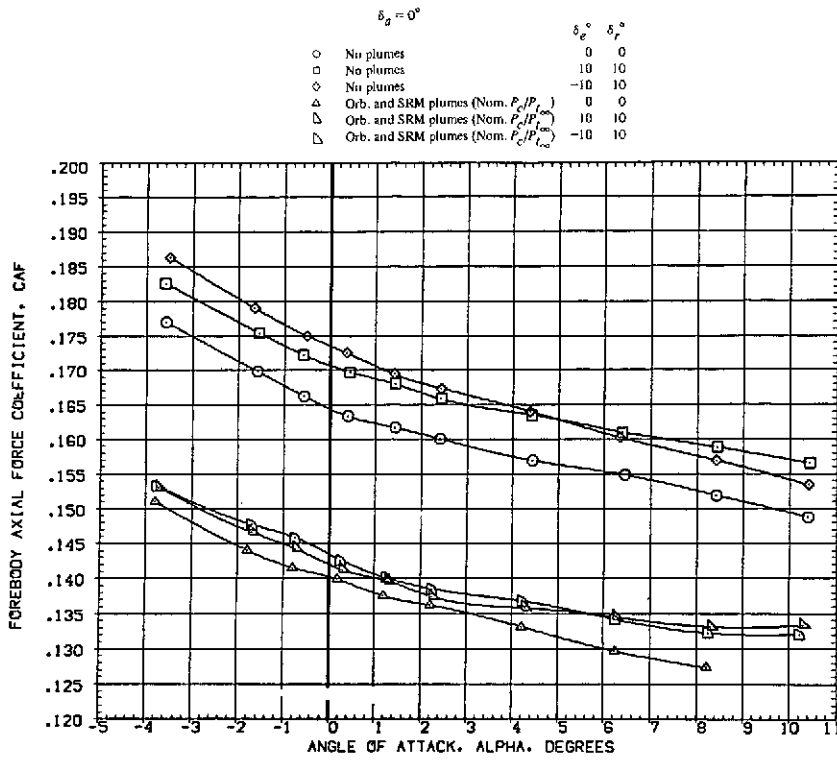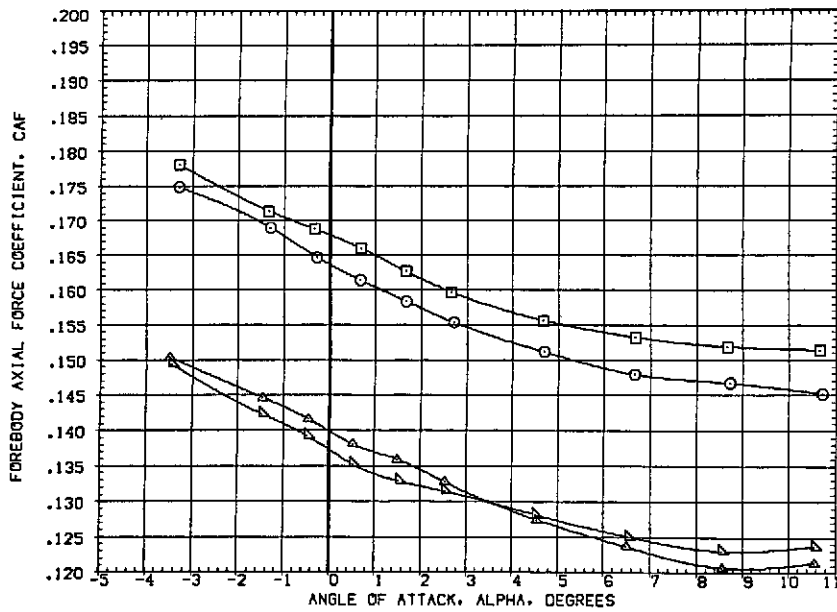
(f) Forebody axial force at $M = 2.17$.

Figure 17.— Continued.

(g) Pitching moment at $M = 1.60$.

(h) Pitching moment at $M = 1.98$.

Figure 17.— Continued.

86

$\delta_a = 0°$

		$\delta_e^°$	$\delta_r^°$
⊡	No plumes	0	0
⊡	No plumes	10	10
○	No plumes	-10	10
◇	Orb. and SRM plumes (Nom. P_c/P_{t_∞})	0	0
△	Orb. and SRM plumes (Nom. P_c/P_{t_∞})	10	10
▷	Orb. and SRM plumes (Nom. P_c/P_{t_∞})	-10	10

(i) Pitching moment at $M = 2.17$.

(j) Normal force vs. pitching moment at $M = 1.60$.

Figure 17.– Continued.

		δ_c^a	δ_r^a
○	No plumes	0	0
□	No plumes	10	10
◇	No plumes	−10	10
△	Orb. and SRM plumes (Nom. P_c/P_{t_∞})	0	0
◩	Orb. and SRM plumes (Nom. P_c/P_{t_∞})	10	10
◪	Orb. and SRM plumes (Nom. P_c/P_{t_∞})	−10	10
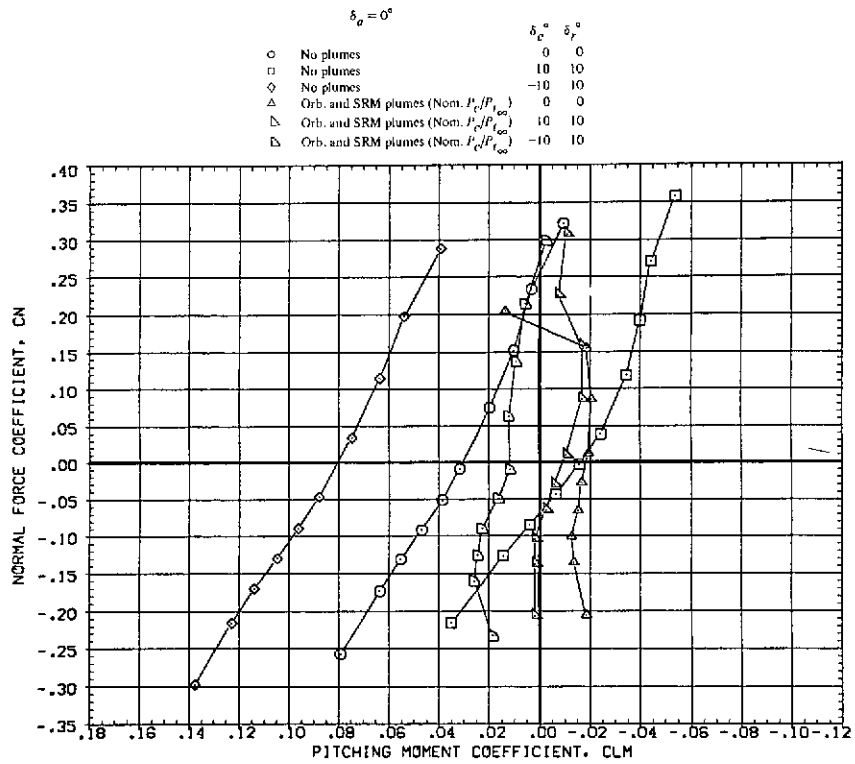
(k) Normal force vs. pitching moment at $M = 1.98$.

(l) Normal force vs. pitching moment at $M = 2.17$.

Figure 17.— Continued.

88

$\delta_a = 0°$

		$\delta_e°$	$\delta_r°$
◯	No plumes	0	0
□	No plumes	10	10
◇	No plumes	-10	10
△	Orb. and SRM plumes (Nom. P_c/P_{t_∞})	0	0
△	Orb. and SRM plumes (Nom. P_c/P_{t_∞})	10	10
△	Orb. and SRM plumes (Nom. P_c/P_{t_∞})	-10	10
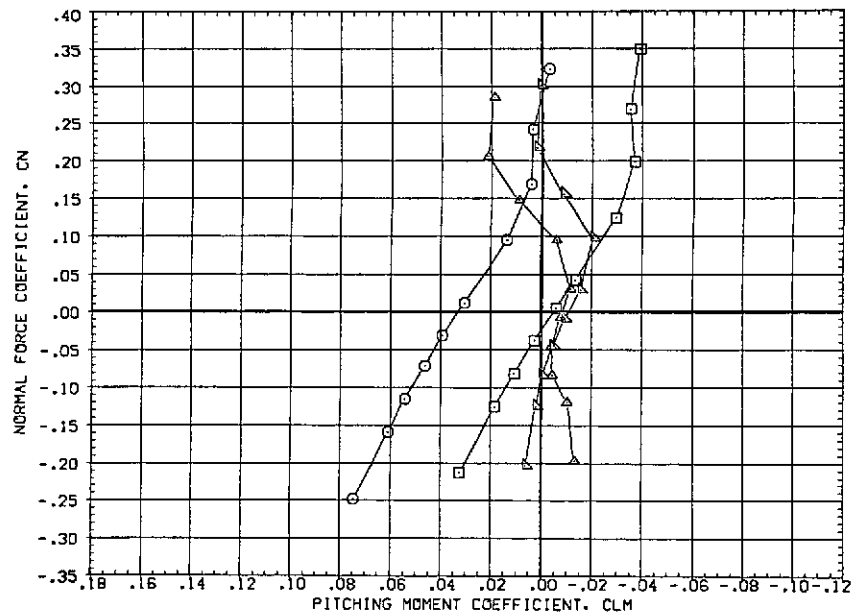
(m) Wing bending moment at $M = 1.60$.

(n) Wing bending moment at $M = 1.98$.

Figure 17.— Continued.
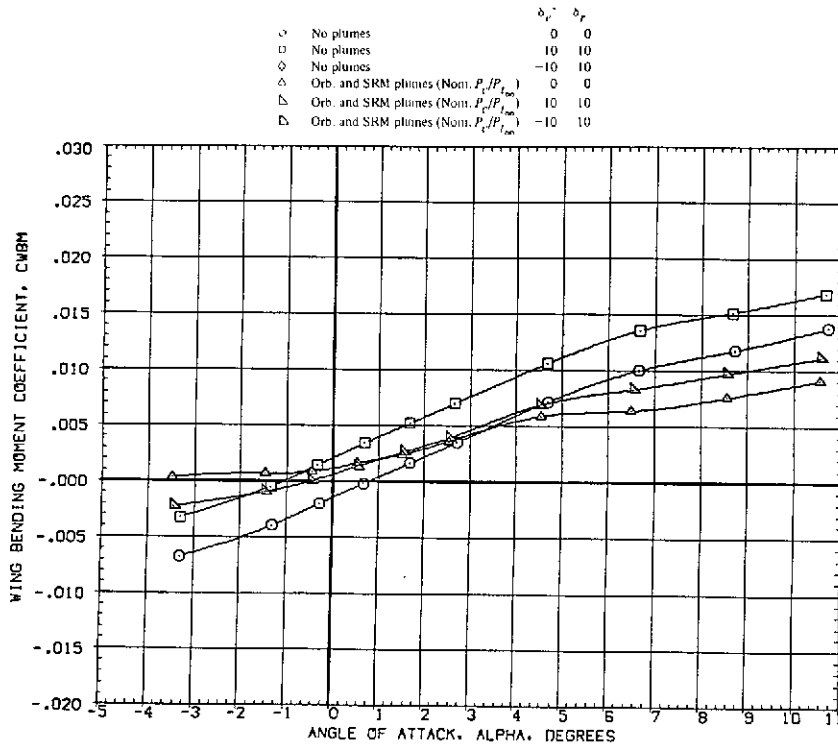
(o) Wing bending moment at $M = 2.17$.
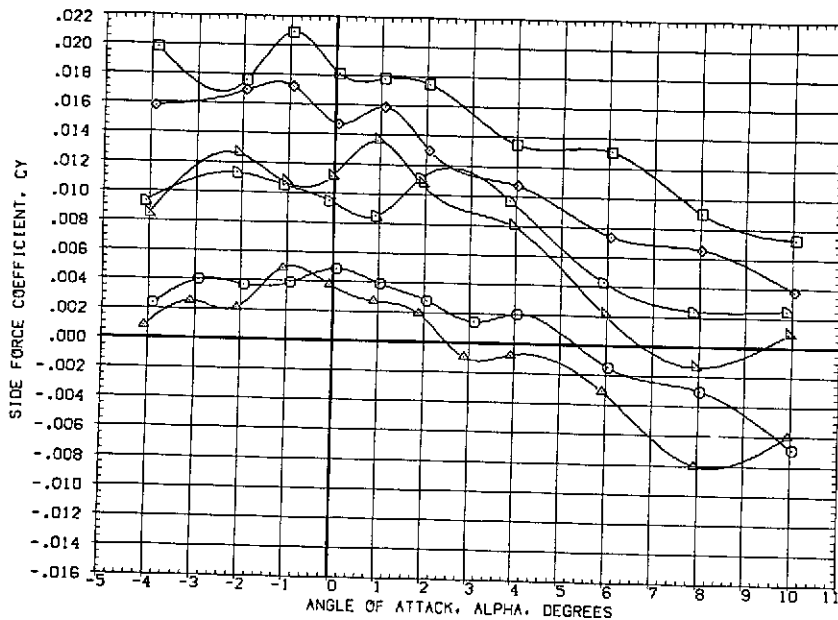
(p) Side force at $M = 1.60$.

Figure 17.-- Continued.

90

$\delta_a = 0$

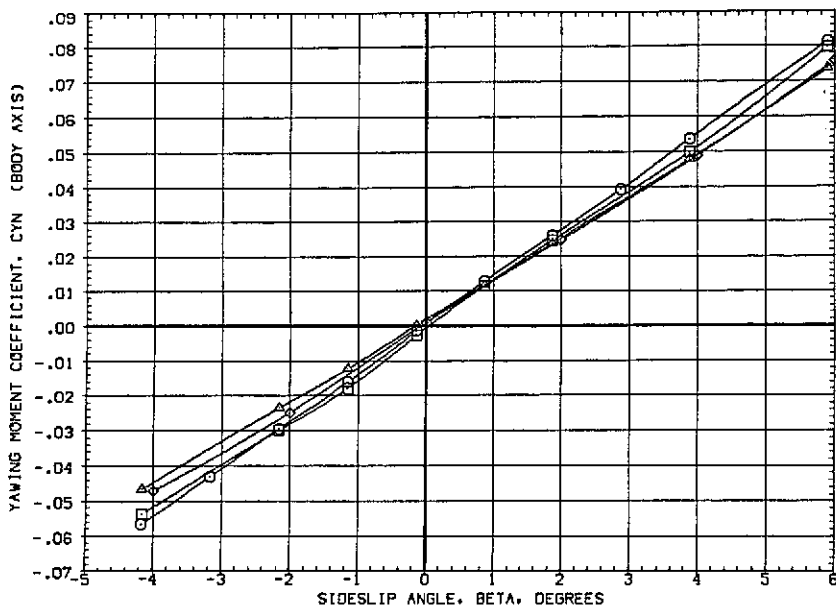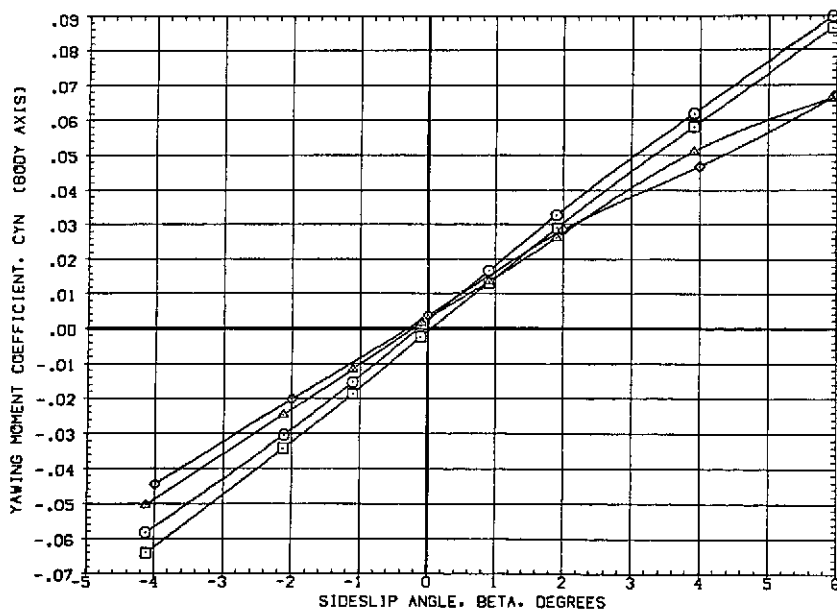|		δ_e	δ_r
	No plumes	0	0
	No plumes	10	10
	No plumes	-10	10
	Orb. and SRM plumes (Nom. P_c P_{t_∞})	0	0
	Orb. and SRM plumes (Nom. P_c/P_{t_∞})	10	10
	Orb. and SRM plumes (Nom. P_c/P_{t_∞})	-10	10
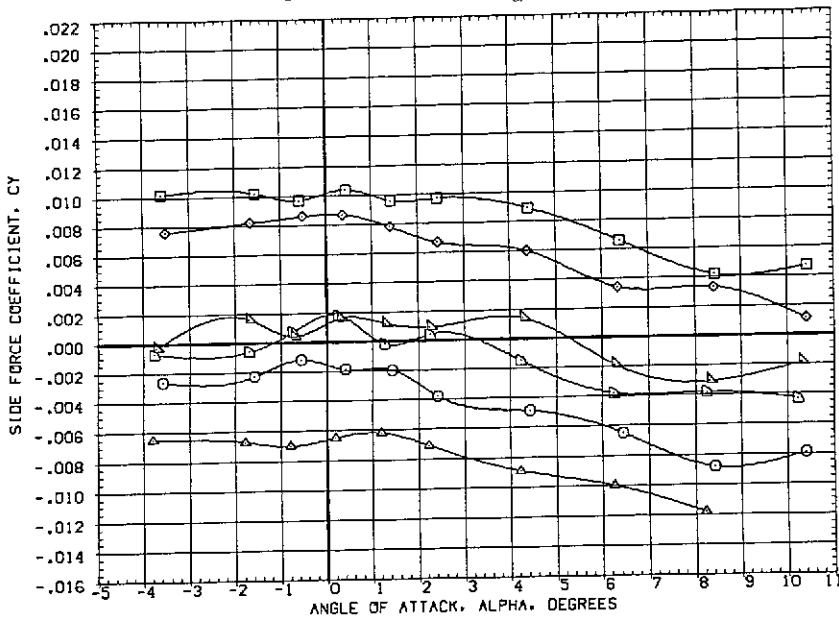
(q) Side force at $M = 1.98$.

(r) Side force at $M = 2.17$.

Figure 17.– Continued.

91

$\delta_a = 0°$

		δ_e°	δ_r°
○	No plumes	0	0
⊔	No plumes	10	10
◇	No plumes	−10	10
∧	Orb. and SRM plumes (Nom. P_c/P_{t_∞})	0	0
◁	Orb. and SRM plumes (Nom. P_c/P_{t_∞})	10	10
◁	Orb. and SRM plumes (Nom. P_c/P_{t_∞})	−10	10

YAWING MOMENT COEFFICIENT, CYN (BODY AXIS)

ANGLE OF ATTACK, ALPHA, DEGREES

(s) Yawing moment at $M = 1.60$.

YAWING MOMENT COEFFICIENT, CYN (BODY AXIS)

ANGLE OF ATTACK, ALPHA, DEGREES

(t) Yawing moment at $M = 1.98$.

Figure 17.— Continued.

$\delta_a = 0°$

		δ_e°	δ_r°
o	No plumes	0	0
u	No plumes	10	10
◊	No plumes	-10	10
△	Orb. and SRM plumes (Nom. P_c/P_{t_∞})	0	0
△	Orb. and SRM plumes (Nom. P_c/P_{t_∞})	10	10
△	Orb. and SRM plumes (Nom. P_c/P_{t_∞})	-10	10

YAWING MOMENT COEFFICIENT, CYN (BODY AXIS)

ANGLE OF ATTACK, ALPHA, DEGREES

(u) Yawing moment at $M = 2.17$.

ROLLING MOMENT COEFFICIENT, CBL (BODY AXIS)

ANGLE OF ATTACK, ALPHA, DEGREES

(v) Rolling moment at $M = 1.60$.

Figure 17.— Continued.

(w) Rolling moment at $M = 1.98$.

(x) Rolling moment at $M = 2.17$.

Figure 17.– Continued.

94

CENTER OF PRESSURE, XCP/L

MACH NUMBER

(y) Center of pressure vs. M.

CABORB

MACH

CABTNK

MACH

CABSRM

MACH

(z) Base forces vs. M.

Figure 17.– Concluded.

$\delta_a = 0°$

		$\delta_e°$	$\delta_r°$
○	No plumes	0	0
□	No plumes	10	10
◇	Orb. and SRM plumes (Nom. P_c/P_{t_∞})	0	0
△	Orb. and SRM plumes (Nom. P_c/P_{t_∞})	10	10
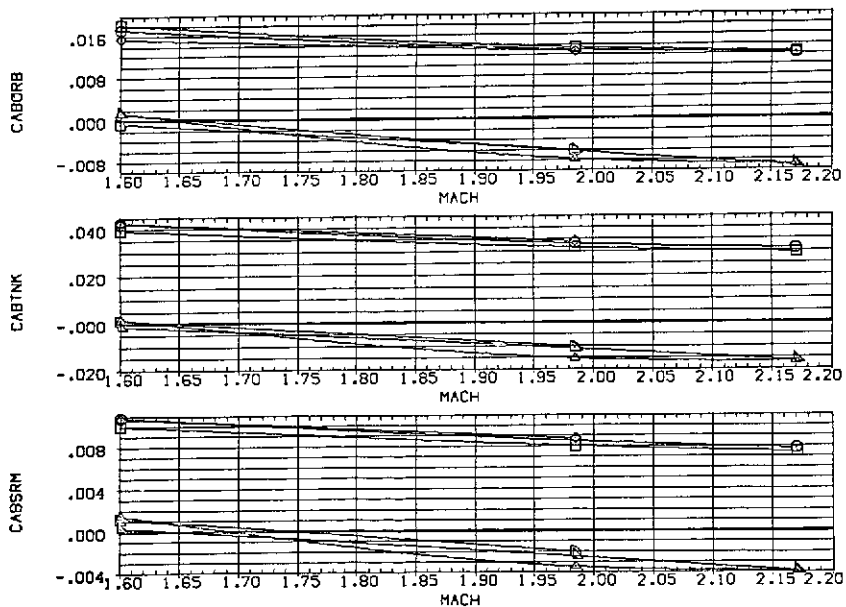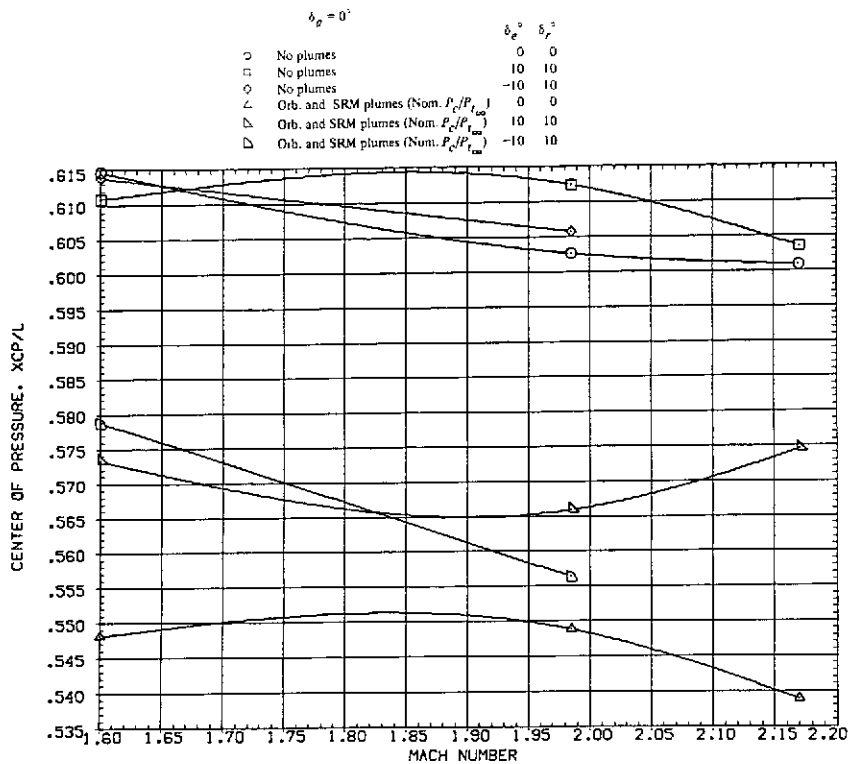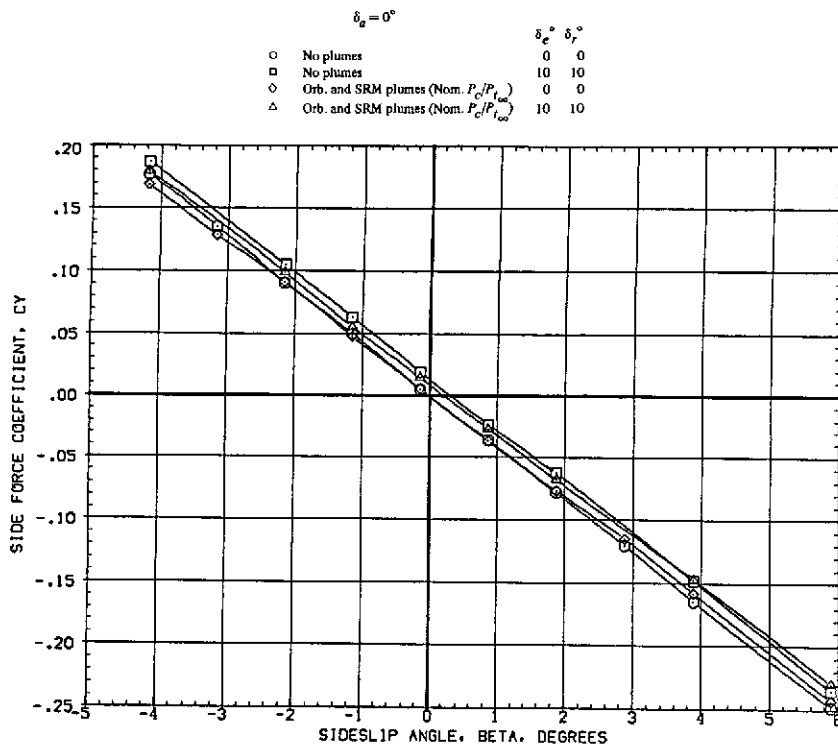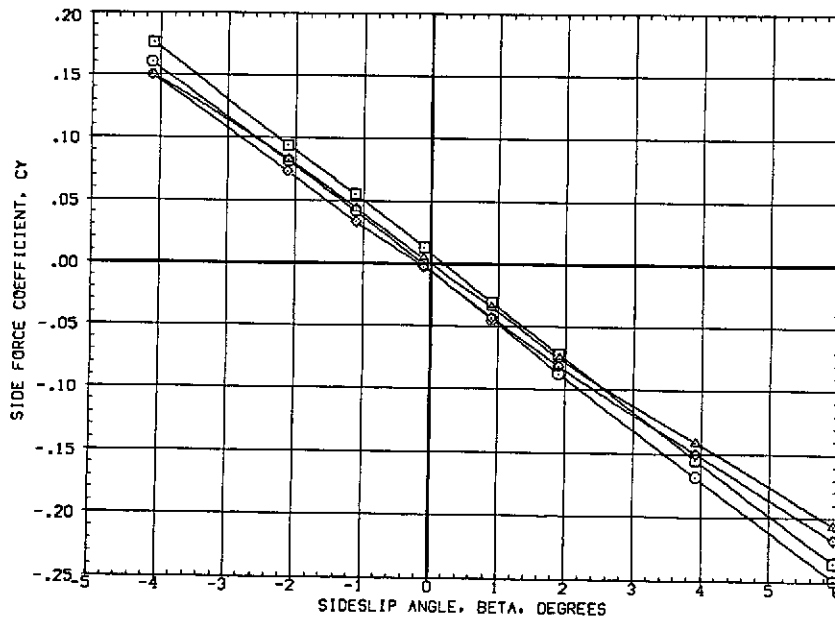
(a) Side force at $M = 1.60$.

(b) Side force at $M = 1.98$.

Figure 18.— Effect of plumes on the elevon and rudder power at $\alpha = 0°$.
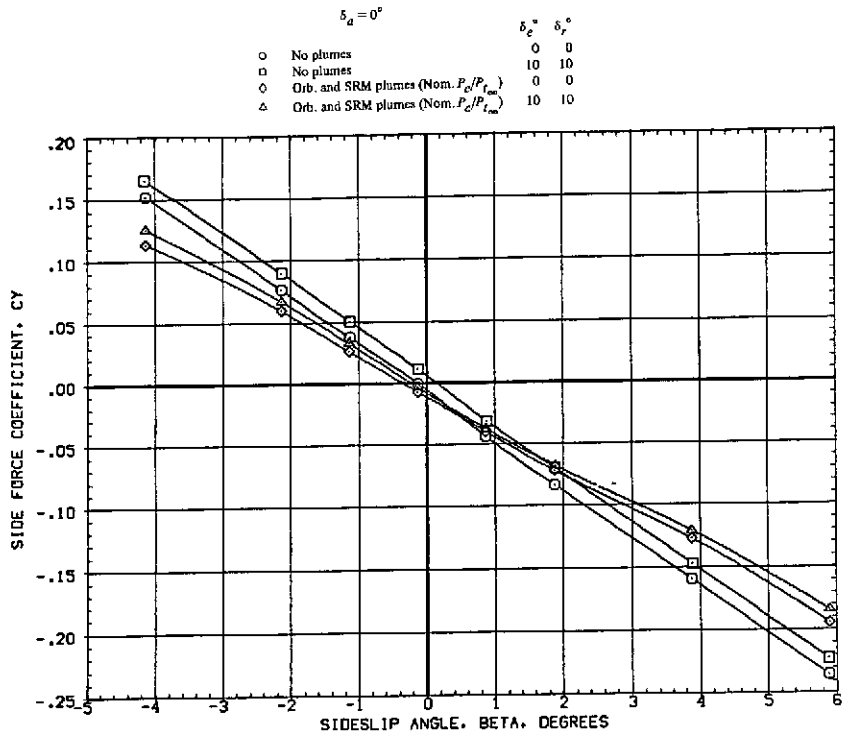
(c) Side force at $M = 2.17$.

(d) Yawing moment at $M = 1.60$.

Figure 18.– Continued.

		$\delta_e°$	$\delta_r°$
○	No plumes	0	0
□	No plumes	10	10
◇	Orb. and SRM plumes (Nom. P_c/P_{t_∞})	0	0
△	Orb. and SRM plumes (Nom. P_c/P_{t_∞})	10	10
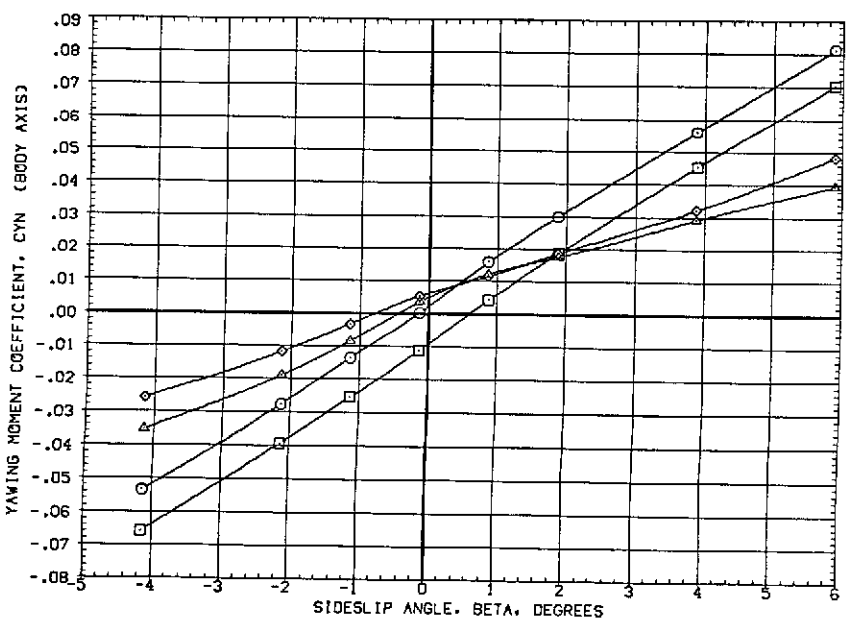
YAWING MOMENT COEFFICIENT, CYN (BODY AXIS)

SIDESLIP ANGLE, BETA, DEGREES

(e) Yawing moment at $M = 1.98$.

YAWING MOMENT COEFFICIENT, CYN (BODY AXIS)

SIDESLIP ANGLE, BETA, DEGREES

(f) Yawing moment at $M = 2.17$.

Figure 18.— Continued.

(g) Rolling moment at $M = 1.60$.

(h) Rolling moment at $M = 1.98$.

Figure 18.– Continued.
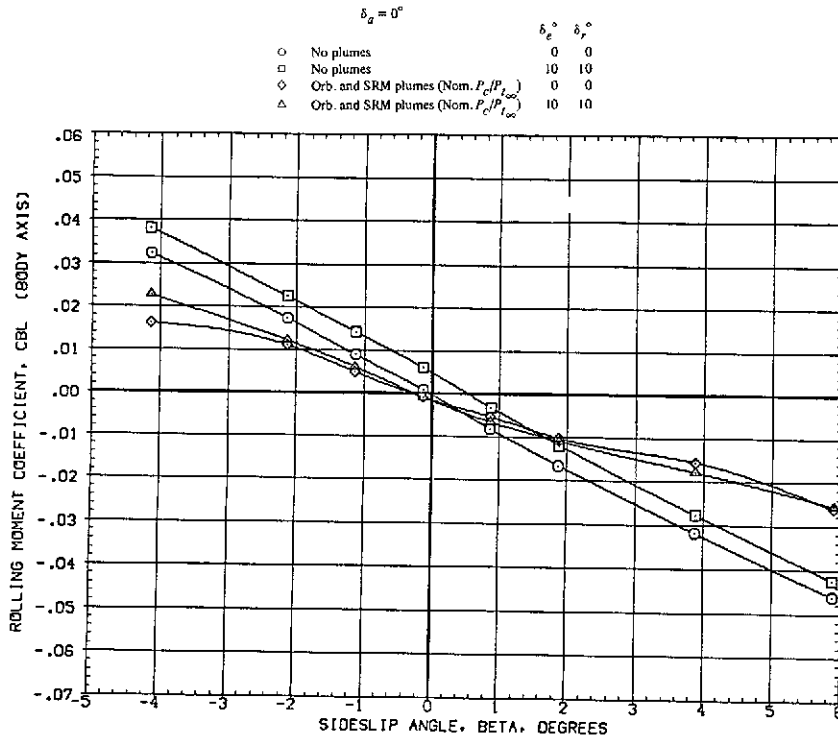
(i) Rolling moment at $M = 2.17$.

(j) Pitching moment at $M = 1.60$.

Figure 18.– Continued.
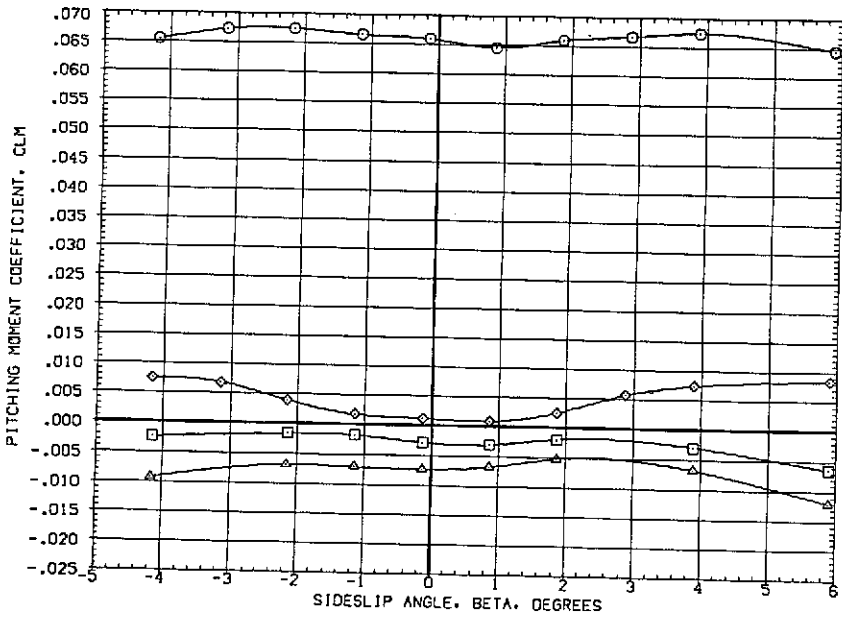
(k) Pitching moment at $M = 1.98$.

(l) Pitching moment at $M = 2.17$.
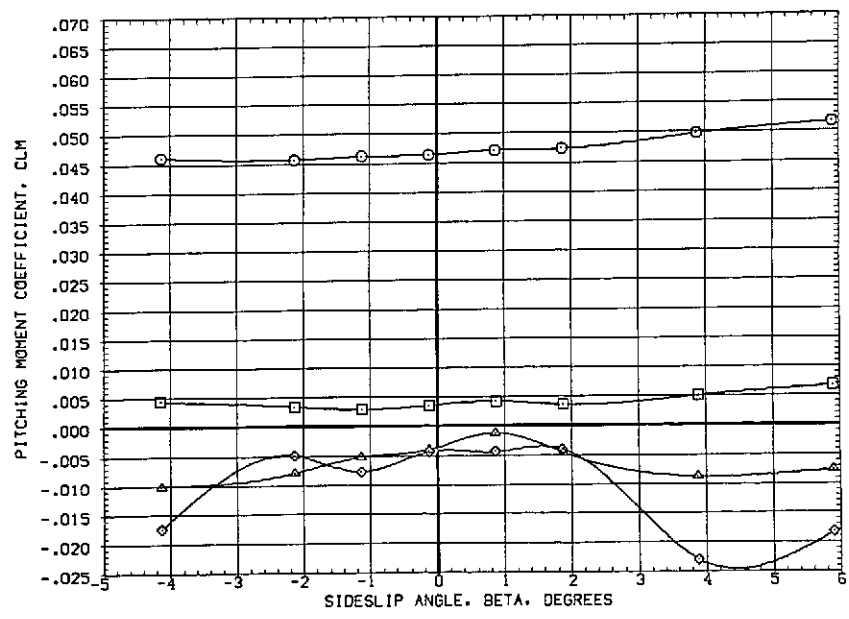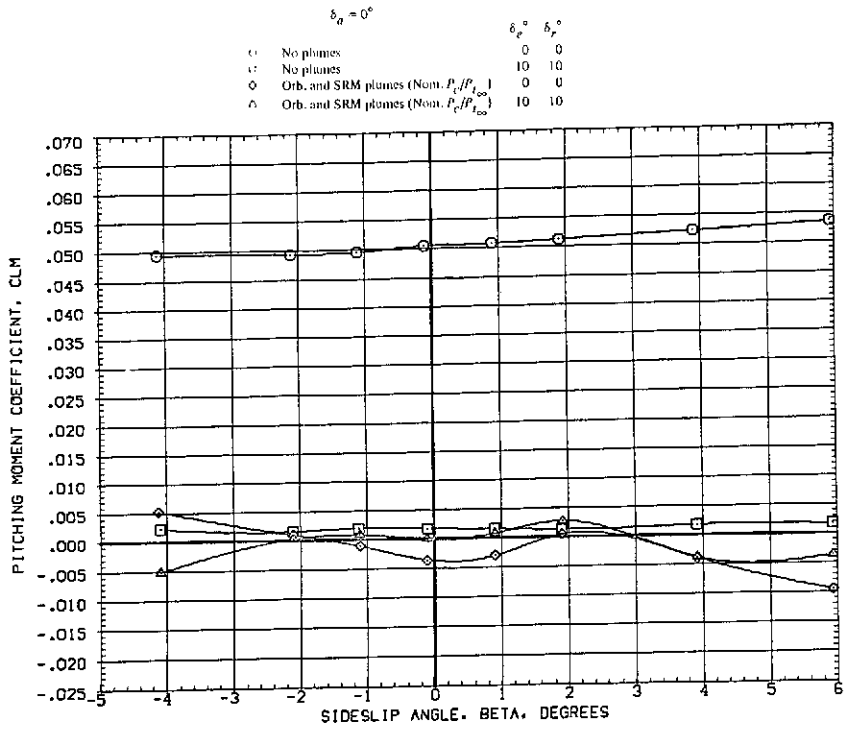
Figure 18.– Continued.
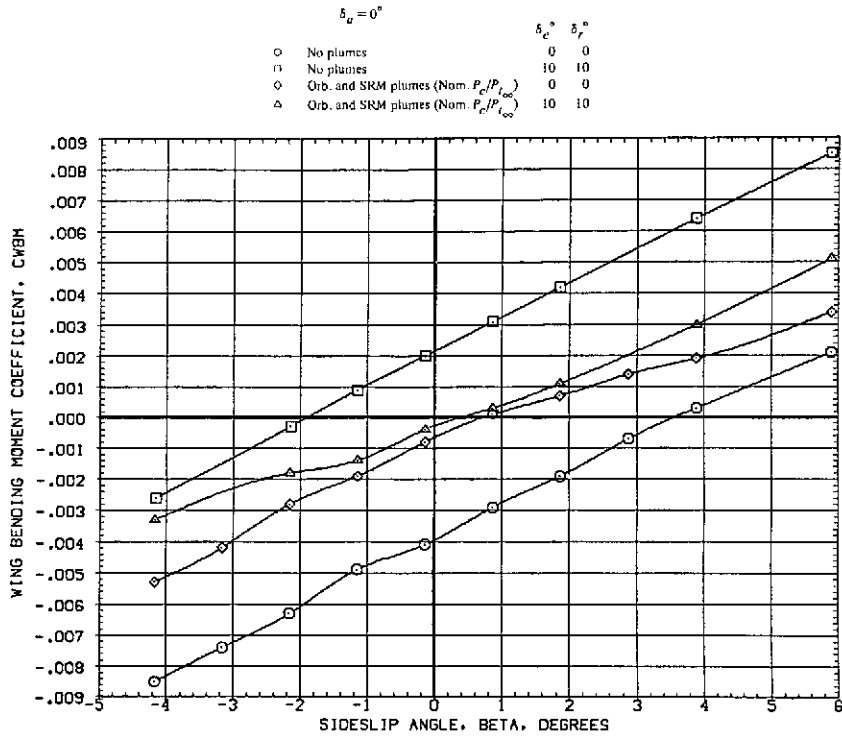
(m) Wing bending moment at $M = 1.60$.
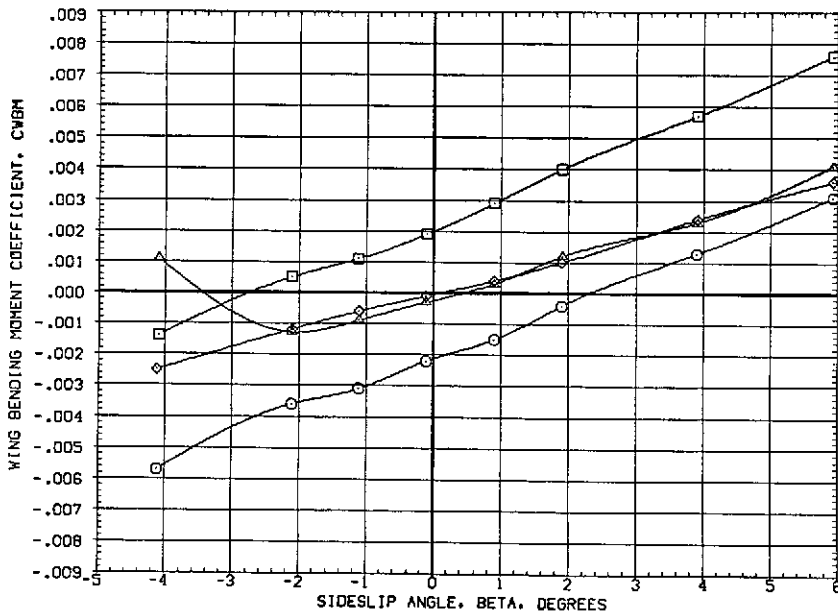
(n) Wing bending moment at $M = 1.98$.

Figure 18.– Continued.
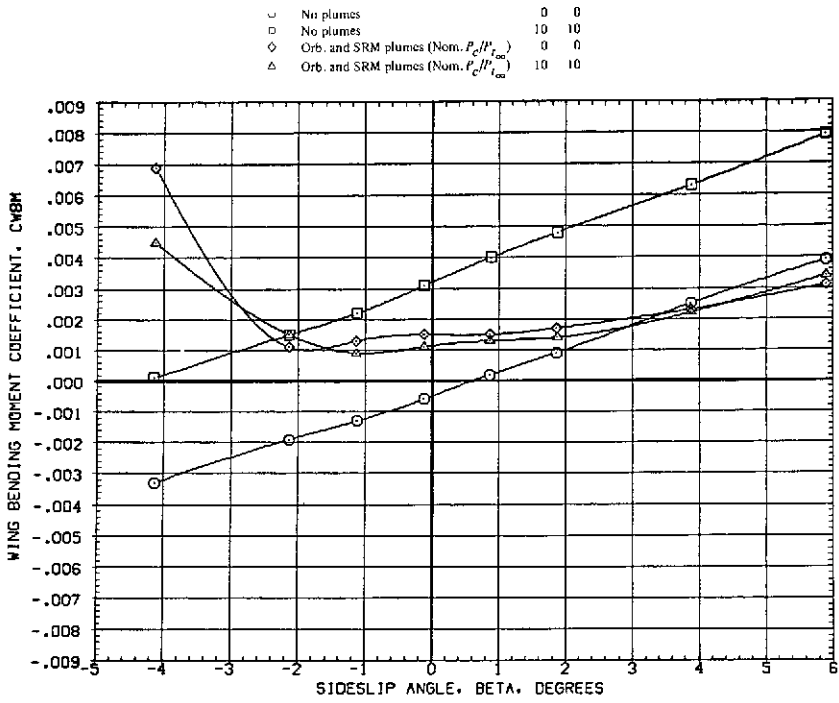
(o) Wing bending moment at $M = 2.17$.
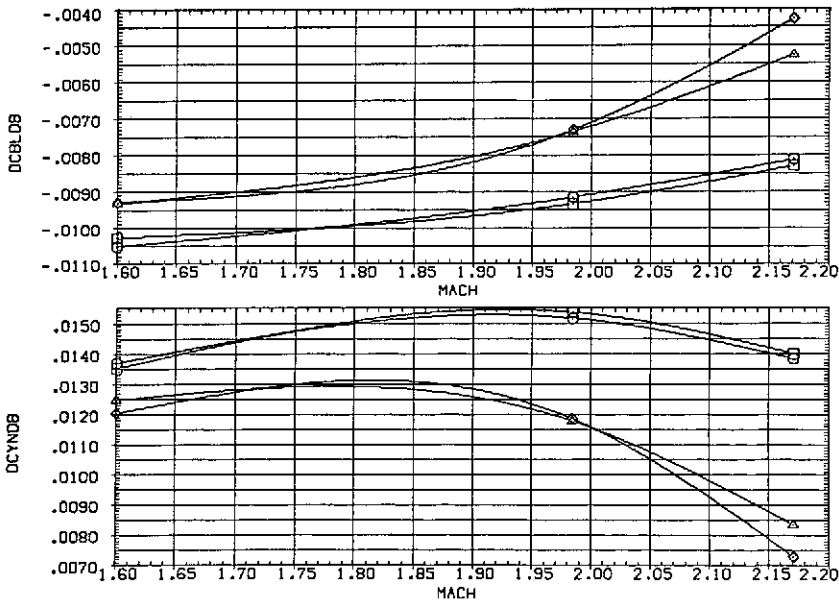
(p) Rolling and yawing — moment derivatives vs. M.

Figure 18.— Concluded.

$\delta_e = \delta_r = 0^\circ; \delta_a = 10^\circ$

o No plumes
◻ Orb. and SRM plumes (Nom. P_c/P_{T_∞}; SRM $A/A^* = 8$)
◇ Smaller SRM plumes (Nom. Orb. plumes; SRM $A/A^* = 12$)
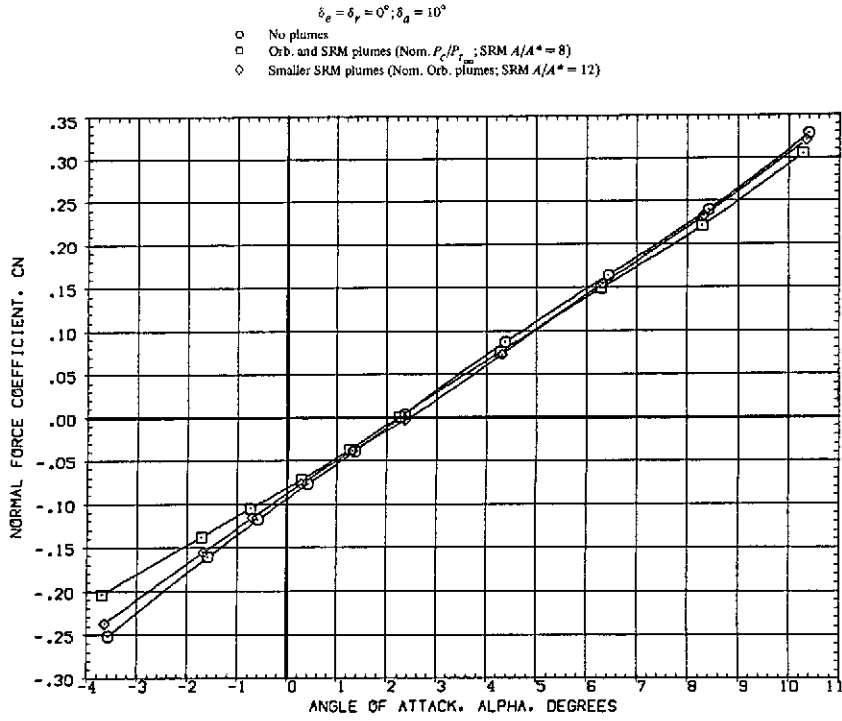
(a) Normal force vs. angle of attack.
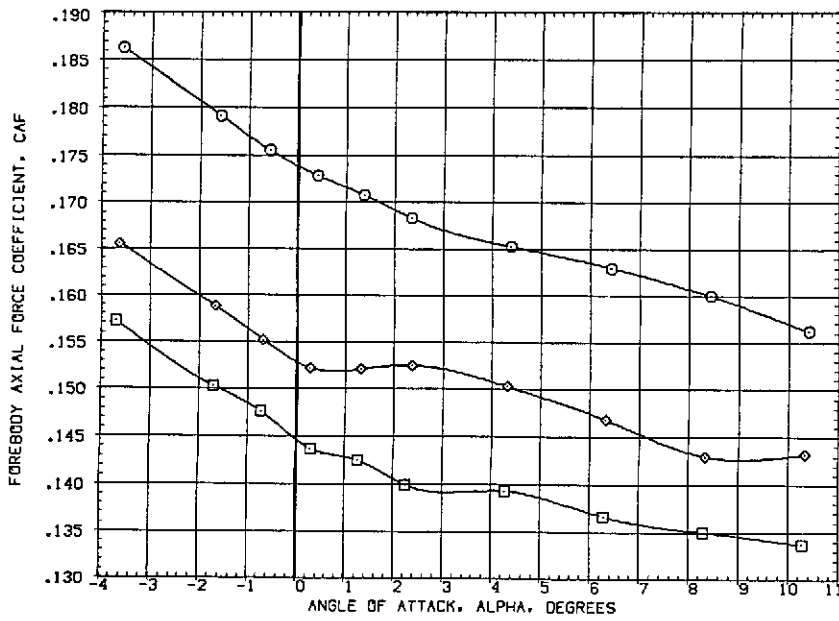
(b) Forebody axial force.

Figure 19.— Effect of plumes on the aileron power at $\beta = 0^\circ$ and $M = 1.98$.

○ No plumes
◻ Orb. and SRM plumes (Nom. P_c/P_{f_∞}; SRM $A/A^* = 8$)
◇ Smaller SRM plumes (Nom. Orb. plumes; SRM $A/A^* = 12$)
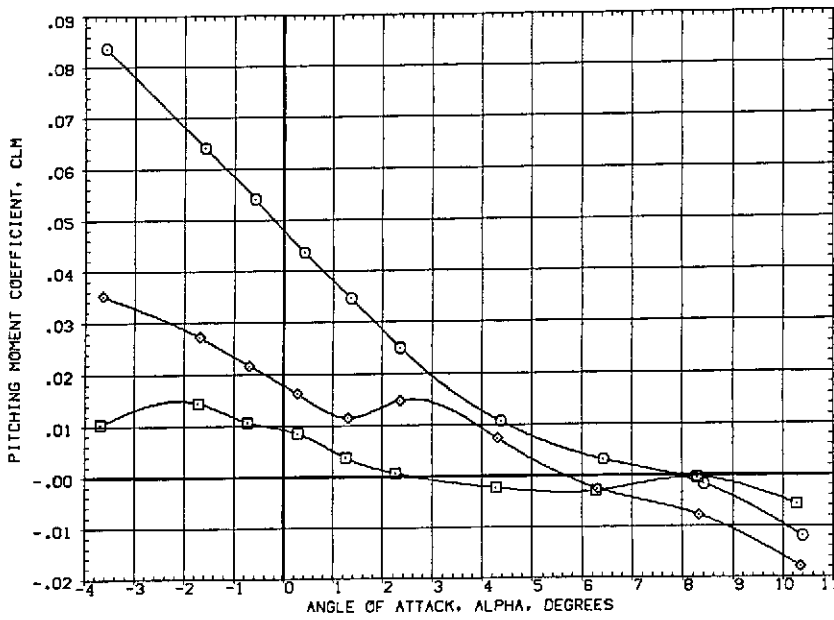
(c) Pitching moment.
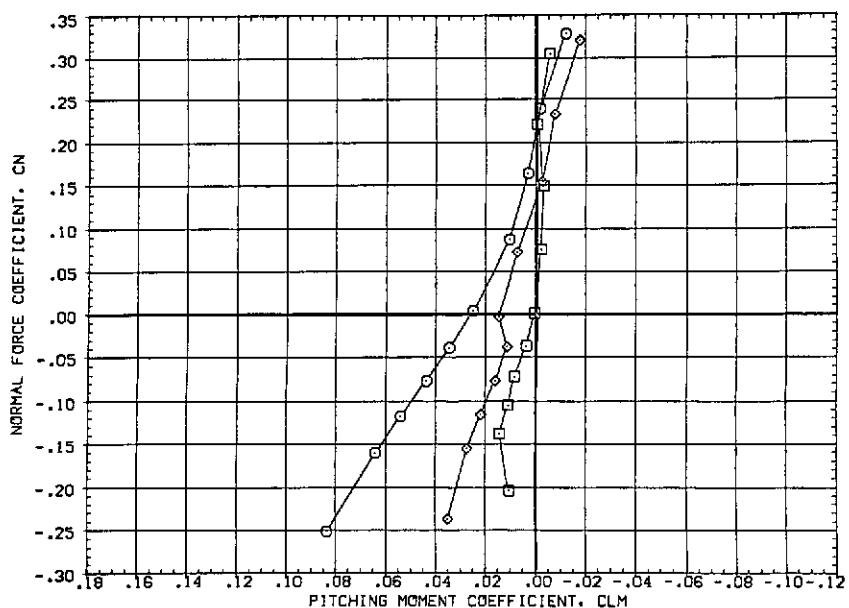
(d) Normal force vs. pitching moment.

Figure 19.— Continued.

$\delta_e = \delta_r = 0°; \delta_a = 10°$

○ No plumes
□ Orb. and SRM plumes (Nom. P_c/P_{t_∞}; SRM $A/A^* = 8$)
◇ Smaller SRM plumes (Nom. Orb. plumes; SRM $A/A^* = 12$)
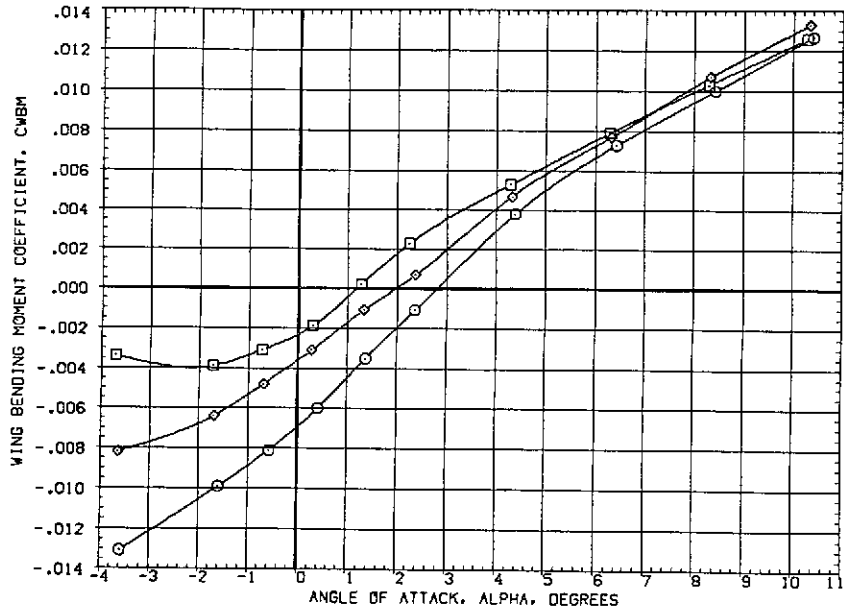
(e) Wing bending moment.
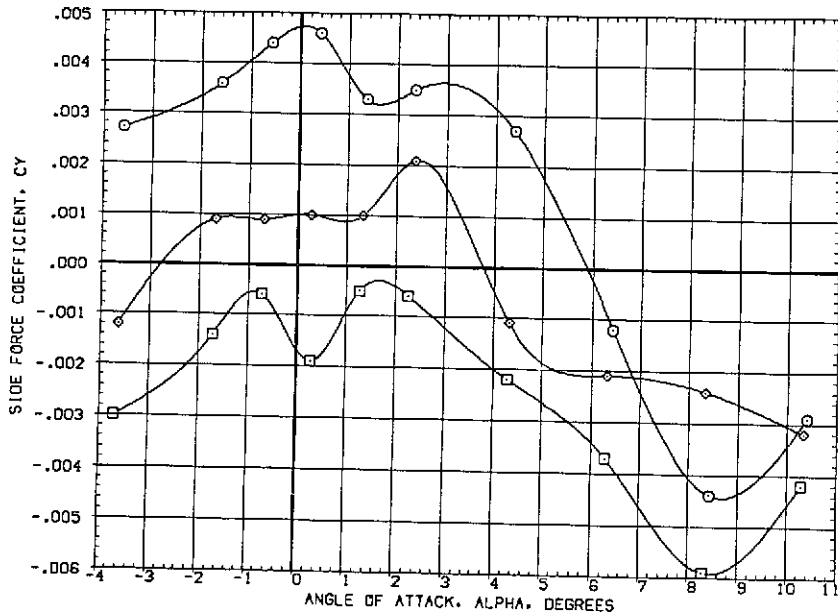
(f) Side force.

Figure 19.— Continued.

$\delta_e = \delta_r = 0°; \delta_a = 10°$

   ○ No plumes
   □ Orb. and SRM plumes (Nom. $P_c/P_{t_{\infty}}$; SRM $A/A^* = 8$)
   ◇ Smaller SRM plumes (Nom. Orb. plumes; SRM $A/A^* = 12$)
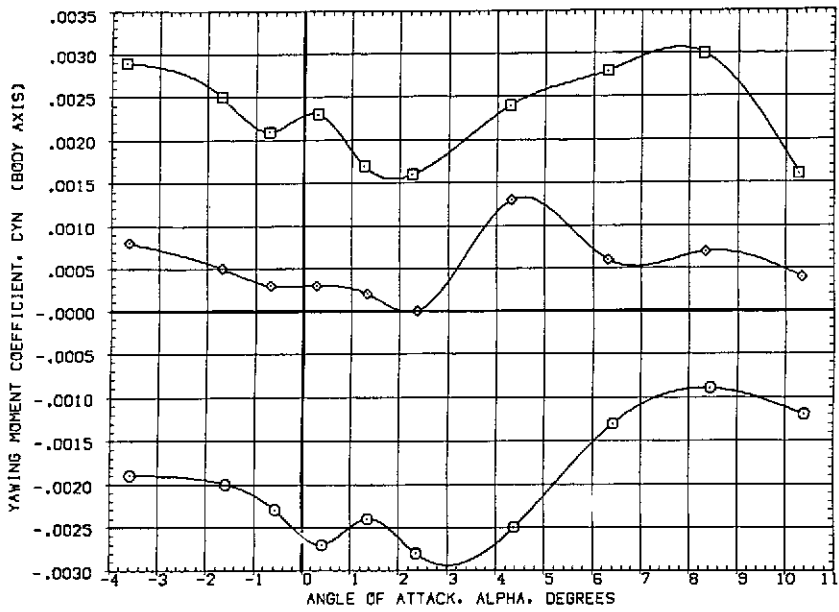
(g) Yawing moment.
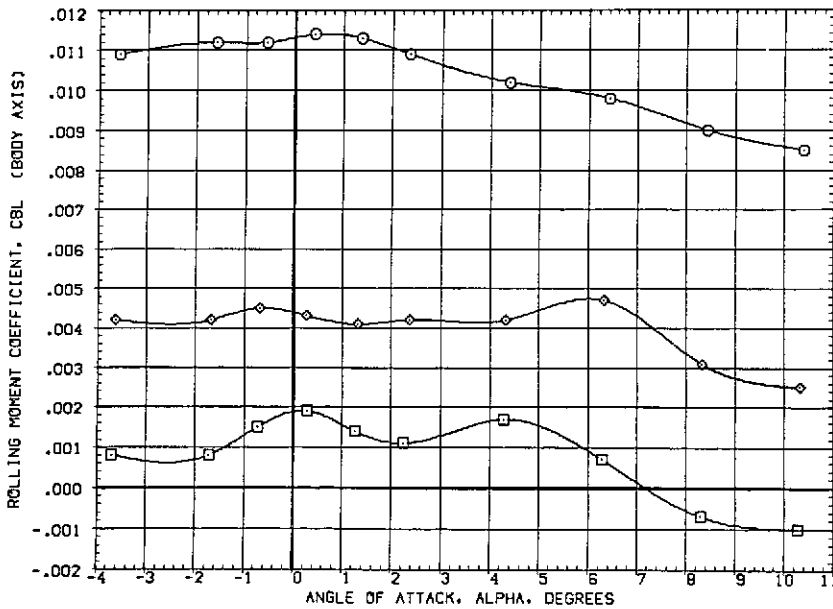
(h) Rolling moment.

Figure 19.-- Concluded.

107

$\delta_e = \delta_r = 0°$

		$\delta_a°$
◯	No plumes	0
◻	No plumes	10
◇	Orb. and SRM plumes (Nom. P_c/P_{t_∞})	0
△	Orb. and SRM plumes (Nom. P_c/P_{t_∞})	10
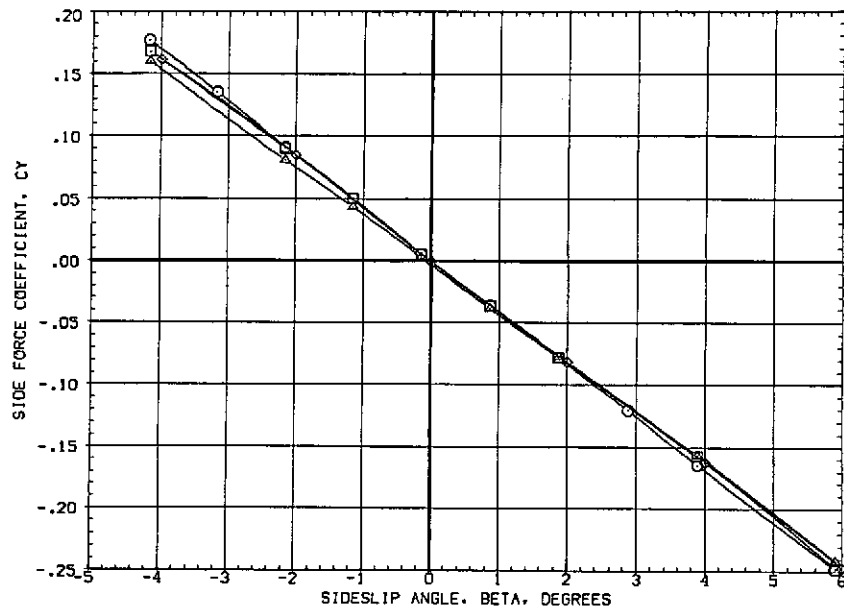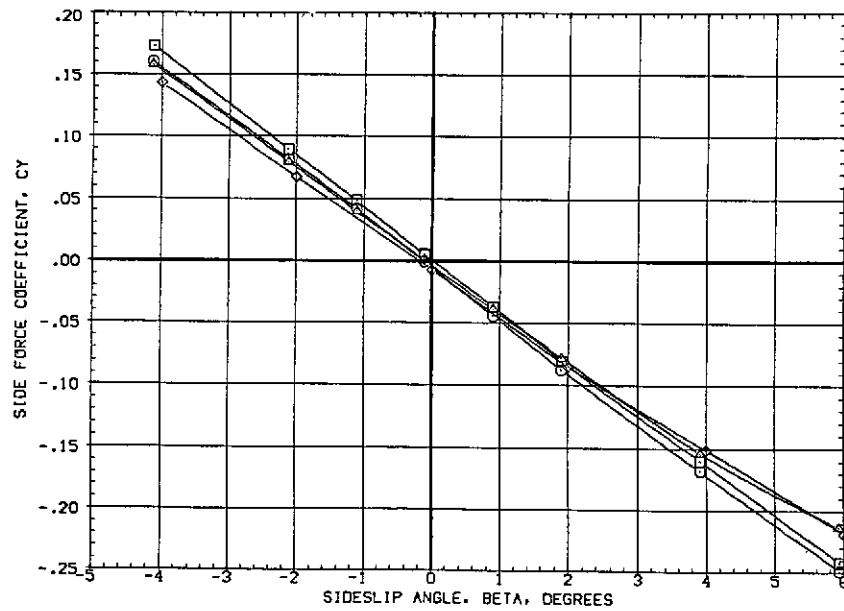
(a) Side force at $M = 1.60$.

(b) Side force at $M = 1.98$.

Figure 20.— Effect of plumes on the aileron power at $\alpha = 0°$.

$\delta_e = \delta_r = 0°$

		$\delta_a°$
○	No plumes	0
□	No plumes	10
◇	Orb. and SRM plumes (Nom. P_c/P_{t_∞})	0
△	Orb. and SRM plumes (Nom. P_c/P_{t_∞})	10

YAWING MOMENT COEFFICIENT, CYN (BODY AXIS)

SIDESLIP ANGLE, BETA, DEGREES

(c) Yawing moment at $M = 1.60$.

YAWING MOMENT COEFFICIENT, CYN (BODY AXIS)

SIDESLIP ANGLE, BETA, DEGREES

(d) Yawing moment at $M = 1.98$.

Figure 20.– Continued.

$\delta_e = \delta_r = 0°$

		$\delta_a°$
○	No plumes	0
◲	No plumes	10
◇	Orb. and SRM plumes (Nom. P_c/P_{t_∞})	0
△	Orb. and SRM plumes (Nom. P_c/P_{t_∞})	10

(e) Rolling moment at $M = 1.60$.

(f) Rolling moment at $M = 1.98$.

Figure 20.-- Continued.

110

$\delta_c + \delta_r = 0^\circ$

		δ_a°
○	No plumes	0
□	No plumes	10
◇	Orb. and SRM plumes (Nom. P_c/P_{t_∞})	0
△	Orb. and SRM plumes (Nom. P_c/P_t)	10

(g) Pitching moment at $M = 1.60$.

(h) Pitching moment at $M = 1.98$.

Figure 20.– Continued.

$\delta_e = \delta_r = 0°$

		δ_a°
○	No plumes	0
□	No plumes	10
◇	Orb. and SRM plumes (Nom. P_c/P_{t_∞})	0
△	Orb. and SRM plumes (Nom. P_c/P_{t_∞})	10

(i) Wing bending moment at $M = 1.60$.

(j) Wing bending moment at $M = 1.98$.

Figure 20.– Concluded.

(a) Normal force vs. angle of attack at $M = 1.60$.

(b) Normal force vs. angle of attack at $M = 1.98$.

Figure 21.— Effect of the size of the plumes on the elevon and rudder power at $\beta = 0°$.

Orbiter and SRM plumes; $\delta_a = 0°$

		$\delta_e°$	$\delta_r°$
○	Nom. plumes (P_c/P_{t_∞} Nom.; SRM $A/A^* = 8$)	0	0
□	Nom. plumes (P_c/P_{t_∞} Nom.; SRM $A/A^* = 8$)	10	10
◇	Smaller SRM plumes (Nom. Orb. plumes; SRM $A/A^* = 12$)	0	0
△	Smaller SRM plumes (Nom. Orb. plumes; SRM $A/A^* = 12$)	10	10
△	Larger plumes (Orb. and SRM $P_c/P_{t_\infty} = 1.3$ Nom.)	0	0
▷	Larger plumes (Orb. and SRM $P_c/P_{t_\infty} = 1.3$ Nom.)	10	10

(c) Forebody axial force at $M = 1.60$.
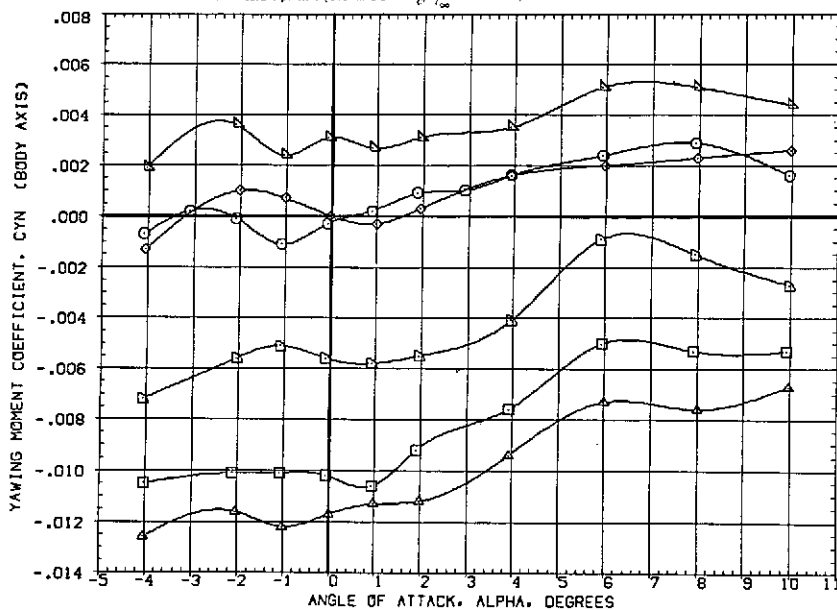

(d) Forebody axial force at $M = 1.98$.

Figure 21.— Continued.

114

		$\delta_e°$	$\delta_r°$
○	Nom. plumes (P_c/P_{t_∞} Nom.; SRM $A/A^* = 8$)	0	0
□	Nom. plumes (P_c/P_{t_∞} Nom.; SRM $A/A^* = 8$)	10	10
◇	Smaller SRM plumes (Nom. Orb. plumes; SRM $A/A^* = 12$)	0	0
△	Smaller SRM plumes (Nom. Orb. plumes; SRM $A/A^* = 12$)	10	10
◁	Larger plumes (Orb. and SRM $P_c/P_{t_\infty} = 1.3$ Nom.)	0	0
◁	Larger plumes (Orb. and SRM $P_c/P_t = 1.3$ Nom.)	10	10

(e) Pitching moment at $M = 1.60$.

(f) Pitching moment at $M = 1.98$.

Figure 21.– Continued.

115

		$\delta_e°$	$\delta_r°$
○	Nom. plumes (P_c/P_{t_∞} Nom.; SRM $A/A^* = 8$)	0	0
◔	Nom. plumes (P_c/P_{t_∞} Nom.; SRM $A/A^* = 8$)	10	10
◇	Smaller SRM plumes (Nom. Orb. plumes; SRM $A/A^* = 12$)	0	0
△	Smaller SRM plumes (Nom. Orb. plumes; SRM $A/A^* = 12$)	10	10
⬚	Larger plumes (Orb. and SRM $P_c/P_{t_\infty} = 1.3$ Nom.)	0	0
⬚	Larger plumes (Orb. and SRM $P_c/P_{t_\infty} = 1.3$ Nom.)	10	10

(g) Normal force vs. pitching moment at $M = 1.60$.

(h) Normal force vs. pitching moment at $M = 1.98$.

Figure 21.— Continued.

116

		δ_e°	δ_r°
○	Nom. plumes (P_c/P_{t_∞} Nom.; SRM $A/A^* = 8$)	0	0
□	Nom. plumes (P_c/P_{t_∞} Nom.; SRM $A/A^* = 8$)	10	10
◇	Smaller SRM plumes (Nom. Orb. plumes; SRM $A/A^* = 12$)	0	0
△	Smaller SRM plumes (Nom. Orb. plumes; SRM $A/A^* = 12$)	10	10
◁	Larger plumes (Orb. and SRM $P_c/P_{t_\infty} = 1.3$ Nom.)	0	0
▷	Larger plumes (Orb. and SRM $P_c/P_{t_\infty} = 1.3$ Nom.)	10	10

(i) Wing bending moment at $M = 1.6$.

(j) Wing bending moment at $M = 1.98$.

Figure 21.— Continued.

117

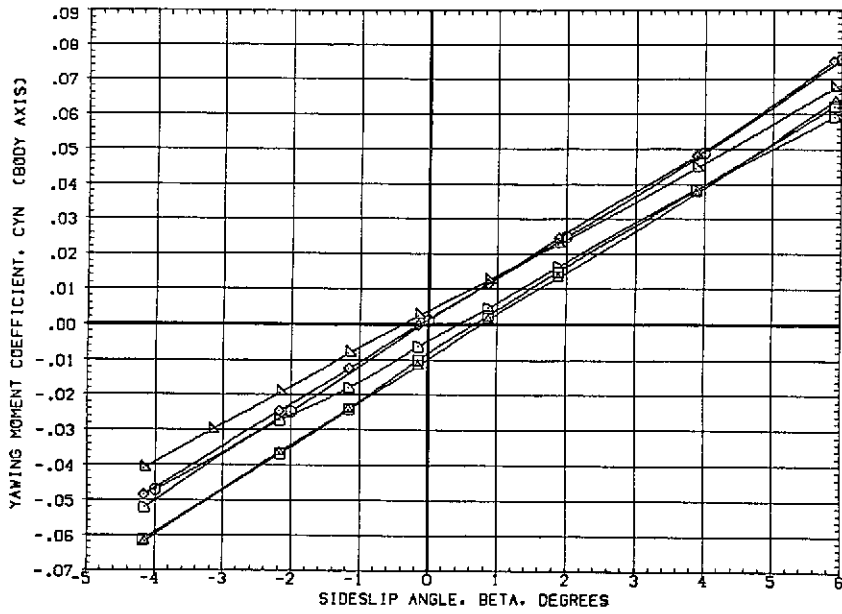|		$\delta_e°$	$\delta_r°$
○	Nom. plumes (P_c/P_{t_∞} Nom.; SRM $A/A^* = 8$)	0	0
□	Nom. plumes (P_c/P_{t_∞} Nom.; SRM $A/A^* = 8$)	10	10
◇	Smaller SRM plumes (Nom. Orb. plumes; SRM $A/A^* = 12$)	0	0
△	Smaller SRM plumes (Nom. Orb. plumes; SRM $A/A^* = 12$)	10	10
◁	Larger plumes (Orb. and SRM $P_c/P_{t_\infty} = 1.3$ Nom.)	0	0
◁	Larger plumes (Orb. and SRM $P_c/P_{t_\infty} = 1.3$ Nom.)	10	10

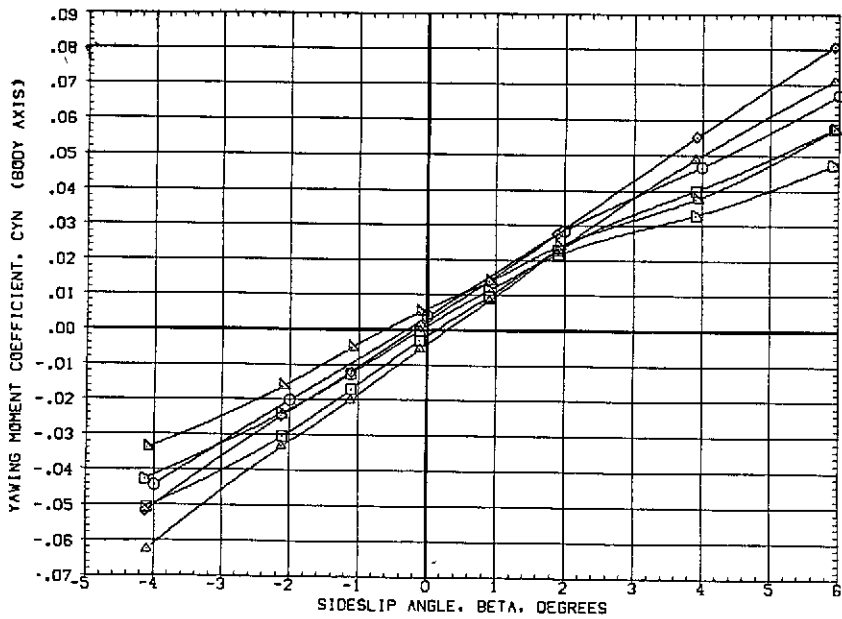(k) Side force at $M = 1.60$.

(l) Side force at $M = 1.98$.

Figure 21.– Continued.

118

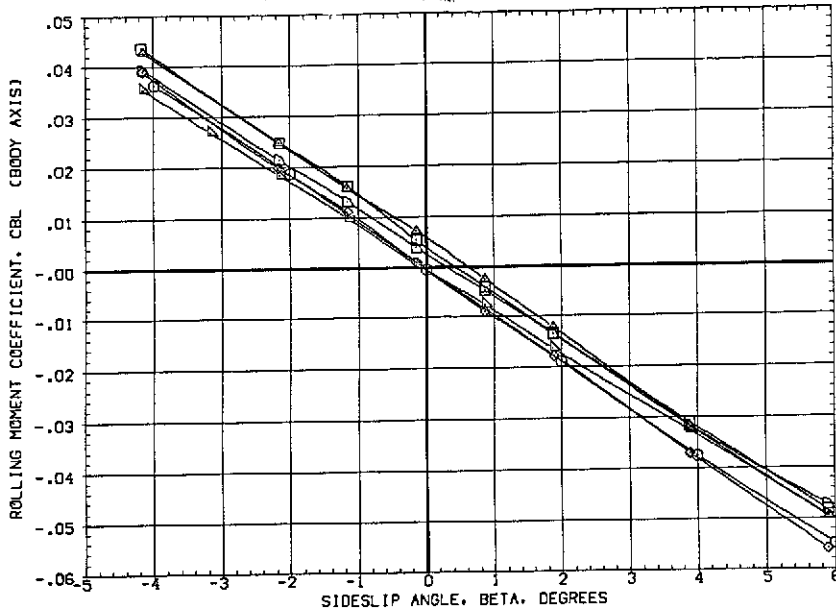|		$\delta_e°$	$\delta_r°$
O	Nom. plumes (P_c/P_{t_∞} Nom.; SRM $A/A^* = 8$)	0	0
□	Nom. plumes (P_c/P_{t_∞} Nom.; SRM $A/A^* = 8$)	10	10
◇	Smaller SRM plumes (Nom. Orb. plumes; SRM $A/A^* = 12$)	0	0
△	Smaller SRM plumes (Nom. Orb. plumes; SRM $A/A^* = 12$)	10	10
◭	Larger plumes (Orb. and SRM $P_c/P_{t_\infty} = 1.3$ Nom.)	0	0
◮	Larger plumes (Orb. and SRM $P_c/P_{t_\infty} = 1.3$ Nom.)	10	10

(m) Yawing moment at $M = 1.60$.

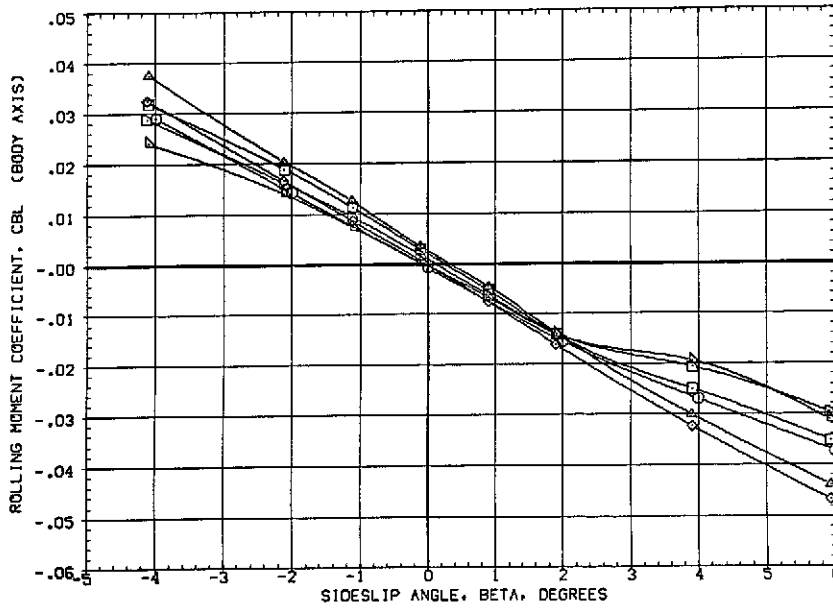(n) Yawing moment at $M = 1.98$.

Figure 21.– Continued.

119

		$\delta_e°$	$\delta_r°$
o	Nom. plumes $(P_c/P_{t_\infty}$ Nom.; SRM $A/A^* = 8)$	0	0
□	Nom. plumes $(P_c/P_{t_\infty}$ Nom.; SRM $A/A^* = 8)$	10	10
◇	Smaller SRM plumes (Nom. Orb. plumes; SRM $A/A^* = 12)$	0	0
△	Smaller SRM plumes (Nom. Orb. plumes; SRM $A/A^* = 12)$	10	10
◁	Larger plumes (Orb. and SRM $P_c/P_{t_\infty} = 1.3$ Nom.)	0	0
◁	Larger plumes (Orb. and SRM $P_c/P_{t_\infty} = 1.3$ Nom.)	10	10

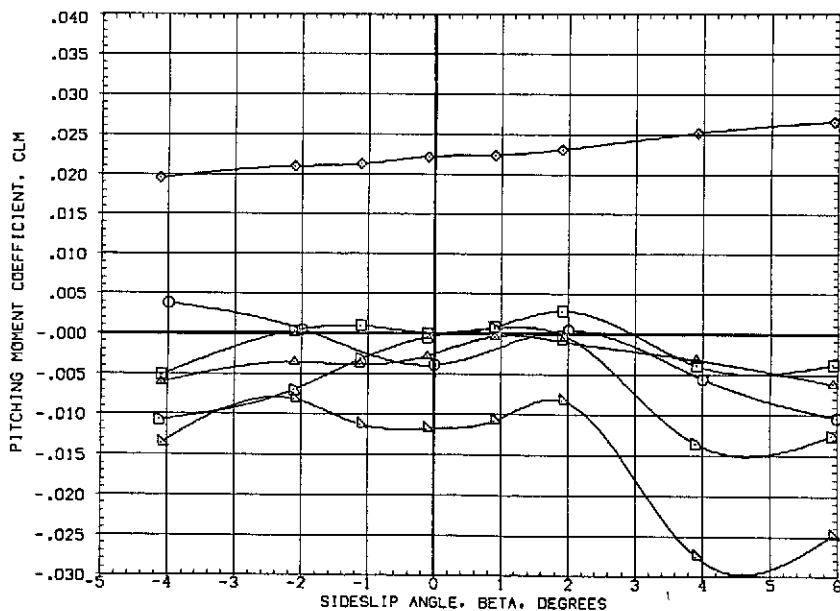(o) Rolling moment at $M = 1.60$.

(p) Rolling moment at $M = 1.98$.

Figure 21.– Concluded.

Orbiter and SRM plumes; $\delta_a = 0°$

		$\delta_e°$	$\delta_r°$
⊓	Nom. plumes (P_t/P_{t_∞} Nom.; SRM $A/A^* = 8$)	0	0
⊓	Nom. plumes (P_t/P_{t_∞} Nom.; SRM $A/A^* = 8$)	10	10
◊	Smaller SRM plumes (Nom. Orb. plumes; SRM $A/A^* = 12$)	0	0
△	Smaller SRM plumes (Nom. Orb. plumes; SRM $A/A^* = 12$)	10	10
◻	Larger plumes (Orb. and SRM $P_c/P_{t_\infty} = 1.3$ Nom.)	0	0
◻	Larger plumes (Orb. and SRM $P_c/P_{t_\infty} = 1.3$ Nom.)	10	10

(a) Side force at $M = 1.60$.

(b) Side force at $M = 2.00$.

Figure 22.— Effect of the size of the plumes on the elevon and rudder power at $\alpha = 0°$.

		$\delta_e^{\,\circ}$	$\delta_r^{\,\circ}$
⊡	Nom. plumes $(P_c/P_{t_\infty}$ Nom.; SRM $A/A^* = 8)$	0	0
⊡	Nom. plumes $(P_c/P_{t_\infty}$ Nom.; SRM $A/A^* = 8)$	10	10
◇	Smaller SRM plumes (Nom. Orb. plumes; SRM $A/A^* = 12$)	0	0
△	Smaller SRM plumes (Nom. Orb. plumes; SRM $A/A^* = 12$)	10	10
◣	Larger plumes (Orb. and SRM $P_c/P_{t_\infty} = 1.3$ Nom.)	0	0
◺	Larger plumes (Orb. and SRM $P_c/P_{t_\infty} = 1.3$ Nom.)	10	10

(c) Yawing moment at $M = 1.60$.

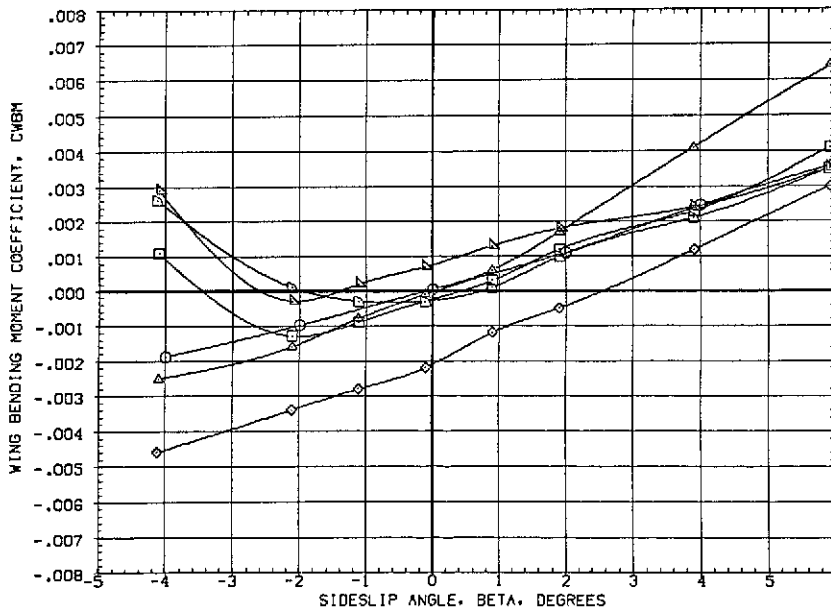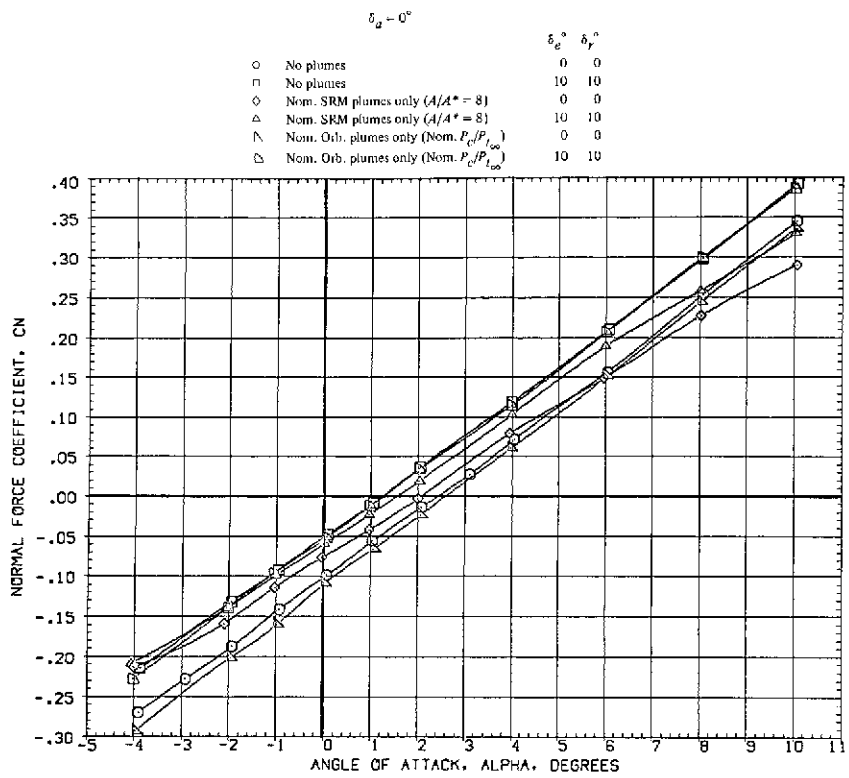(d) Yawing moment at $M = 2.00$.

Figure 22.– Continued.

		$\delta_e^°$	$\delta_r^°$
○	Nom. plumes (P_c/P_{t_∞} Nom.; SRM $A/A^* = 8$)	0	0
□	Nom. plumes (P_c/P_{t_∞} Nom.; SRM $A/A^* = 8$)	10	10
◇	Smaller SRM plumes (Nom. Orb. plumes; SRM $A/A^* = 12$)	0	0
△	Smaller SRM plumes (Nom. Orb. plumes; SRM $A/A^* = 12$)	10	10
◺	Larger plumes (Orb. and SRM $P_c/P_{t_\infty} = 1.3$ Nom.)	0	0
◹	Larger plumes (Orb. and SRM $P_c/P_{t_\infty} = 1.3$ Nom.)	10	10

(e) Rolling moment at $M = 1.60$.

(f) Rolling moment at $M = 2.00$.

Figure 22.– Continued.

		$\delta_c^{\,\circ}$	$\delta_r^{\,\circ}$
○	Nom. plumes $(P_c/P_{t_\infty}$ Nom.; SRM $A/A^* = 8)$	0	0
⊡	Nom. plumes $(P_c/P_{t_\infty}$ Nom.; SRM $A/A^* = 8)$	10	10
◇	Smaller SRM plumes (Nom. Orb. plumes; SRM $A/A^* = 12)$	0	0
△	Smaller SRM plumes (Nom. Orb. plumes; SRM $A/A^* = 12)$	10	10
◿	Larger plumes (Orb. and SRM $P_c/P_{t_\infty} = 1.3$ Nom.)	0	0
◺	Larger plumes (Orb. and SRM $P_c/P_{t_\infty} = 1.3$ Nom.)	10	10

(g) Pitching moment at $M = 1.60$.

(h) Pitching moment at $M = 2.00$.

Figure 22.– Continued.

		δ_t°	δ_r°
ᴄ	Nom. plumes (P_c/P_{t_∞} Nom.; SRM $A/A^* = 8$)	0	0
⊓	Nom. plumes (P_c/P_{t_∞} Nom.; SRM $A/A^* = 8$)	10	10
◇	Smaller SRM plumes (Nom. Orb. plumes; SRM $A/A^* = 12$)	0	0
△	Smaller SRM plumes (Nom. Orb. plumes; SRM $A/A^* = 12$)	10	10
◁	Larger plumes (Orb. and SRM $P_c/P_{t_\infty} = 1.3$ Nom.)	0	0
◁	Larger plumes (Orb. and SRM $P_c/P_{t_\infty} = 1.3$ Nom.)	10	10

(i) Wing bending moment at $M = 1.60$.

(j) Wing bending moment at $M = 2.00$.

Figure 22.– Concluded.

125

$\delta_a = 0°$

		$\delta_e°$	$\delta_r°$
O	No plumes	0	0
п	No plumes	10	10
◊	Nom. SRM plumes only $(A/A^* = 8)$	0	0
△	Nom. SRM plumes only $(A/A^* = 8)$	10	10
Ν	Nom. Orb. plumes only (Nom. P_c/P_{t_∞})	0	0
Ⴆ	Nom. Orb. plumes only (Nom. P_c/P_{t_∞})	10	10

(a) Normal force vs. angle of attack at $M = 1.60$.
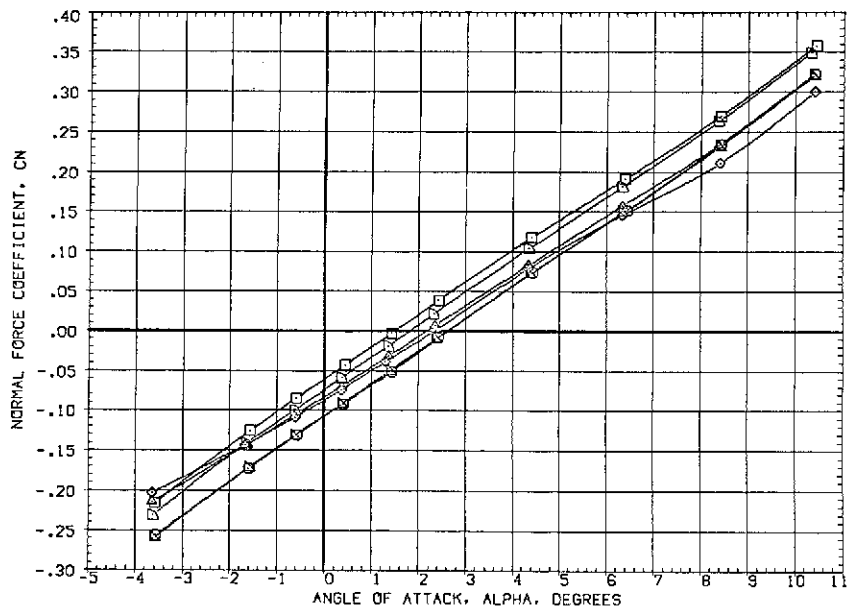
(b) Normal force vs. angle of attack at $M = 1.98$.

Figure 23.— Effect of the orbiter and the solid rocket motor (SRM) plumes on the elevon and rudder power at $\beta = 0°$.

(c) Forebody axial force at $M = 1.60$.

(d) Forebody axial force at $M = 1.98$.

Figure 23.— Continued.

127

(e) Pitching moment at $M = 1.60$.

(f) Pitching moment at $M = 1.98$.

Figure 23.— Continued.

128

$\delta_a = 0°$

		$\delta_e°$	$\delta_r°$
O	No plumes	0	0
◠	No plumes	10	10
◇	Nom. SRM plumes only $(A/A^* = 8)$	0	0
△	Nom. SRM plumes only $(A/A^* = 8)$	10	10
◺	Nom. Orb. plumes only (Nom. P_c/P_{t_∞})	0	0
◿	Nom. Orb. plumes only (Nom. P_c/P_{t_∞})	10	10

(g) Normal force vs. pitching moment at $M = 1.60$.

(h) Normal force vs. pitching moment at $M = 1.98$.
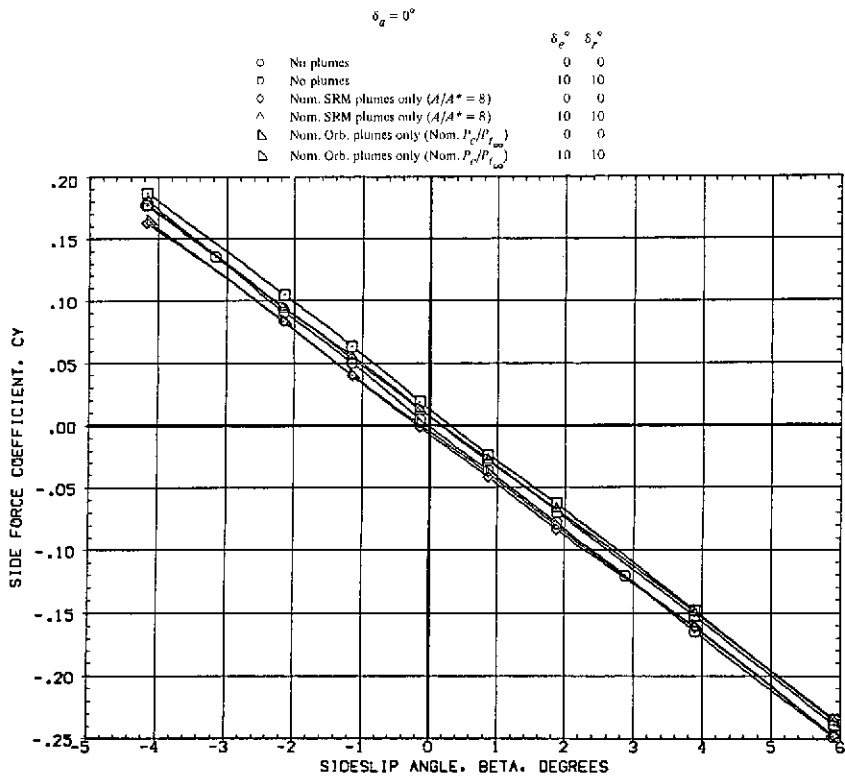
Figure 23.— Continued.

129

(i) Wing bending moment at $M = 1.60$.

(j) Wing bending moment at $M = 1.98$.

Figure 23.— Continued.

(k) Side force at $M = 1.60$.

(l) Side force at $M = 1.98$.

Figure 23.-- Continued.

		$\delta_e°$	$\delta_r°$
○	No plumes	0	0
□	No plumes	10	10
◇	Nom. SRM plumes only $(A/A^* = 8)$	0	0
∧	Nom. SRM plumes only $(A/A^* = 8)$	10	10
◲	Nom. Orb. plumes only (Nom. P_c/P_{t_∞})	0	0
◱	Nom. Orb. plumes only (Nom. P_c/P_{t_∞})	10	10

(m) Yawing moment at $M = 1.60$.

(n) Yawing moment at $M = 1.98$.

Figure 23.— Continued.

132

(o) Rolling moment at $M = 1.60$.

(p) Rolling moment at $M = 1.98$.
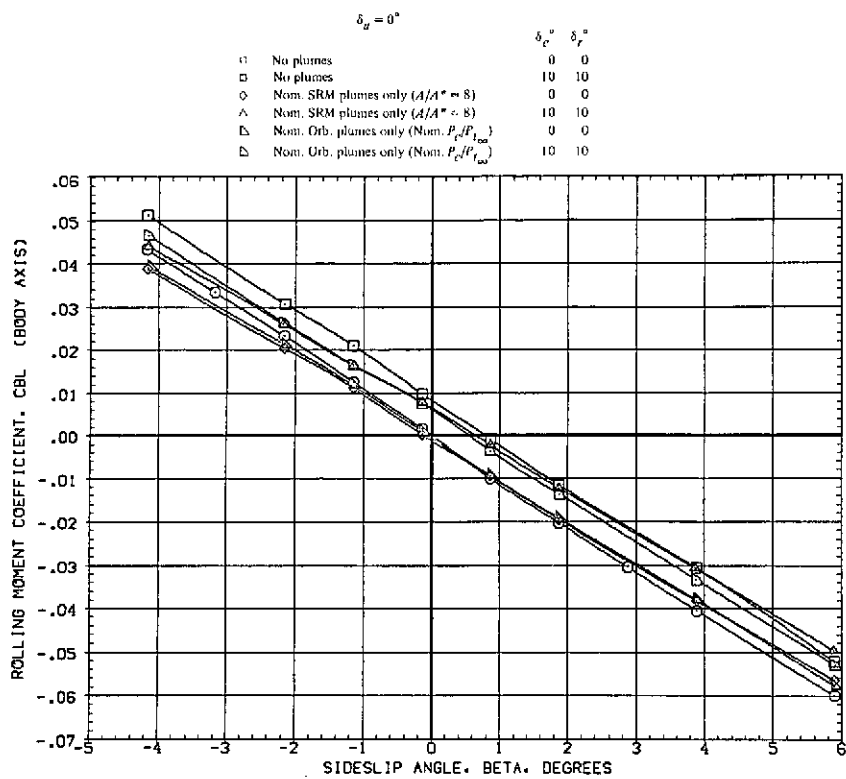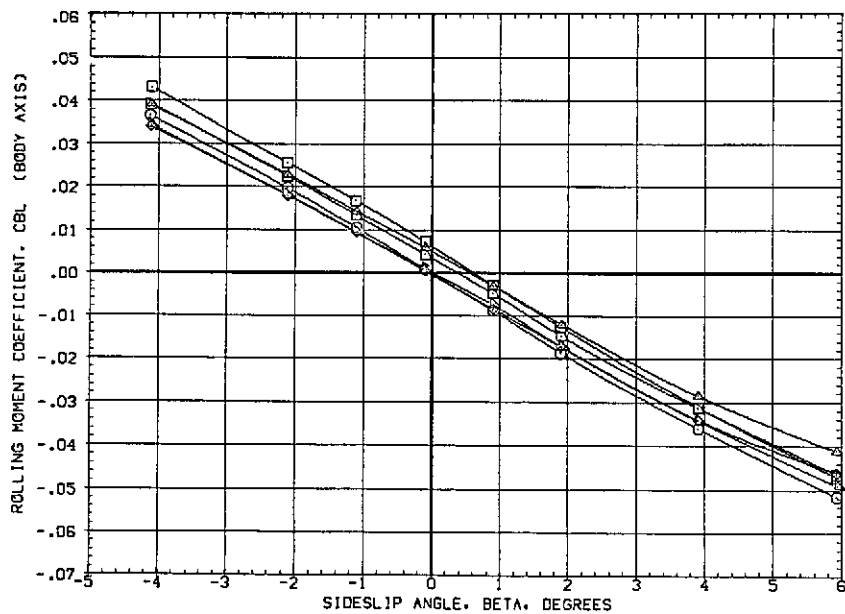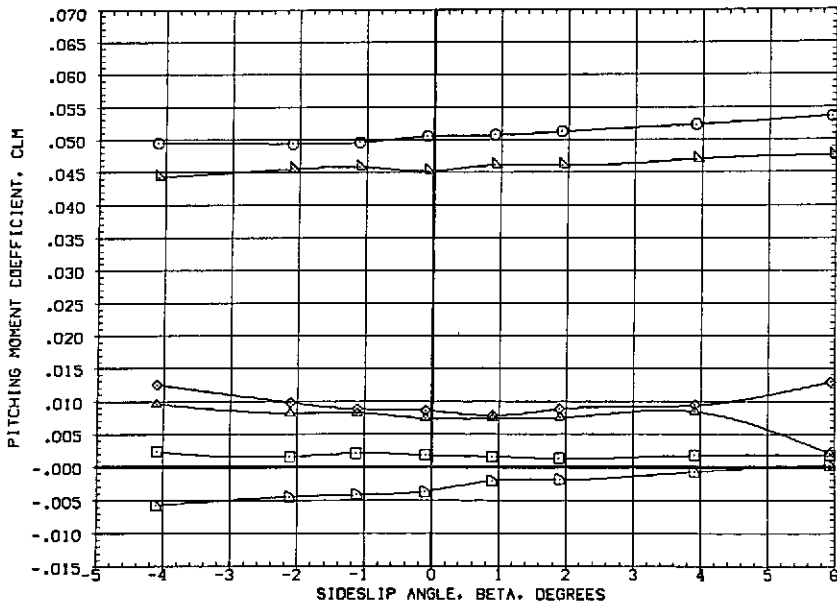
Figure 23.– Concluded.

133

$\delta_q = 0°$

		$\delta_e°$	$\delta_r°$
○	No plumes	0	0
◫	No plumes	10	10
◇	Nom. SRM plumes only ($A/A^* = 8$)	0	0
⋀	Nom. SRM plumes only ($A/A^* = 8$)	10	10
◩	Nom. Orb. plumes only (Nom. P_c/P_{t_∞})	0	0
◭	Nom. Orb. plumes only (Nom. P_c/P_{t_∞})	10	10
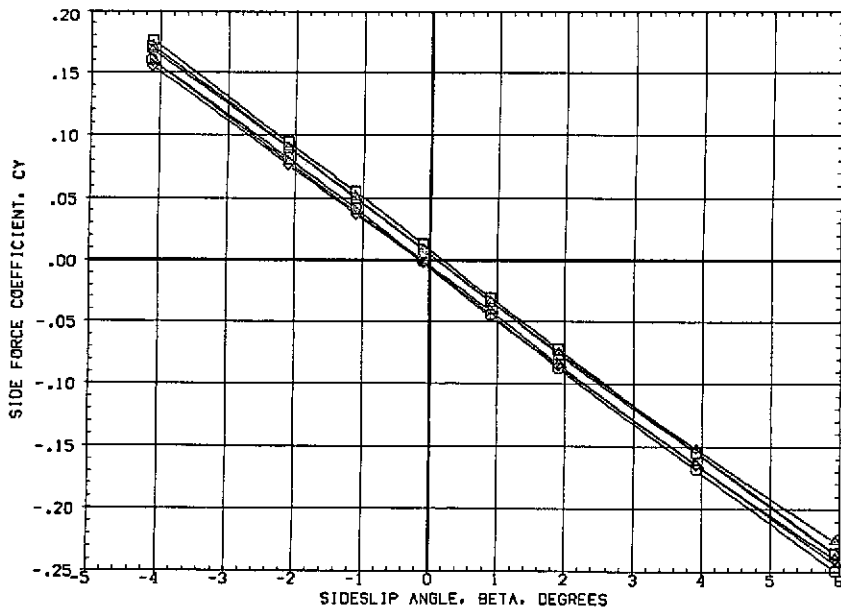
(a) Side force at $M = 1.60$.

(b) Side force at $M = 1.98$.

Figure 24.– Effect of the orbiter and the solid rocket motor (SRM) plumes on the elevon and rudder power at $\alpha = 0°$.

134

		$\delta_e,°$	$\delta_r,°$
○	No plumes	0	0
○	No plumes	10	10
◇	Nom. SRM plumes only $(A/A^* = 8)$	0	0
∧	Nom. SRM plumes only $(A/A^* = 8)$	10	10
△	Nom. Orb. plumes only $(Nom. P_c/P_{t_\infty})$	0	0
□	Nom. Orb. plumes only $(Nom. P_c/P_{t_\infty})$	10	10

(c) Yawing moment at $M = 1.60$.

(d) Yawing moment at $M = 1.98$.

Figure 24.– Continued.

135

		$\delta_{c}^{\,\circ}$	$\delta_{r}^{\,\circ}$
⃝	No plumes	0	0
▢	No plumes	10	10
◇	Nom. SRM plumes only $(A/A^{*} = 8)$	0	0
△	Nom. SRM plumes only $(A/A^{*} = 8)$	10	10
◺	Nom. Orb. plumes only (Nom. $P_{c}/P_{t_{\infty}}$)	0	0
◿	Nom. Orb. plumes only (Nom. $P_{c}/P_{t_{\infty}}$)	10	10

(e) Rolling moment at $M = 1.60$.

(f) Rolling moment at $M = 1.98$.

Figure 24.– Continued.

$\delta_a = 0°$

		$\delta_e°$	$\delta_r°$
⊙	No plumes	0	0
⊡	No plumes	10	10
◇	Nom. SRM plumes only ($A/A^* = 8$)	0	0
△	Nom. SRM plumes only ($A/A^* = 8$)	10	10
◺	Nom. Orb. plumes only (Nom. P_c/P_{t_∞})	0	0
◹	Nom. Orb. plumes only (Nom. P_c/P_{t_∞})	10	10

(g) Pitching moment at $M = 1.60$.

(h) Pitching moment at $M = 1.98$.

Figure 24.-- Continued.

137

$\delta_a = 0°$

		δ_c°	δ_r°
○	No plumes	0	0
○	No plumes	10	10
◇	Nom. SRM plumes only ($A/A^* = 8$)	0	0
△	Nom. SRM plumes only ($A/A^* = 8$)	10	10
△	Nom. Orb. plumes only (Nom. P_c/P_{t_∞})	0	0
△	Nom. Orb. plumes only (Nom. P_c/P_{t_∞})	10	10

(i) Wing bending moment at $M = 1.60$.

(j) Wing bending moment at $M = 1.98$.

Figure 24.– Concluded.

138

Nom. plumes (Nom. P_c/P_{t_∞}; SRM $A/A^* = 8$)

$\delta_a = 0°; \delta_r = 10$

O $M = 1.60$
□ $M = 2.0$
◇ $M = 2.20$
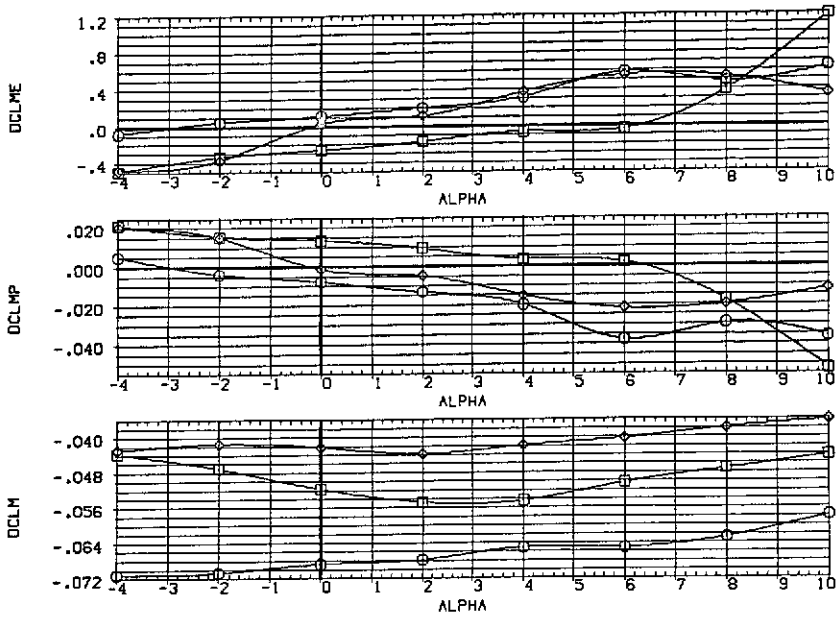
(a) Elevons deflected 10°.
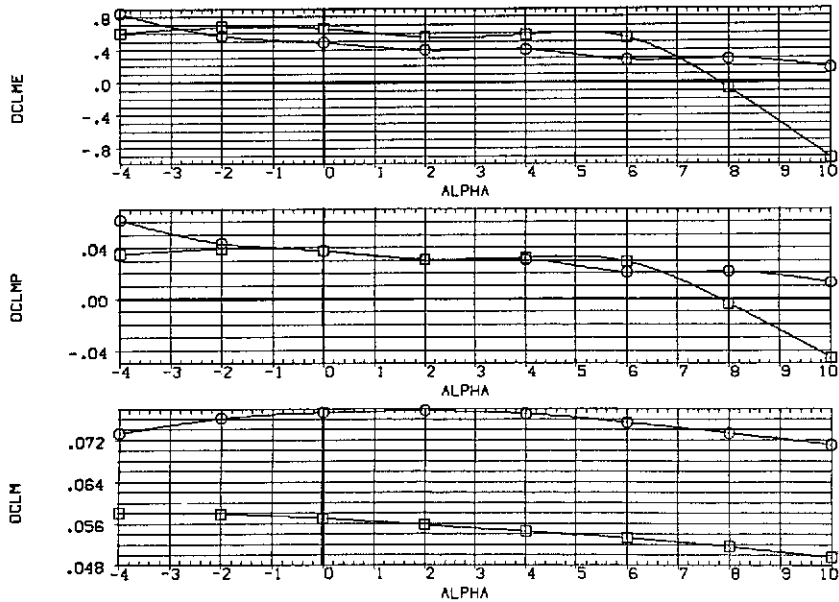
(b) Elevons deflected −10°.

Figure 25.− Effect of the orbiter and the solid rocket motor (SRM) plumes on the elevon effectiveness parameters at $\beta = 0°$
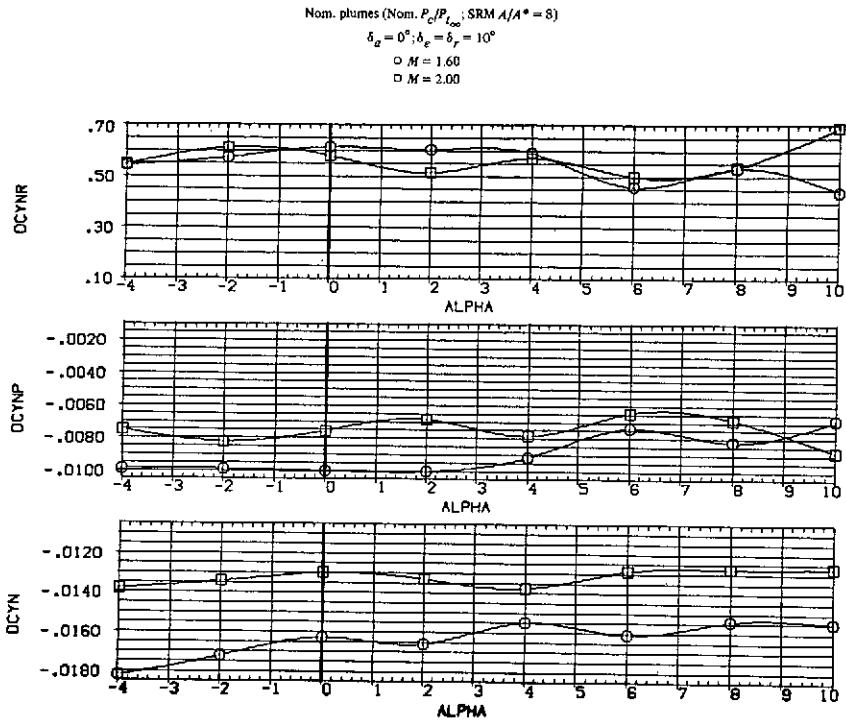
(a) Yawing—moment parameters at $M = 1.60$ and 2.00.
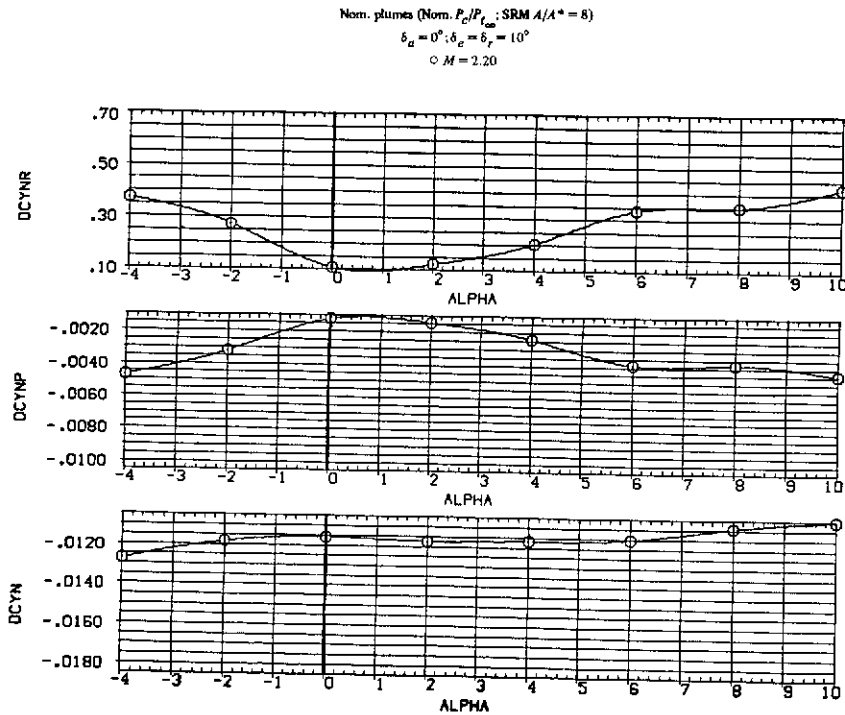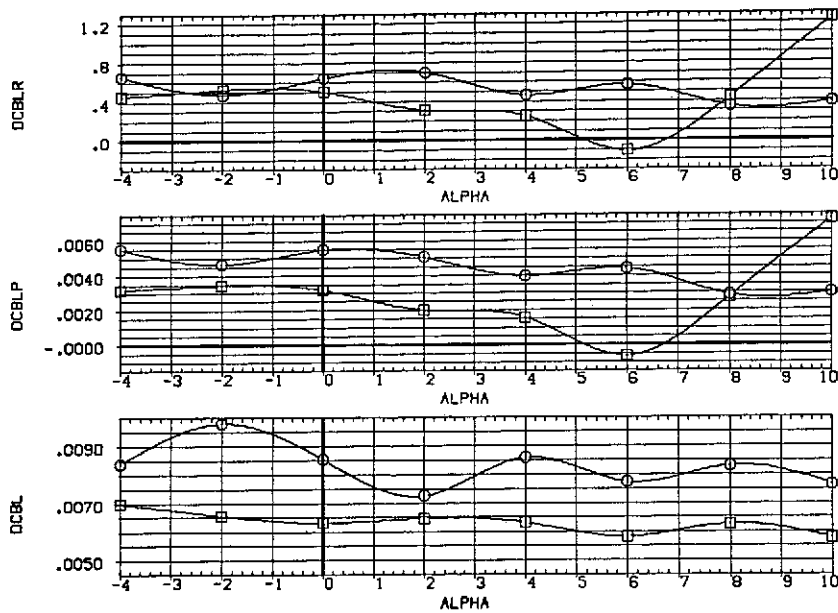
(b) Yawing—moment parameters at $M = 2.20$

Figure 26.— Effect of the orbiter and the solid rocket motor (SRM) plumes on the rudder effectiveness parameters at $\beta = 0°$.

140

(c) Rolling–moment parameters at $M = 1.60$ and 2.00.
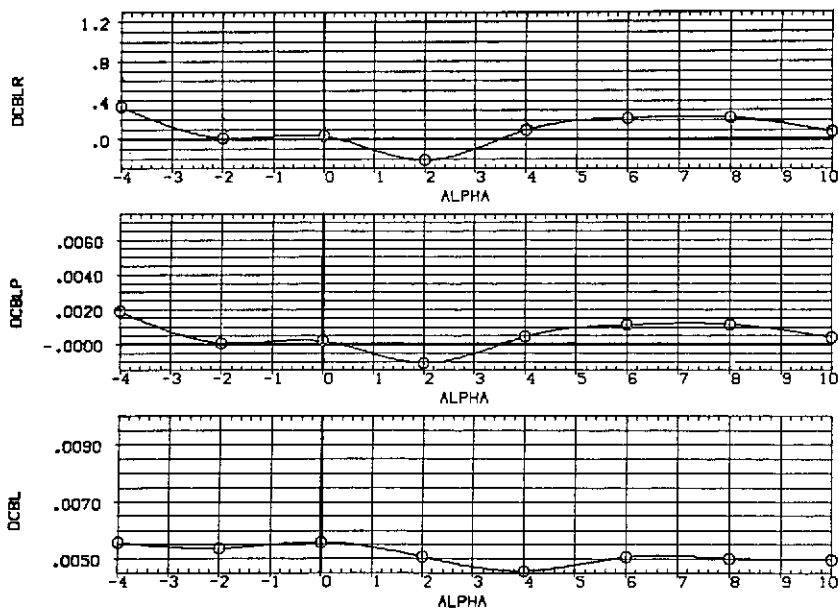
(d) Rolling–moment parameters at $M = 2.20$.

Figure 26.– Concluded.
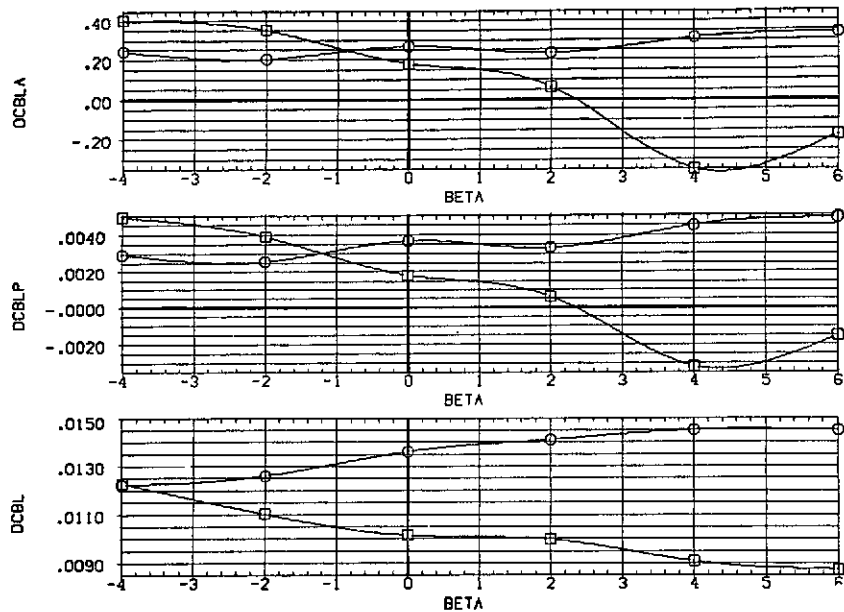
(a) Rolling—moment parameters.
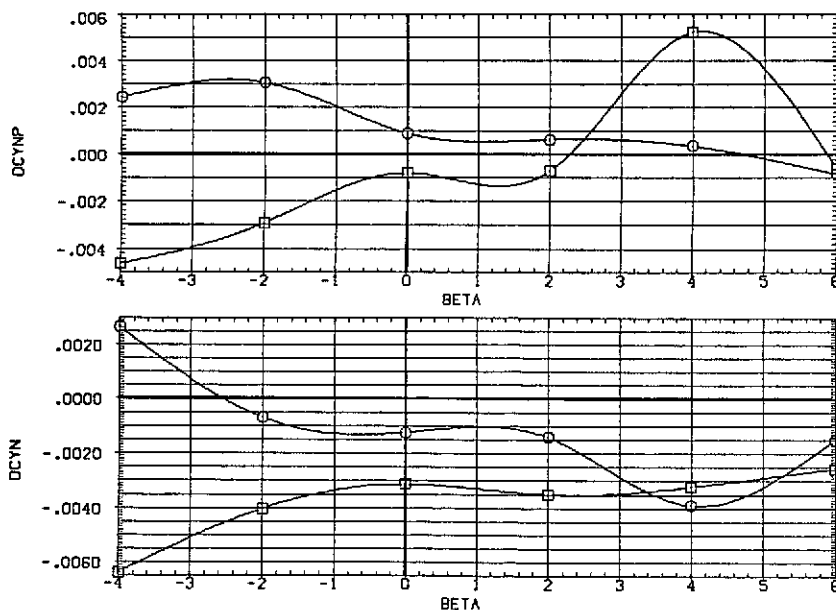
(b) Yawing—moment parameters.

Figure 27.— Effect of the orbiter and the solid rocket motor (SRM) plumes on the aileron effectiveness parameters at $\alpha = 0°$.